LEVEL

ANALYTICAL AND EXPERIMENTAL VALIDATION OF THE LIGHTNING TRANSIENT ANALYSIS TECHNIQUE

TECHNOLOGY INCORPORATED
INSTRUMENTS AND CONTROLS DIVISION
DAYTON, OHIO

MARCH 1978

TECHNICAL REPORT AFFDL-TR-78-47
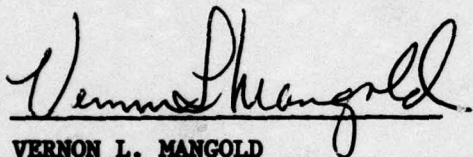Final Report for Period March 1977 — November 1977

AIR FORCE FLIGHT DYNAMICS LABORATORY
AIR FORCE WRIGHT AERONAUTICAL LABORATORIES
AIR FORCE SYSTEMS COMMAND
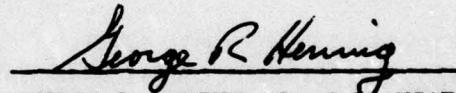WRIGHT-PATTERSON AIR FORCE BASE, OHIO 45433

79 01 22 096

NOTICE

When Government drawings, specifications, or other data are used
for any purpose other than in connection with a definitely related
Government procurement operation, the United States Government thereby
incurs no responsibility nor any obligation whatsoever; and the fact
that the Government may have formulated, furnished, or in any way
supplied the said drawings, specifications, or other data, is not to be
regarded by implication or otherwise as in any manner licensing the holder
or any other person or corporation, or conveying any rights or permission
to manufacture, use, or sell any patented invention that may in any
way be related thereto.

This report has been reviewed and is approved for publication.

VERNON L. MANGOLD
Project Physicist

GEORGE R. HENNIG, Lt Col, USAF
Chief, Survivability/Vulnerability Br.
Vehicle Equipment Division
AF Flight Dynamics Laboratory

FOR THE COMMANDER

AMBROSE B. NUTT
Director, Vehicle Equipment Division
AF Flight Dynamics Laboratory

Copies of this report should not be returned unless return is re-
quired by security considerations, contractual obligations, or notice
on a specific document.

AIR FORCE/56780/24 May 1978 — 250

REPORT DOCUMENTATION PAGE		READ INSTRUCTIONS BEFORE COMPLETING FORM
1. REPORT NUMBER AFFDL-TR-78-47	2. GOVT ACCESSION NO.	3. RECIPIENT'S CATALOG NUMBER
4. TITLE (and Subtitle) Analytical and Experimental Validation of the Lightning Transient Analysis Technique		5. TYPE OF REPORT & PERIOD COVERED Final Report, for Period March — November 1977
		6. PERFORMING ORG. REPORT NUMBER
7. AUTHOR(s) W. McCormick, Ph.D. K. J. Maxwell R. Finch, Ph.D.		8. CONTRACT OR GRANT NUMBER(s) F33615-75-D-0090 PWI-19
9. PERFORMING ORGANIZATION NAME AND ADDRESS Technology Incorporated Instruments and Controls Division Dayton, Ohio 45431		10. PROGRAM ELEMENT, PROJECT, TASK AREA & WORK UNIT NUMBERS 200 p.
11. CONTROLLING OFFICE NAME AND ADDRESS Air Force Flight Dynamics Laboratory Air Force Systems Command Wright-Patterson AFB, Ohio 45433		12. REPORT DATE March 1978
		13. NUMBER OF PAGES 167
14. MONITORING AGENCY NAME & ADDRESS(if different from Controlling Office)		15. SECURITY CLASS. (of this report) Unclassified
		15a. DECLASSIFICATION/DOWNGRADING SCHEDULE N/A

16. DISTRIBUTION STATEMENT (of this Report)

Approved for public release; distribution unlimited.

17. DISTRIBUTION STATEMENT (of the abstract entered in Block 20, if different from Report)

18. SUPPLEMENTARY NOTES

19. KEY WORDS (Continue on reverse side if necessary and identify by block number)

Lightning Transient Analysis	Linear System Model
Lightning Simulation Testing	Scaling
Lightning Susceptibility	Capacitive & Inductive Coupling
Linearity	Transfer Function

20. ABSTRACT (Continue on reverse side if necessary and identify by block number)

A research program was undertaken to analyze and experimentally validate the Lightning Transient Analysis (LTA) technique using Lightning Simulation Test (LST) data. Using linear systems theory, the LST has been shown to be a linear combination of three transfer functions. These transfer functions were derived and shown to be valid. Specifically, the linear transform of the output pulse $[S_{LST}(\omega)]$ was shown to be the product of linear transfer func-

$L_{sub\ LST}$ ω (omega)

407 742

tions of the LST configuration $[G_{LST}(\omega)]$, an aperture coupling term $[G_{ap}(\omega)]$ and the aircraft wiring/measurement equipment $[G_{a/c}(\omega)]$.

The LST configuration transfer function was derived using a shorted TEM analytical transmission line model which was validated experimentally using low-loss RG-58 cabling and verified by tests on an F-111 circuit. The aperture transfer function was defined by extending Van Bladel's small aperture expressions to the near field. Experiments were performed to measure E and H field coupling, and two-dimensional potential (e.g., resistance paper) methods were used to evaluate the electromagnetic fields in the vicinity of the aperture. A novel and simple experimental approach to simulate peripheral skin current density with a yoke coil was developed to analyze near- and far-field effects and shielding and was found to yield accurate results. Van Bladel's small aperture dipole expressions were adapted to enable prediction of the effective voltage impulse levels for both capacitive and inductive coupling. An estimate was made of the cable length that must be exposed to lightning excitation to yield measurable induced voltages. The estimate of five centimeters indicated that such lengths are typically present in aircraft circuits. The aircraft cabling transfer function was derived by analyzing the transient responses in the time and frequency domains using a transmission line model of an F-111 fuselage circuit. The results were compared to those obtained on the actual F-111 circuit. Additional investigations were performed to identify the scalable physical variables using the derived transfer functions. Because of the inherent homogeneity properties of a linear system, it was demonstrated that any physical variable (i.e., i, di/dt, v, dv/dt) is scalable provided the input waveform remains invariant. The proper technique for LTA amplitude scaling between ground based and airborne measurements was defined. A technique for decoupling LST configuration effects using the measured aircraft response and its impedance was developed. An LTA model was postulated that explains some commonly observed LTA signal phenomena. It was shown that the physical nature of the aperture coupling (i.e., capacitive vs inductive coupling) can be determined using the phase response of the voltage transfer function in the frequency domain.

It was concluded that the combination of frequency domain LTA technique and advanced LST processing equipment is a solid foundation for assessing aircraft vulnerability to the lightning hazard.

Recommendations are made to perform analytical and experimental studies to quantify configuration effects; small aperture spatial electromagnetic fields and shielding effects; the pulse response of a wide range of aircraft circuits; the complete nature of aperture coupling, including identification of the dominant and secondary apertures; the effects of possibly distributed versus local excitation points and methods of extending the technique to other aircraft cabling parameters (e.g., terminating impedances, non-linear devices and cable lengths) and to shielded cabling. The amplitude scaling technique should be incorporated into existing routines at the AFFDL Electromagnetic Hazards Group data acquisition and processing system. Experimental programs should be continued to define the required parameters from natural lightning to permit the use of realistic standardized waveforms for the most probable and severe threats so that LTA can be used to its full potential. In the interim, LST programs should not be limited to a single waveform since important LTA information may be lost. Finally, the requirements for LST and LTA should be standardized for all aspects of instrumentation, procedures, data processing and analysis so that specifications for equipment design and testing can be written and implemented.

FOREWORD

This report describes a research effort sponsored by the Electromagnetic Hazards Group (FES), Vehicle Equipment Division (FE), Air Force Flight Dynamics Laboratory (AFFDL), Ohio under Project 43630135, "Analytical and Experimental Validation of the Lightning Transient Analysis Technique".

The work reported herein was performed by Technology, Incorporated under Contract F33615-75-D-0030, Proceed Work Instruction (PWI) Number 19, during the period March 1977 to November 1977, under the direction of Mr. Vernon L. Mangold (AFFDL/FES), project engineer.

Dr. W. McCormick, principal investigator, was responsible for the development and publication of the technical work presented in this report and was assisted by Mr. K. Maxwell, senior engineer. Dr. R. Finch was program manager for Technology, Incorporated.

The authors wish to thank the Electromagnetic Hazards Group (AFFDL/FES) for the support provided, which included use of the Lightning Simulation Test (LST) facilities.

TABLE OF CONTENTS

TABLE OF CONTENTS (Concluded)

LIST OF ILLUSTRATIONS

LIST OF ILLUSTRATIONS (Continued)

LIST OF ILLUSTRATIONS (Continued)

LIST OF ILLUSTRATIONS (Continued)

LIST OF ILLUSTRATIONS (Continued)

LIST OF ILLUSTRATIONS (Continued)

LIST OF ILLUSTRATIONS (Concluded)

LIST OF TABLES

SUMMARY

1. Lightning Transient Analysis

Lightning Transient Analysis (LTA) is a technique that applies the results of Lightning Simulation Tests (LST) towards the prediction of the response of aircraft circuits to an actual lightning event. In this study the method that was investigated is currently being used by the EM Hazards Group of AFFDL. This particular method has been converted to a computer model which is in a constant state of validation/verification and refinement. Inputs for the model are derived from on-going LST programs. The purpose of LTA is to provide aircraft and aircraft system designers with data and/or design guidelines for protecting modern-day aircraft against the lightning hazard. For example, such guidelines would quantify the transient response expected on internal circuitry from lightning events, thus allowing the designers to take precautions in protecting avionics systems and selecting optimum cable routes throughout the vehicle.

a. Lightning and Laboratory Simulation

There can be no question that aircraft struck by lightning are subjected to severe mechanical stresses externally and to severe electrical stresses internally. These facts have been made abundantly clear by flight experience.[1] The external mechanical stresses are observed to occur in close physical proximity to the entry/exit points of the lightning current. The internal electrical stresses, on the other hand, are distributed throughout the aircraft interior. These effects occur because natural lightning generates electric and magnetic fields which penetrate into the interior of aircraft by various methods.

By convention aircraft lightning damage has been separated into two categories: "direct effects" and "indirect effects." Direct effects produce the mechanical changes to the aircraft and are a consequence of the intimate contact of lightning current with and conduction through the skin. Indirect effects result not from direct mechanical forces but from electromagnetic fields resulting from lightning events.

Lightning is characterized by an electric field strength prior to current flow. This field collapses as the return stroke phase is initiated. The neutralizing current flowing in a lightning channel (return stroke) rises to some peak magnitude, I_p, in a few microseconds as shown in Figure 1. During this risetime, T_f, the current is rapidly changing in magnitude. This rate of change of current is usually characterized by a single worst case value of di/dt, although the actual di/dt is not really constant over the time from zero current to peak current. After reaching its peak the
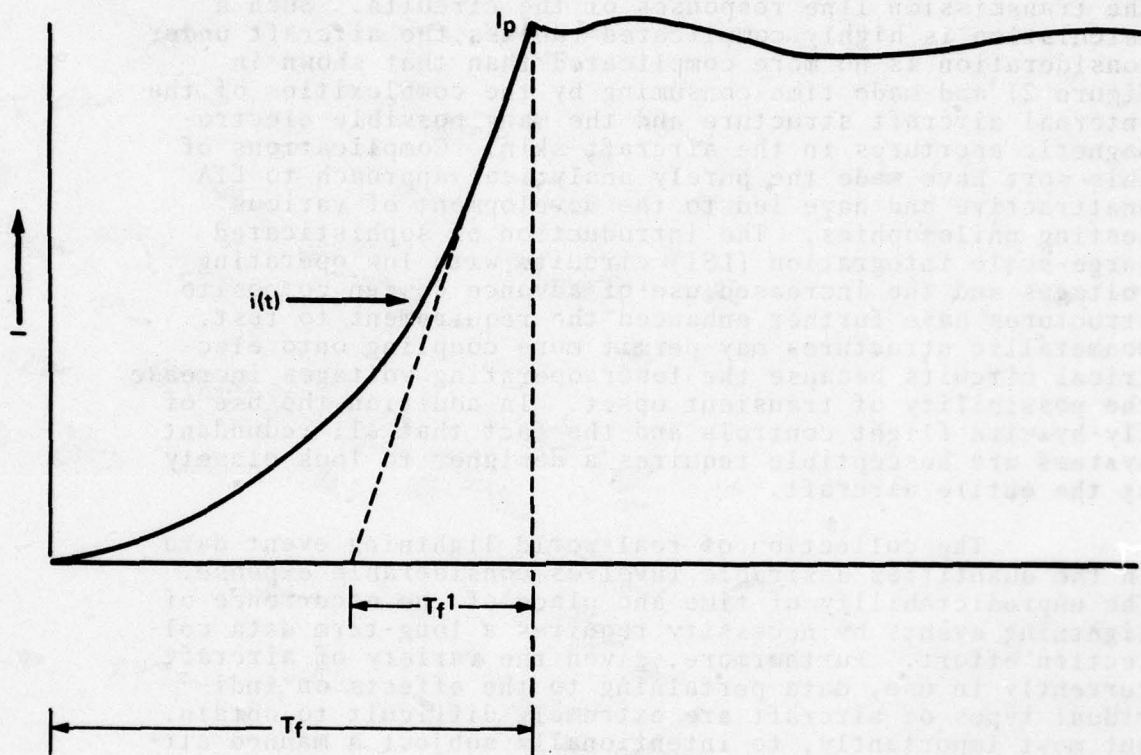
T_f = FRONT TIME AS MEASURED AT GROUND LEVEL

T_f¹ = POSSIBLE EFFECTIVE TIME AS MEASURED AT A FLIGHT VEHICLE

Figure 1.   Characteristic Current-Time History of Return Stroke

current falls in a few hundred microseconds to some intermediate or low value. These lower levels may last for durations of milliseconds to hundreds of milliseconds. From an effects point of view, only the electric field and the rapidly changing magnetic field (produced by the current I_p) cause significant transients in aircraft electrical circuits. Theoretically the induced transients on aircraft circuits can be calculated by estimating the internal electromagnetic field, predicting the coupling coefficients and calculating the transmission line responses of the circuits. Such a calculation is highly complicated (unless the aircraft under consideration is no more complicated than that shown in Figure 2) and made time-consuming by the complexities of the internal aircraft structure and the many possible electromagnetic apertures in the aircraft skin. Complications of this sort have made the purely analytical approach to LTA unattractive and have led to the development of various testing philosophies. The introduction of sophisticated large-scale integration (LSI) circuits with low operating voltages and the increased use of advance design composite structures have further enhanced the requirement to test. Nonmetallic structures may permit more coupling onto electrical circuits because the lower operating voltages increase the possibility of transient upset. In addition the use of fly-by-wire flight controls and the fact that all redundant systems are susceptible requires a designer to look closely at the entire aircraft.

The collection of real-world lightning event data in the quantities desirable involves considerable expense. The unpredictability of time and place of the occurrence of lightning events by necessity requires a long-term data collection effort. Furthermore, given the variety of aircraft currently in use, data pertaining to the effects on individual types of aircraft are extremely difficult to obtain. But most importantly, to intentionally subject a manned aircraft to a lightning environment is potentially hazardous. Because real event data is required for the ultimate validation/verification of LTA, the Electromagnetic (EM) Hazards Group of the Air Force Flight Dynamics Laboratory (AFFDL) at Wright-Patterson Air Force Base, Ohio, has initiated programs for collection of the much needed data.[2] In the meantime, laboratory simulations of lightning phenomena parameters of interest such as peak current, current rise times and decay times have been developed.[3] The laboratory simulations provide a controlled and repeatable environment that can be applied to an aircraft so that its response and that of its systems can be measured. Such simulations normally pertain to the high peak current phase, called the return stroke, of negative discharge lightning flashes. This type of simulation is usually the nature of LST.
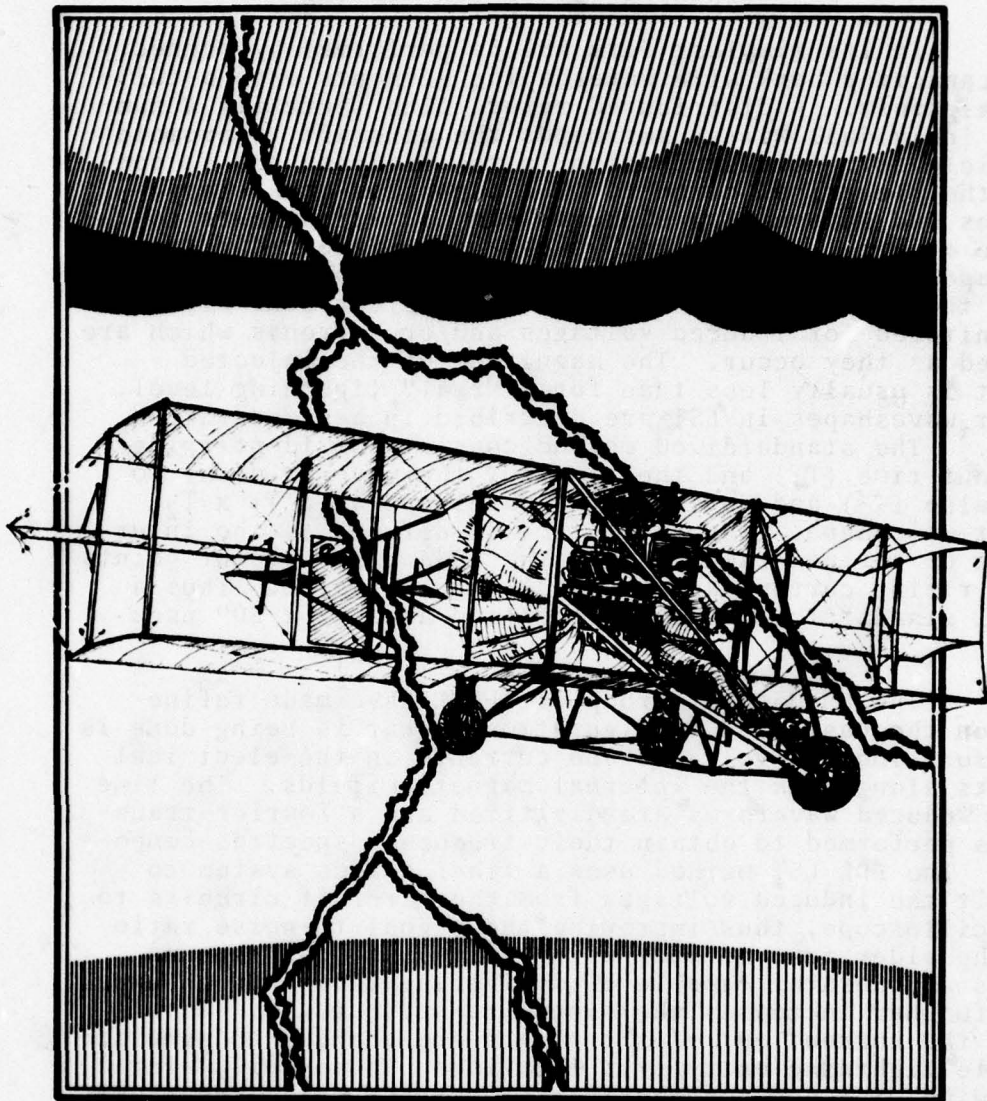
Figure 2. Aircraft with Limited Lightning Susceptibility

b. Lightning Simulation Testing

In its simplest form LST is performed by connecting a capacitor bank with waveshaping elements onto a full-scale aircraft. A distributed return line (actually a number of individual wires) surrounds the aircraft to promote free field current distribution in the airframe and to complete the electrical circuit. The capacitor bank charge voltages and waveshaping elements can be varied so as to produce a variety of current waveshapes. Selected current waveshapes and magnitudes are conducted through the aircraft. During the flow of current the internal electrical circuits are monitored for induced voltages and/or currents which are recorded as they occur. The magnitude of the injected current is usually less than for a "real" lightning level. Current waveshapes in LST are described in a standardized manner.[3] The standardized method consists of identifying the front time (T_1) and the time for the wave to decay to half value (T_2) and defining the waveshape as a T_1 x T_2 current waveshape. The front time is defined as the intersection of a line drawn through the 10 and 90 percent points of the rising current and the peak current value. Thus a typical standardized wave is specified as a "2 x 50" μsec wave.

The EM Hazards Group of AFFDL have made refinements on the basic LST configuration. What is being done is to measure induced voltages and currents in the electrical circuits along with the internal magnetic fields. The time domain induced waveforms are digitized and a Fourier transform is performed to obtain their frequency spectral components. The FDL LST method uses a fiber optics system to transmit the induced voltages from the aircraft circuits to the oscilloscope, thus improving the signal-to-noise ratio from the older test methods using twin-axial cables, and employs a generator capable of delivering thousands of amps which further increases the signal-to-noise ratio. In all tests, the current entry/exit points are changed to simulate possible lightning entry/exit locations. Nose-tail, wing-tail, wing-wing and nose-horizontal current paths are those most frequently selected. Tests on avionics systems can thus be performed *in situ*, powered up or powered down.

One assumption regarding the waveform applied from a laboratory generator is that the current pulse contains a frequency distribution and relative discrete frequency amplitude comparable to a natural lightning return stroke but at lower (scaled) levels. A 2 x 50 μsec waveshape is commonly used because it corresponds somewhat to the specified waveshape in MIL-B-5087B[4] and satisfies Aerospace Recommended Practice.[3] However, the selected 2 x 50 wave does not represent a small model of a real lightning pulse. Most tests performed by the EM Hazards Group supplement this standard waveshape with a variety of other waveshapes to

maximize the amount of information obtained. The objective of applying any waveform is to provide the internal cables with a spectrum of frequencies of "appropriate" relative proportions to which they can respond. From this frequency domain point of view it is apparent that the cables will respond only at discrete frequencies or over discrete bands. The application of multiple waveshapes permits facility effects to be eliminated using the LTA method to be discussed.

Another assumption upon which scaled LST methods depend is linearity. This assumption is that for a given input (drive) function, there is a response function whose magnitude will change in direct proportion to a change in the input function. The concept of linearity as it applies here is that the induced transients are related to the applied current and that the relationship can be approximated by the solution of a linear differential equation. Verification of linearity has been investigated in a number of ways by several methods.[5,6,7,8,9] Linearity appears to be a valid assumption as has been shown by Lloyd and Walko[5] and for low frequency scaling by Burrows.[6]

Among the objectives of this program were the definition of the proper way to perform lightning simulation tests and the analysis of the measured data. Specifically, objectives were to determine whether or not lightning simulation testing is linear, what the nature of coupling to internal circuits is, and what the appropriate method of scaling laboratory test data to the natural environment is.

2. Analytical Validation of the LTA Technique

In a general sense, the LTA approach can be considered as an identification problem involving a hybrid lumped-distributed parameter system. During the past 10 years, considerable time and effort have been expended on this highly challenging identification problem. Impressive contributions from electromagnetics, plasma physics, etc. have been made in the LTA area, yet major questions concerning interpretation and methodology still remain. In contrast to the previous work, the present investigation has approached the problem in a significantly different way. Rather than emphasize the detailed physics of the problem, the present study concentrated instead on the detailed modeling of the system as a general linear, time-invariant system. Using the linear system framework, the powerful techniques of convolution and transfer function theory were applied in an attempt to understand both the physics and the dynamics of the complete system.

Independent of the physical details and peculiarities of the LST system, the fundamental linearity of the overall LST system is assured as a direct result of the basic linearity of Maxwell's field equations. Linearity, in the pre-

sent context, is equivalent to the property of superposition
which simply states that the response to the sum of two in-
puts is the sum of the responses to the individual inputs.
The superposition property along with the property of time-
invariance holds for any static system described by Maxwell's
equations and permits, as a consequence, the use of the fre-
quency domain or transfer function approach which is particu-
larly well suited to the analysis of the cascade configura-
tion found in the LTA problem.

Referring to Figure 3, the LTA model, in time sequence,
consists of the LST configuration-dependent skin current
which electromagnetically couples through the "small aper-
ture" to the aircraft cable. A small aperture is defined as
one with aperture dimensions much smaller than a wavelength.
From left to right, the LST configuration transfer function,
$G_{LST}(\omega)$, relates the pulse assembly parameters to the air-
craft distributed parameters in a way that defines the Fourier
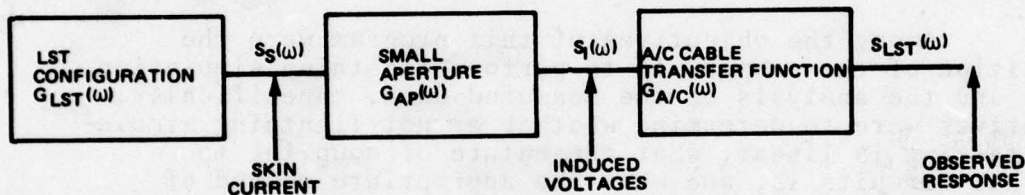
Figure 3. LTA Cascade Configuration in LTA Problem

transform of the aircraft skin current, $S_S(\omega)$, (see Paragraph
2.a.). Assuming that the dominant flux coupling is "small
aperture," the second transfer function, $G_{AP}(\omega)$, expresses
capacitive and inductive coupling in terms of induced aper-
ture voltage, $v_I(t)$, as a linear derivative operation on the
aircraft skin current, $i_S(t)$, given as:

$$v_I(t) = K \frac{di_S(t)}{dt} + a \frac{d^2 i_S(t)}{dt^2} \tag{1}$$

where K and a are constants

with the equivalent transfer function:

$$G_{AP}(\omega) = K [j \omega - a \omega^2] = \frac{S_I(\omega)}{S_S(\omega)} \tag{2}$$

The final aircraft cable transfer function, $G_{A/C}(\omega)$, relates the induced aperture voltage, $v_I(t)$, at its point of application to the output voltage, $S_{LST}(t)$, measured at any point within the aircraft cabling. From basic linear system theory it now becomes possible to multiply the transfer functions and, provided each transfer function is isolated from the preceding transfer function, express the transform of the output pulse, $S_{LST}(\omega)$, as:

$$S_{LST}(\omega) = G_{LST}(\omega)\ G_{AP}(\omega)\ G_{A/C}(\omega) \tag{3}$$

Fortunately, this isolation exists in the LST configuration since neither the "small aperture" itself nor the aircraft cabling will significantly load the aircraft skin current. With the available Fast Fourier Transform (FFT) algorithms and with the observed input current and output voltage waveforms, a simple, direct system identification can be made as described in the following sections.

To summarize, the following assumptions were made in the present investigation:

a. Dominant coupling due to the relationship between wavelength and aircraft dimensions is small aperture coupling (no diffusion or resistance components were observed during pulse tests).

b. There is only one dominant aperture.

c. The small aperture(s) and aircraft cabling do not significantly load the aircraft skin current, $i_S(t)$.

d. As various tests have confirmed, the system is linear and time-invariant.

Some of the data reported here has been reported previously in Reference 10. This particular data was collected as part of a normal LTA program and was not originally collected specifically for use in this study (See Appendix). However, the data was used in this study to prove the LST linearity assumption and to provide insight into the coupling mode (electric or magnetic field) for certain electrical circuits. Many electrical circuits were studied in the original F-111 LTA work but the present work concentrates on

the results obtained for the yaw computer to yaw damper servo circuit. The circuit consists of a 17.2 meter run of cable from the yaw computer in the forward fuselage area to the yaw servo damper assembly in the top of the aircraft as illustrated in Figure 4 and presented in more detail in Figures 5 and 6. A schematic representation of this circuit is presented in Figure 7. The only apertures which are located near the circuit cable run are the speed brake just forward of the main gear and the opening in the wing pivot area.

a. Scope and Results of Investigation

The results of the investigations performed during this program are presented in Sections 2 through 5 and summarized below in the four specific categories. These categories arise naturally from the LTA problem and correspond to the transfer function blocks of the linear system representation of Figure 3.

(1) LST Configuration Effects

(a) The LST configuration effects were completely analyzed using a transverse electromagnetic (TEM) shorted-end transmission line representation. The TEM representation was completely verified by actual F-111 skin current measurements and also through a detailed laboratory simulation using RG-58 cabling.

(b) With the LST TEM representation, equivalent linear system representations were defined in both the time domain (impulse response) and frequency domain (transfer function). The derived $G_{LST}(\omega)$ was shown to be:

$$G_{LST}(\omega) = \frac{v_c \, C_s}{1 - \omega \, C_s \, Z_0 \, \tan\left(\frac{\omega \ell_{A/C}}{c}\right) + j \, \omega \, R_s \, C_s} \tag{4}$$

where v_c = capacitor charge voltage, volts

C_s = capacitance of the pulse capacitor

R_s = value of damping resistor, ohms

Z_0 = characteristic impedance of LTA configuration

$\ell_{A/C}$ = length of aircraft, meters

c = speed of light ($c \approx 3 \times 10^8 \text{m/s}$)
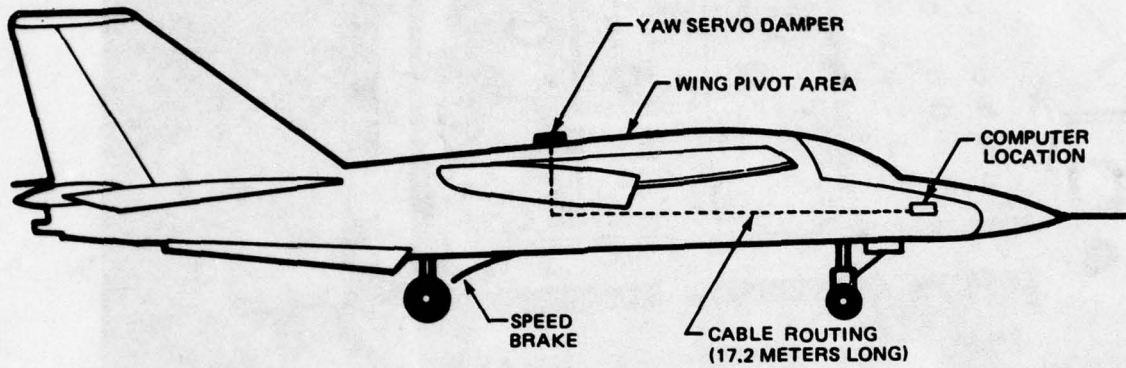
Figure 4. Location of Yaw Computer, Yaw Servo Damper, and
Interconnect Cable Routing for F-111 S/N 67-116A
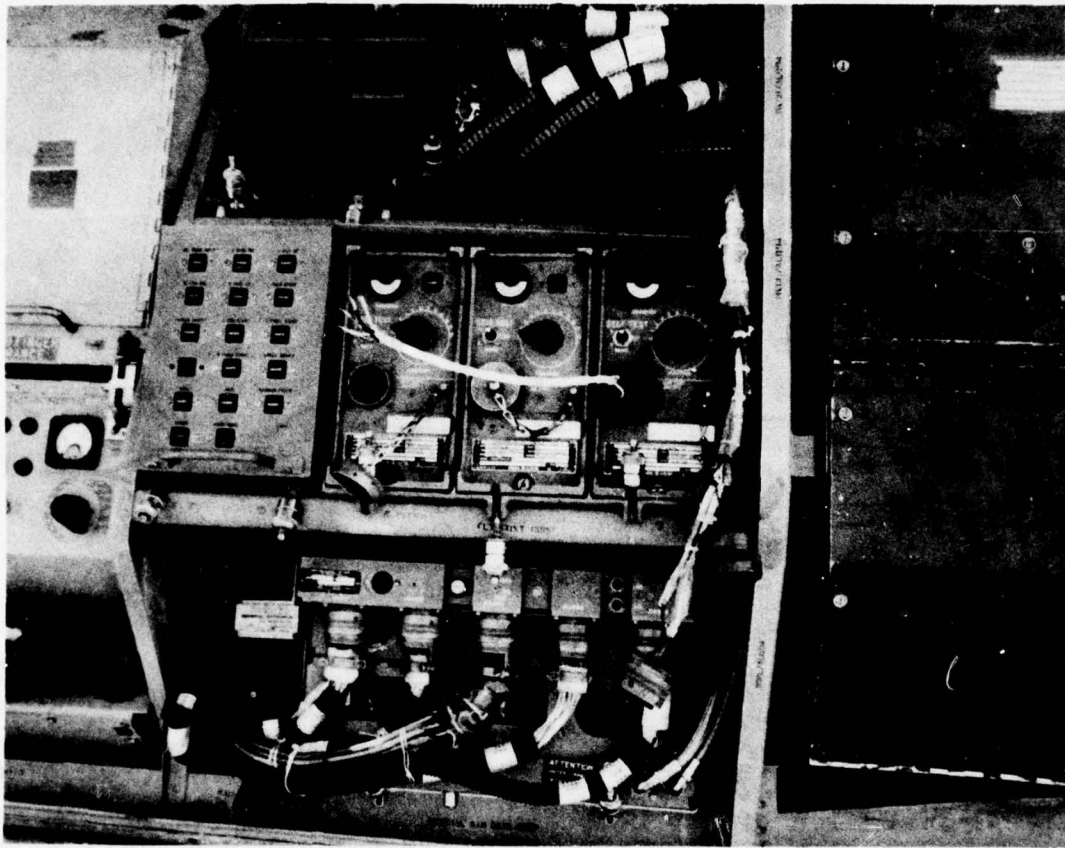
Figure 5. Access Door 1101 to Equipment Bay on F-111E
Showing Pitch, Roll and Yaw Computers
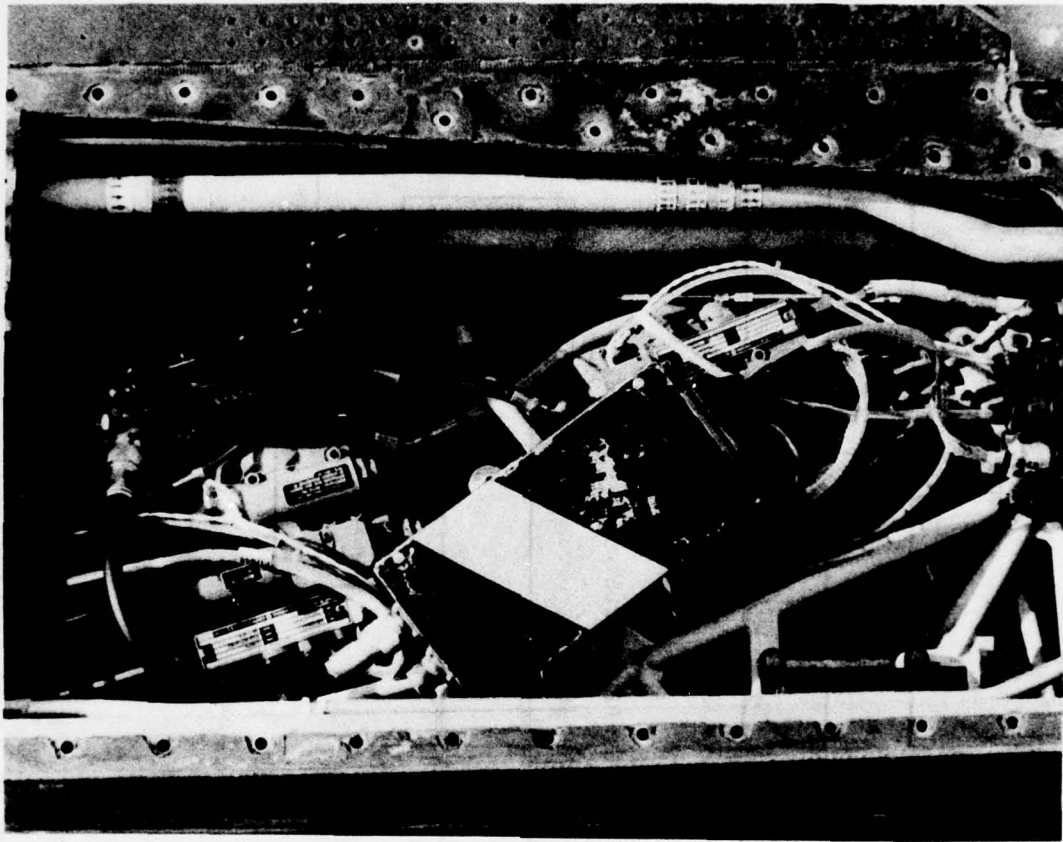
Figure 6. Test Connection for Yaw Damper Servo
Transient Measurement
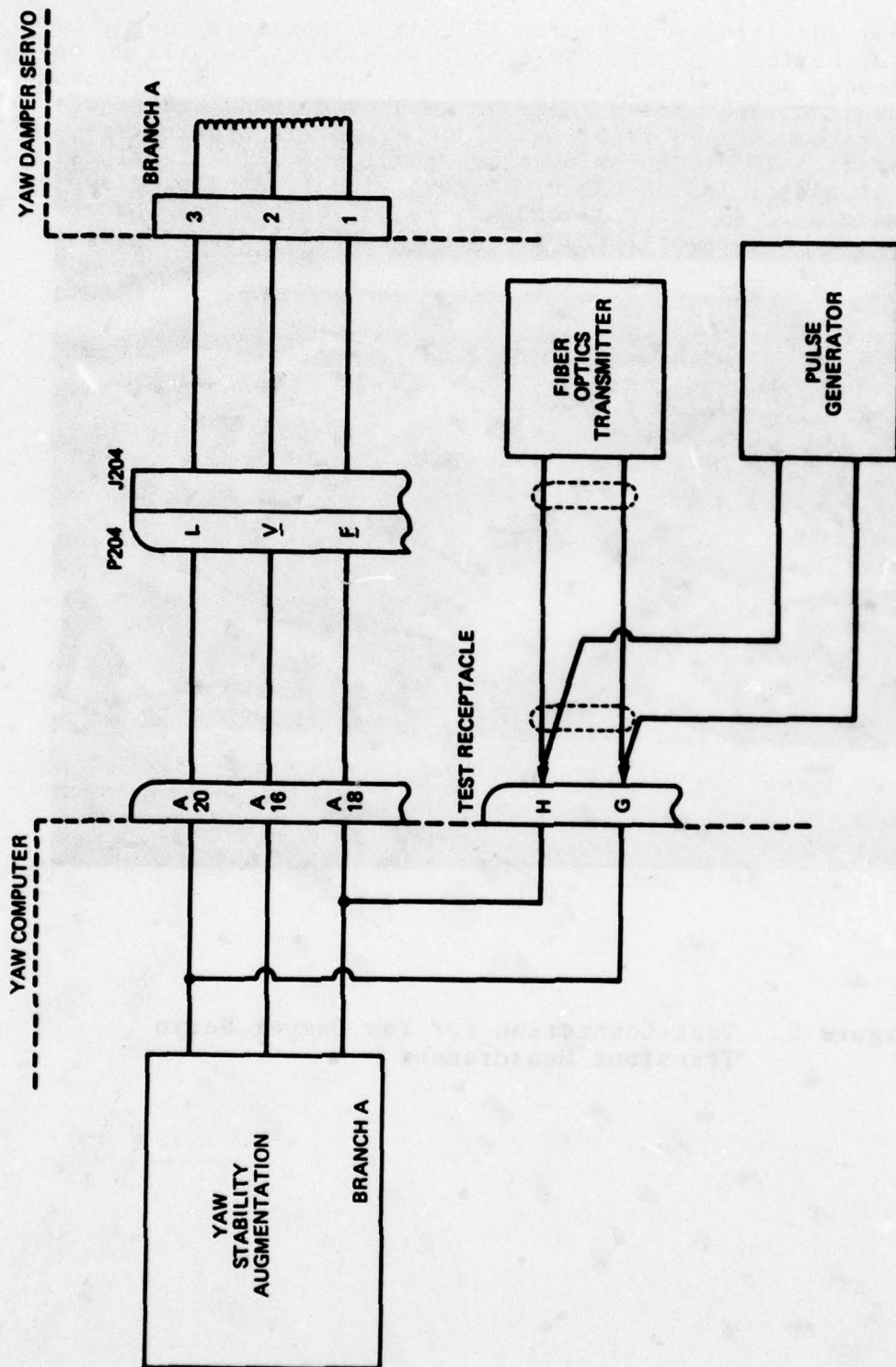
Figure 7. Schematic of LST Circuit for Lightning Transient Research on an F-111 Aircraft

The above system description allows a straight-forward compensation for the LST configuration effects using standard linear system techniques.

(c)   The TEM model determined the relationship between the LST current pulse, $i_s(x,t)$, and voltage pulse, $v_s(x,t)$, waveforms along the aircraft axis. Such a determination yields an estimate of the relative effects of capacitive and inductive coupling.

(d)   The TEM assumption was used along with scaled models and two-dimensional potential techniques to investigate the dependence of skin current density distributions on LST geometry. The effect of varying entrance-exit points on the skin current density was also studied for both the LST and airborne situation.

(2)   Small Aperture Studies

(a)   A determination was made of small aperture near-field behavior, both from experimental (yoke coil) measurements and also from resistance paper potential solutions. Van Bladel's (Ref. 11) results were extended to numerically determine the electric and magnetic scalar field potentials of a circular aperture in the near and far field.

(b)   A continuous wave, CW, technique using yoke coils was defined to measure $\vec{E}$ and $\vec{H}$ coupling in an accurate, carefully controlled manner. In conjunction with the potential theory approach, these tests will provide a method for predicting induced excitation voltage levels for any arbitrary aperture, cavity, and cable routing strategy.

(c)   The effect of shielding was investigated by the resistance paper method, the conjugate harmonic method, and the graphical curvilinear square method as were motivated by the TEM assumption.

(d)   Significant analytical progress was made in adapting Van Bladel's dipole expressions to the prediction of effective voltage impulse levels for both capacitive and inductive coupling. This work led to the transfer function, $G_{AP}(\omega)$, presented in Figure 3.

(3) <u>Pulse Response of Aircraft Cabling</u>

    (a) The pulse response of aircraft cabling was successfully modeled as a low-loss transmission line terminated at both ends and excited by an induced waveform at some point through an infinite impedance. A new time-domain technique was developed for analyzing the pulse response of low-loss cabling when excited from a high impedance source. The model was defined for any arbitrary excitation point or waveform and can be used with any terminating impedance values. The new technique permits a direct prediction of the excitation waveform from the observed output waveform or, conversely, the prediction of the aircraft cable transient response to any arbitrary excitation pulse. The new approach is a characterization of the linear system by means of its impulse response and is extremely well suited to experimental investigation. With this method, actual pulse tests were performed on the yaw damper circuit of the F-111 and yielded results consistent with the LST experiments. Using this technique, it is now possible to predict the effect of a postulated excitation pulse on any given section of aircraft cabling. With further refinement, this technique will provide essential information as to the nature of the LST coupling phenomena and should eventually lead to a procedure for predicting (spec-ing) the effects of lightning on any given aircraft circuit.

    (b) Using the same high source impedance model of (2.a.(1)), the complete voltage transfer function of the aircraft cable system was derived, including the effects of loss. The transfer function, $G_{A/C}(\omega)$, forms the third block in the cascade configuration of Figure 3. The derived $G_{A/C}(\omega)$ equals (Ref. 12)

$$G_{A/C}(\omega) = K \frac{Z_1 Z_2}{Z_1 + Z_2} \qquad (5)$$

where: $Z_1 = Z_0 \tanh (\gamma \ell_1)$

                $Z_2 = Z_0 \coth (\gamma \ell_2)$ (Yaw Damper Circuit)

                Z_0 = characteristic impedance of cable

$$tanh(\ ) = \text{hyperbolic tangent function}$$

$$cotanh(\ ) = \text{hyperbolic cotangent function}$$

$$\gamma = \text{complex propagation constant including loss term}$$

$$\ell_1 = \text{distance from excitation point to shorted end}$$

$$\ell_2 = \text{distance from excitation point to open end}$$

$G_{A/C}(\omega)$ was programmed on a digital computer and was found to be consistent with actual CW (sine wave) tests on the F-111 and also with a detailed series of tests using RG-58 cabling. Using the transfer function phase response, a new technique was developed to determine the relative magnitudes of capacitive versus inductive coupling independent of where the excitation itself is physically applied. The resolution of the inductive versus capacitive coupling question is one of the major outstanding questions in LTA.

(c) A detailed series of experimental tests were performed to determine the effects of typical circuit nonlinearities (e.g., p-n junction) on the overall linearity of the system. From actual F-111 and RG-58 tests on a variety of devices (e.g. amplifiers, diodes, etc.), it was observed that linearity, in the sense of input/output superposition, is rarely affected by the usual zero-memory nonlinearity found in most aircraft circuitry. This fortunate fact is the direct result of the capacitive shunt to ground configuration commonly observed in most aircraft cable terminations.

(4) <u>System Considerations</u>

(a) The question of which physical variable to scale on (i, $\frac{di}{dt}$, v, $\frac{dv}{dt}$) was completely resolved. It was demonstrated by analysis that extrapolation (scaling) can be legitimately made on current magnitude (for a given waveshape) regardless of the nature of the coupling mechanism. Furthermore, the overall LST system impulse response was derived from the inverse transform of the ratio of the Fourier

transforms of the recorded input and output waveforms. Actual determination of the overall LST impulse response was accomplished using this procedure and represents a significant advance in the LTA program. With the LST h(t) defined, the output to any arbitrary input can be predicted from the convolution integral. The use of the convolution or superposition integral also provides a powerful confirmation of system linearity.

(b)   From linear system theory, a procedure was suggested that defines the aperture transfer function given the known aperture excitation point and, conversely, defines the cable transfer function given a dominant aperture location. An even more powerful technique using the phase response and the resonant nature of the cable transfer function was also developed to estimate the relative magnitudes of capacitive and inductive excitation.

(c)   A definitive resolution of the amplitude scaling problem was accomplished. From linear system theory, it was demonstrated that pure amplitude scaling can be performed only when the input waveform remains invariant. For the usual case where the LST waveform differs from the airborne lightning current waveform, a detailed procedure for proper scaling was defined using the convolution integral as an intermediate step.

b.   Important LTA Questions Resolved by the Investigation

To summarize and to also focus on the significance of the reported work, listed below are those LTA problems addressed and resolved in this study. It is evident that some of the items concern LTA questions that have excited discussion and controversy over the years.

(1)   A definitive answer to the amplitude scaling question was achieved. Specifically, the question of which physical variable may be amplitude scaled was resolved and also a detailed experimental procedure was advanced to test a given circuit for linearity. Furthermore, for the first time, the full implications of linearity were used in the quantitative analysis of the overall system.

(2) Important progress was made in the analysis and
     testing of the small aperture effect, particularly
     with regard to the previously unaddressed shield-
     ing and near-field effects. A convenient method
     using two-dimensional resistance paper was devel-
     oped that could lead to an optimum cable routing
     strategy.

(3) The LST configuration effects were successfully
     modeled. With this accurate representation it is
     now possible to compensate for configuration
     effects and to realistically extrapolate to ex-
     pected airborne signal levels.

(4) A complete linear system representation of the
     pulse response of aircraft cabling was developed
     in both the time and frequency domains. The new
     methods resolve the question of capacitive versus
     inductive coupling and should also lead to a
     complete system optimization with regard to the
     lightning threat.

3. Report Contents

The technical substantiation of subjects summarized in
this section is contained in Sections 2 through 5. These
sections are each an integrated compilation based on ten
technical memoranda prepared by Dr. W. S. McCormick of Tech-
nology Incorporated, Dayton, Ohio during the program as
performance progress reports. Rather than presenting the
memoranda in their original chronological sequence, the
reports have been integrated and compiled into the four
topical categories discussed in Paragraph 2, each presented
as a separate section of this report. All the relevant
technical content has been included in this report and ac-
tual reference to the progress reports for technical infor-
mation is unnecessary.

1. INTRODUCTION

Aircraft struck by lightning are subjected to severe mechanical (externally) and electrical (internally) stresses as evidenced by flight experience. To investigate this phenomenon and deal with the lightning hazard, analytical and test methods have been developed and are currently in use. Some of the methods, while widely used and documented, are the subject of a continuing controversy in terms of validity and realism. Because of the nature of the hazard it is essential that the methods used to define the magnitude of the hazard, the manner in which aerospace vehicle/system performance is affected, and the criteria being used in the development of new aerospace vehicle/system design be validated in a definitive way. To this end the program reported herein was undertaken to review existing Electromagnetic Pulse (EMP), and lightning technology and related analytical/experimental methods used to determine aircraft susceptibility to transient electromagnetic fields, determine which method (if any) is suitable to quantify the aircraft's response to the lightning hazard, and to validate the selected method.

The review of existing methods revealed a number of significant development programs, either completed or ongoing, by General Electric, McDonnell Douglas, Boeing and others. Some of the methods investigated were in various stages of expansion, development and/or verification. In common to all the methods found were the requirements for large computer facilities, large amounts of computation time and substantial programming support. These requirements result from the amount of structural and electrical details of the aircraft and its systems needed for valid lightning hazard analysis.

The determination of which existing method, or model, was best suited to confidently predict the response of an aircraft/system to lightning hazards entailed several considerations. Among these were theoretical basis, validity of assumptions, and agreement with available "real world" and other test data. A significant finding of this study was the realization that the Lightning Transient Analysis (LTA) method, developed by L. C. Walko (References 5 and 13) and refined by the Air Force during Lightning Simulation Tests (LST), is highly adaptable to Fourier analysis methods for the development of system and subsystem or component transfer functions which enable definition of their susceptibility, individually or collectively, to the lightning threat.

1

The selection of the LTA method to predict the response
of an aircraft/system to lightning hazards required that its
credibility be established by dealing with those aspects of
the method which have been the subject of some controversy.
Questions had arisen as to the validity of the use of LST
results in LTA, the linear extrapolation of LST current
levels to those levels present in the actual lightning
hazard, and the nature of the coupling of the lightning
energy to the internal cables of the aircraft.

2. LST CONFIGURATION EFFECTS

In general, the LST configuration includes the lumped elements of the pulsing assembly as well as the distributed parameters of the aircraft (A/C) and ground return paths. The initial objective of the investigation was to develop a linear system representation of the configuration in order to compensate for configuration effects. The results in this section provide a complete linear system based on the TEM mode assumption. As will be demonstrated, the TEM model has completely quantified the configuration effects and has supplied the system transfer function, $G_{LST}(\omega)$, for the overall system.

2.1 Frequency Domain Approach

2.1.1 General Discussion

The initial representation of the LST configuration was in the frequency domain. Using the shorted TEM frequency transmission line model, the complete representation of the LST configuration was identified as well as the bulk inductance of the LST configuration. As a final result, the configuration transfer function, $G_{LST}(\omega)$, was identified.

2.1.2 Detailed Discussion

The present approach is to consider the LST configuration effects and the internal aircraft cable responses as essentially isolated in an electromagnetic sense. This key assumption allows the multiplication of transfer functions and suggests a systematic procedure to decouple the LST configuration effects. As a first (analytical) step in this approach, the LST configuration is modeled as a shorted, low-loss transmission line operating physically in the fundamental TEM mode. In this model, the aircraft skin and return lines form the two conductor "planes" with the $\vec{E}$ and $\vec{H}$ fields contained in the space between conductors. For the AFFDL F-111, oscillatory input measurements suggest a bulk inductance, $\bar{L}$, of 17 μh for the entire LST configuration (including wiring, etc.) giving an inductance per meter, L, of 0.77 μh/m for a 22 m aircraft. The capacitance per meter, C, can now be calculated from the IMPORTANT reciprocity relation between L and C for the TEM mode given as:

$$C = \frac{\mu_0 \, \varepsilon_0}{L} \tag{6}$$

or, in our case where $\mu_0 = 4\pi \times 10^{-7}$ H/m and $\varepsilon_0 = 8.85 \times 10^{-12}$ F/m:

$C = 14.4$ pf/m or $\bar{C} = C\ell_{A/C} \approx 317$.

The LTA configuration is then given by:

3

$$Z_0 = \sqrt{\frac{L}{C}} \approx \sqrt{\frac{0.77 \times 10^{-6}}{14.4 \times 10^{-12}}} \approx 231\Omega$$

Continuing with the analysis, the input admittance of the shorted transmission line can be expressed as:

$$Y = -j\, Y_0 \cot \frac{\omega\, \ell_{A/C}}{c} \tag{7}$$

where Y_0 is the reciprocal of the characteristic impedance. The admittance of (Eq. 7) has singularities at $\omega = n\left(\frac{\pi C}{\ell_{A/C}}\right) = n\omega_1$, where $n = 0,1,2,\ldots$, and can be expressed in the following alternate form:

$$\frac{Y}{Y_0} = -j\, \frac{1}{\pi} \frac{1}{\frac{\omega}{\omega_1}} + j\, \frac{2}{\pi} \sum_{n=1}^{\infty} \frac{\omega/\omega_1}{n^2 - \left(\frac{\omega}{\omega_1}\right)^2} \tag{8}$$

where $\omega_1 = \pi c/\ell_{A/C} = 2\pi f_1$. That is $f_1 = c/2\ell_{A/C} \approx 6.8$ MHz fundamental.

The expression of (Eq. 8) immediately suggests the following equivalent circuit for the assembly at the front of the aircraft:
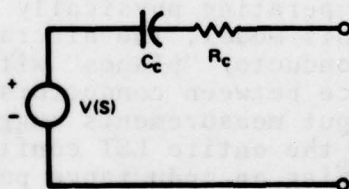
Figure 8. Thevenin Equivalent Circuit of Pulse Assembly

Since it is more convenient to drive an admittance model with a current drive, the above Thevenin circuit can be reduced to its Norton equivalent given as:
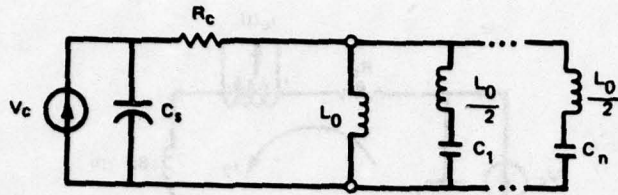
where $L_0 = \mathcal{L} = 17 \ \mu h$

$$C_n = \frac{2\ell_{A/C}}{Z_0 n^2 \pi^2 C} = \frac{2}{n^2 \pi^2} \cdot \frac{1}{C}$$

Figure 9. Norton Equivalent Circuit
of Pulse Assembly

where the current generator is now an impulse of strength V_c.

Combining the source with LST equivalent circuit, we arrive at
the complete equivalent circuit shown below:

OVERALL LTA CONFIGURATION
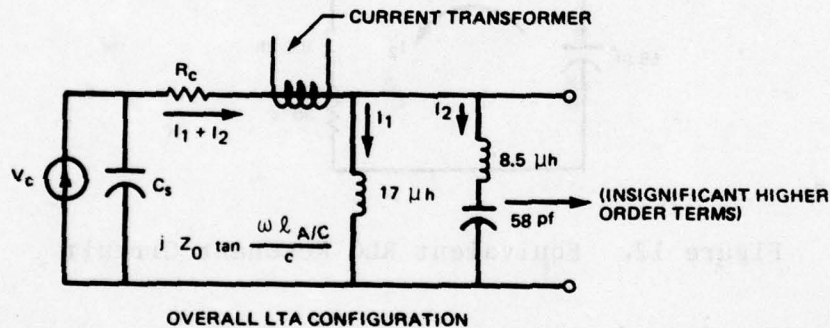
where $C_1 = \dfrac{2\ell_{A/C}}{Z_0 \pi^2 C}$

Figure 10. Equivalent Circuit of Overall
LTA Configuration

In the overall equivalent circuit, the current I_1 represents
the usual unipolar over-damped waveform while I_2 represents
an LST oscillatory waveform. Using the property of super-
position, we can look at the I_2 as generated by the follow-
ing component equivalent circuit.

5
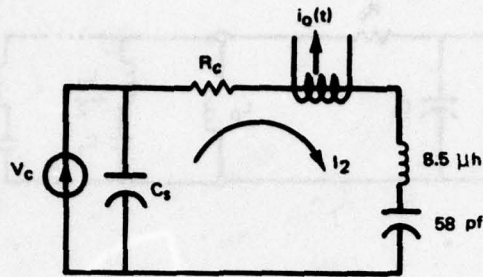
Figure 11. Component Equivalent
Circuit for I_2

Taking Figure 11 as a representative LST circuit, the C_s
can be set at 2.4 µf and R_c at 30 Ω. Since $C_s >> 58$ pf,
the series combination of C_s and the 58 pf is approximately
58 pf, reducing the circuit to the following simple series
R-L-C resonant circuit:
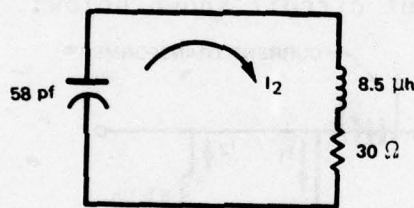
Figure 12. Equivalent RLC Resonant Circuit

with an under-damped resonant response of:

$$f_R \approx \frac{1.4}{2\pi\sqrt{L\,C}} \approx \frac{1.4}{\sqrt{17 \times 10^{-6} \times 58 \times 10^{-12}}} \approx 7.1 \text{ MHz} \qquad (9)$$

which agrees with the fundamental period of $c/2\ell_{A/C}$;
the damped time constant (e^{-1}) of:

$$\text{T.C.} \approx \frac{1}{\alpha} \qquad (10)$$

6

where $\alpha = \delta \omega_R = \dfrac{R}{2L_1} = \dfrac{R}{L_0} \approx 1.76 \times 10^6$ nepers $\approx 2 \times 10^6$ nepers

to give a 37% time constant of:

$$\text{T.C.} \approx 0.50 \ \mu\text{sec.} \tag{11}$$

Both the 6.8 MHz frequency and the 0.50 μsec T.C. are clearly indicated in Figure 13 where the I_1 and I_2 components are quite apparent. Since Figure 13 is only a typical observed waveform, the confirmation gives a validation to the model.

Consistent with Figure 10 and equation (7), the Fourier transform of the entire LST current can now be written from the series impedance configuration as

$$I_{LST}(\omega) = \frac{v_c}{Z_1 + Z_2} = \frac{v_c/j\omega}{\left(R_c + \dfrac{1}{j \omega C_s}\right) + j \ Z_0 \ \tan \omega \ \ell_{A/C}}$$

$$= \frac{v_c \ C_s}{1 - \omega \ Z_0 \ C_s \ \tan \left(\dfrac{\omega \ \ell_{A/C}}{c}\right) + j \ \omega \ R_c C_s} \tag{12}$$

where Z_0 equals 231Ω.

2.2 Time Domain Approach

2.2.1 General Discussion

It is instructive to analyze the LST configuration in the time domain. A time domain approach (Ref. 14) clearly illustrates the reflection properties of the system and also clearly defines the interrelationship between the voltage traveling wave, $v(x,t)$, and the current traveling wave, $i(x,t)$. The important conclusion of this section is that the $v(x,t)$ waveshape is proportional to the time derivative of $i(x,t)$; this result is of great significance in investigating the relative importance of capacitive versus inductive coupling.

7
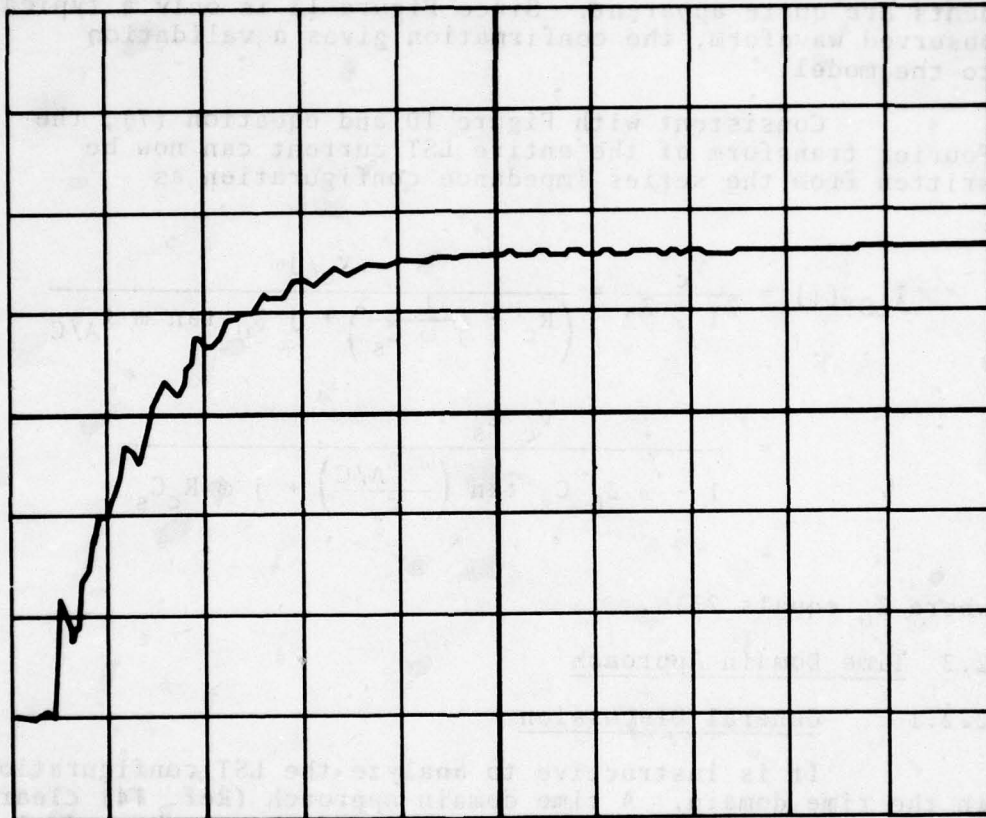
Figure 13. Typical Observed Waveform of LST Current

2.2.2 Detailed Discussion

The input impedance for the shorted transmission line is given by:

$$Z_{in} = j \, Z_0 \, \tan\left(\frac{2\pi \, \ell_{A/C}}{\lambda}\right) \quad (13)$$

where Z_0 is the characteristic impedance of the LTA configuration equal to 231Ω. For all significant frequencies of the unipolar pulse ($f < 1$ MHz), λ is $>>$ than the aircraft length and Z_{in} can be written, using the small angle approximation for the term tan ( ), as:

$$Z_{in} \approx j \, 231 \left(\frac{2\pi \, \ell_{A/C}}{\lambda}\right) = j \, 231 \left(\frac{2\pi f \ell_{A/C}}{c}\right) \quad (14)$$

which implies an inductance equal to

$$\overline{L} = \left(\frac{231}{c}\right) \ell_{A/C} = 0.77 \, \ell_{A/C} \, \mu h \quad (15)$$

$$\left[\begin{array}{l}\text{Note that at the attachment point } \ell_{A/C} = 22m, \\ \text{and } \overline{L} \text{ equals } \underline{17 \, \mu h} \text{ which checks with the ob-} \\ \text{served value.}\end{array}\right]$$

In order to better appreciate the TEM mode (Ref. 15), it is instructive to consider the unipolar transient response in the time domain. For the time interval, $0 < t < 2\ell_{A/C}/c$, before the first reflection, the discharge circuit is actually looking into what appears to be an infinite transmission line as shown below:
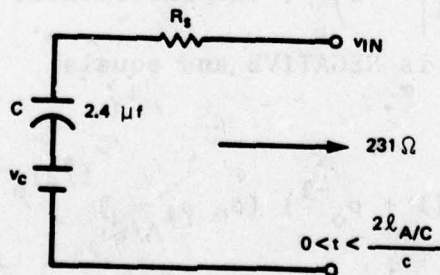
Figure 14. Equivalent Discharge Circuit

For every significant ω, $\frac{1}{\omega C} \ll (R_s + 231)$, so that the full v_c appears across the transmission line input at $t = 0^+$.

After $t > 2\ell_{A/C}/c$, v_{in} will be affected by reflections at the "shorted-end" with a reflection coefficient of $|\rho_{\ell_{A/C}}| = 1$ and at the "sending-end" with a

$$\rho_o = \frac{R_s - \frac{j}{\omega C} - 231}{R_s + \frac{j}{\omega C} + 231} \approx \frac{R_s - 231}{R_s + 231} \approx -1 \qquad (16)$$

A general analysis involving the two reflection points yields, after $m = t / \dfrac{2\ell_{A/C}}{c}$ round-trip intervals:

$$\frac{v_{in}}{v_c} = 1 + \sum_{n=1}^{m} \left(\rho_{\ell_{A/C}}^{\ n} \rho^{n-1} + \rho_{\ell_{A/C}}^{\ n} \rho_o^{\ n} \right) \qquad (17)$$
$$\underset{\text{(sending-}\atop\text{end)}}{} \qquad \underset{\text{(loaded-}\atop\text{point)}}{}$$

or

$$\frac{v_{in}}{v_c} = 1 + \left(1 + \frac{1}{\rho_o} \right) \sum_{n=1}^{m} \left(\rho_o \, \rho_{\ell_{A/C}} \right)^n \qquad (18)$$

Because the reflection at the "shorted-end" is 100% ($|\rho_{\ell_{A/C}}| = 1$) while the reflection at the "sending-end" is less than 100% $\left(|\rho_o| = \left| \dfrac{R_s - 231}{R_s + 231} \right| < 1 \right)$, the incremental change in v_{in} after a $2\ell_{A/C}/c$ interval is NEGATIVE and equals:

·

$$\frac{\Delta v_{in}}{v_c} = (1 + \rho_o^{-1}) \left(\rho_o \, \rho_{\ell_{A/C}} \right)^{t/2T_o} \qquad (19)$$

where $T_o = \ell_{A/C}/c$. Since $a^x = e^{x \ln a}$,

10

$$\frac{\Delta v_{in}}{v_C} = (1 + \rho_0^{-1}) \exp\left(t \frac{\ln \rho_0 \rho_{\ell A/C}}{2T_0}\right) \quad , \quad (20)$$

which yields an effective exponential time constant of:

$$\tau = \frac{2T_0}{\ln \rho_0 \rho_{\ell A/C}} \tag{21}$$

In our case $|\rho_{\ell A/C}| = 1$ and $|\rho_0| \approx 1$ so that:

$$\ln\left(\rho_0 \rho_{\ell A/C}\right) \approx \rho_0 \rho_{\ell A/C} - 1 \tag{22}$$

which leads to:

$$-\tau = \frac{2T_0}{1 - \rho_0 \rho_{\ell A/C}} = \frac{2T_0}{1 + \rho_0} = \frac{T_0(R_s + 231)}{R_s} \tag{23}$$

or

$$\boxed{-\tau = T_0 + T_0 \frac{231}{R_s}} \tag{24}$$

Now $\frac{231}{R_s} \gg 1$ and $231 = \sqrt{\frac{L}{C}}$; also $T_0 = \ell_{A/C} \sqrt{LC}$ which results in

the time constant finally as $\boxed{-\tau = \ell_{A/C} \frac{L}{R_s} = \frac{\overline{L}}{R_s}}$ which gives $v_{in}(t)$

$$v_{in}(t) = v_C\, e^{\left(-t/\overline{L}/R_s\right)} \text{ where } \overline{L} = \ell_{A/C} L$$

Since $\quad i_{in}(t) = \frac{1}{\overline{L}} \int_{0^-}^{t} v_{in}(\alpha)d\alpha = \frac{v_C}{\overline{L}}\left(1 - e^{-t/\overline{L}/R_s}\right) \quad (25)$

11

the analysis is consistent with the current waveform
derived from the lumped-parameter model.

Observing that $v(t) = 0$ at the "shorted-end" and
also that $\ell_{A/C} \ll \lambda$, it follows that $v(t)$ (peak value) will
increase linearly from the "shorted-end". Furthermore, the
inductance varies linearly as $\overline{L} = L\ell_{A/C}$ so that

$$i_\ell(t) = \frac{1}{L\ell} \int_{0^-}^{t} v(\alpha)\,d\alpha = \frac{\ell}{L\ell} \int_{0^-}^{t} s(\alpha)\,d\alpha \qquad (26)$$

where $s(t)$ is the voltage at $\ell = 1$ meter. It can therefore be
concluded that the skin current, $i_\ell(t)$ will <u>not</u> vary either
in magnitude or waveform along the aircraft $\overline{axis}$. *Except for the
slight decrease in the horizontal current component due to the center
ground rod, these conclusions are confirmed by the skin current measure-
ments.* In closing, the $v(\ell,t)$, $i(\ell,t)$ waveforms are shown in
the following figure.

It should also be mentioned that the 6.8 MHz LST
oscillation can be represented by the "multiple-reflection"
model presented below. Even though $2\ell/c$ is much less than
the L/R rise time of the unipolar pulse, the time-delayed re-
flections do introduce a "square-wave" ripple component on
the current pulse as shown in Figure 15c.

(a)
WAVE FORMS FOR $v(\ell,t)$

$X = \ell_{A/C}$ $X = 0$

(b)
WAVE FORMS FOR $i(\ell,t)$ AS MEASURED BY SKIN CURRENT PROBE
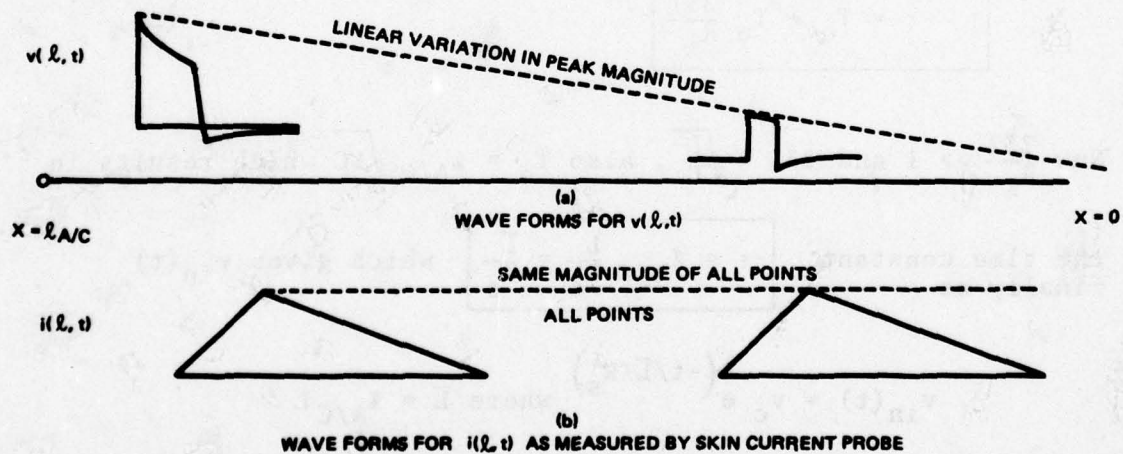
Figure 15. Waveforms for $v(\ell,t)$ and $i(\ell,t)$
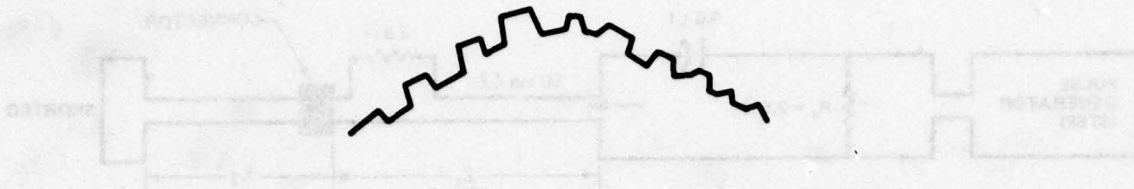
Figure 15c. Example of Square Wave Ripple on Current Pulse

The fundamental period of this ripple is $\frac{2\ell}{c}$ *corresponding to a fundamental frequency of 6.8MHz.* The higher-order harmonics are precisely the higher-order resonance responses corresponding to the series resonant L-C elements presented in the transmission line equivalent circuit in Figure 10. Of course, the 30 MHz fibre-optics instrumentation bandwidth will not pass all the harmonics.

2.3 An RG-58 Cable Simulation of the LST Configuration

2.3.1 General Discussion

Because RG-58 cable is a low-loss transmission line propagating in the TEM mode, the general relationships between current, voltage, etc. should be the same with the RG-58 cabling as with the LST configuration. It is, of course, much easier to work with RG-58 cable since long lengths can be coiled in a convenient manner and different lengths and impedance terminations can be constructed. A great deal of valuable work was done using the RG-58 cable simulation. All of the results of Sections 2.1 and 2.3 were completely verified.

2.3.2 Detailed Discussion

In order to test the LST TEM assumption, the complete LST configuration was simulated using RG-58 coaxial cable. Since the characteristic impedance of the cable is (50/231) of the LST configuration characteristic impedance, all circuit components must be scaled linearly. For convenience, the R_S was reduced from $R_S = 15\Omega$ to $R_S = 2.5\Omega$ and the capacitor, C_S, will be increased from 2.4μf to $\approx$ 10μf. The initial voltage charge will be represented by a step-function voltage generator in series with an initially relaxed capacitor as illustrated in Figure 16.

13
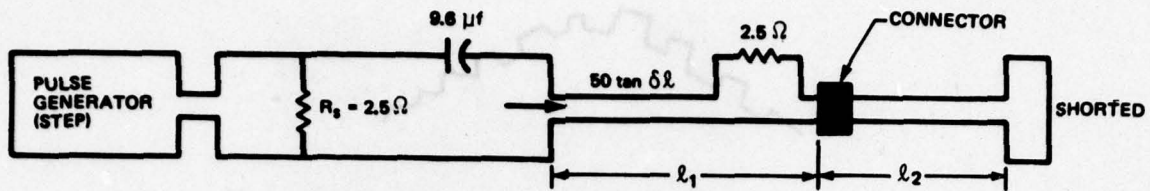
Figure 16.   Test Setup for RG-58 Cable Simulation
of the LST Configuration

One of the most important conclusions is that the
current waveform retains the same magnitude and shape no
matter where it is measured. For a ℓ_1 = 50', ℓ_2 = 6' case,
the current was measured at the end of ℓ_1 and also at R_s.
The measurement at the end of ℓ_1 was made with a voltage
measurement across a 2.5Ω test resistor implanted in the
cable shield. The resulting two current waveforms are, for
all practical purposes, identical as shown in Figure 17.

Top
100 mV/d
(across R_S)

Bottom
100mV/d
(across test
resistor)

ℓ_1=50'

ℓ_2=6'

2μsec/d
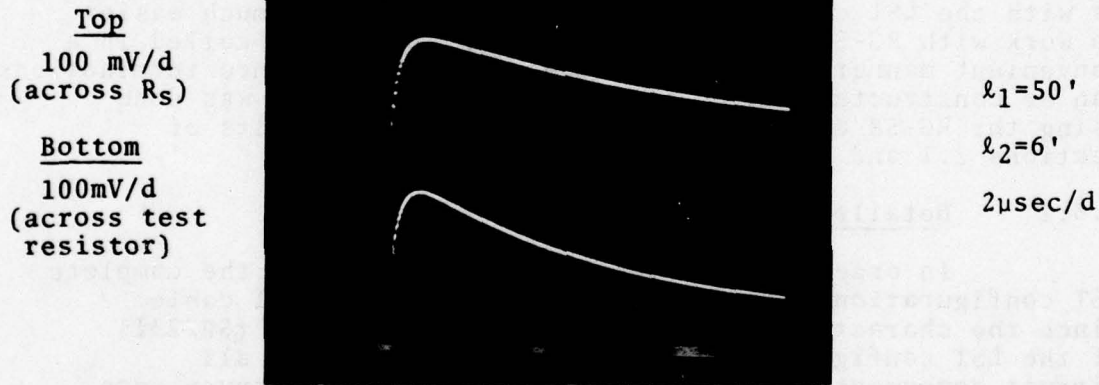
Figure 17.   Comparison of Current Waveforms
at Two Different Distances

For the case of ℓ_1 = 50', ℓ_2 = 0, C_S = 0.1 μf (to
give a shorter fall time), Figure 18 presents a typical
voltage-current waveform pair. It is clear that the voltage
waveform is in fact the time derivative of the current
waveform.

14

Top

Voltage Waveform
200 mV/d

Bottom

Current Waveform
20mA/d

ℓ_1=50'

ℓ_2=0
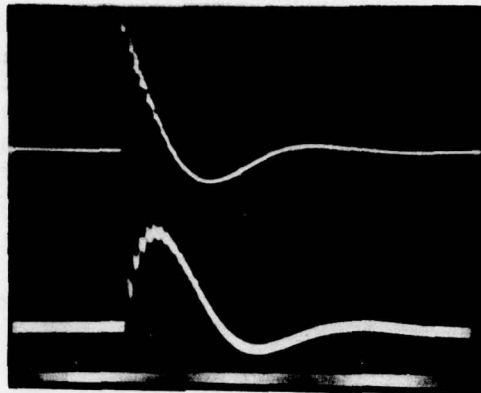
1μsec/d

Figure 18.   Typical Voltage-Current Waveform Pair

As a final verification, the linear dependence with distance of the peak-to-peak value of the voltage waveform was considered.   For a ℓ_1 = 16', ℓ_2 = 6', C_s = 1μf case, voltage waveforms were measured at the beginning of the transmission line and also at the end of the 50 foot section.   The two waveforms of Figure 19 were observed.

Top

Input to
Transmission
Line
(200mV/d)

Bottom

End of 50'
Section
(100mV/d)

ℓ_1=16'

ℓ_2=6'

1μsec/d

Figure 19.   Comparison of Peak-to-Peak Value at
Two Different Distances

The magnitude of the voltage waveforms are in the ratio of
$\frac{\text{Top}}{\text{Bottom}} \approx \frac{400}{120} \approx 3.33$ which compares quite well with the $\frac{22}{6} \approx 3.66$

15

ratio predicted from a linear variation with distance. It
is noted that the linear variation with distance applies
only to the low-frequency, over-damped "pedestal" response.
Superimposed on the low-frequency pedestal is the "reflec-
tion" transient which essentially has the same peak-to-peak
value independent of the point of measurement. The "reflec-
tion" traveling wave is of course more prominent near the
shorted-end where the pedestal is lower.

2.4 Application of Potential Analog Methods to the LST Problem

2.4.1 General Discussion

In order to understand the nature and magnitude of
the internal flux leakage, it is necessary to fully define
the LST skin current density distribution. For the dominant
low frequency components of the current pulse, Kirchoff's
current law must be satisfied at every point on the aircraft
skin. It follows, therefore, that the current density
vector field is the gradient of a scalar field satisfying
Laplace's equation. In the LST configuration, a dominant
cylindrical symmetry is present which permits the use of
two-dimensional potential techniques. One of the most
convenient of the two-dimensional techniques is the resist-
ance paper technique described in the text. With this
technique, some significant electromagnetic properties of
the LST configuration were studied and resolved.

2.4.2 Detailed Discussion

2.4.2.1 Application of the Resistance Paper Method to Predict the Non-uniform Variation of $\vec{J}$ Around the Aircraft Skin

From the continuity relationship, $\nabla \cdot \vec{J} = \partial \rho_s / \partial t$,
we can write:

$$J_x(x) \approx \int_0^x \frac{\partial \rho_s(\tau, t)}{\partial t} \, d\tau \tag{27}$$

which, for $\lambda \gg$ aircraft length, implies that J_x should be
large where ρ_s is large. The determination of ρ_s is straight-
forward given the TEM mode in the LST configuration. It
is straightforward because $\rho_s = E_n$ on the aircraft skin and,
in the TEM mode, $\nabla \times \vec{E} = \nabla \times \vec{H} =$ longitudinal components $= 0$
which then implies that $\vec{E} = -\nabla V$ and that $\nabla^2 V = 0$ in the
charge free region between the fuselage and ground return
paths. In other words, the $\vec{E}$ and $\vec{H}$ fields in a cross-
sectional plane in the TEM mode can be solved from Laplace's
equation, $\nabla^2 V = 0$, given the LST boundary surfaces. The
boundary surfaces are shown in Figure 20.

16
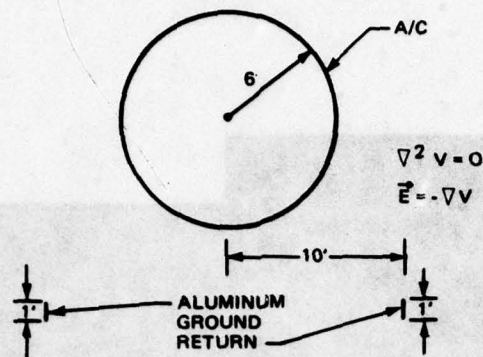
Figure 20.   LST Boundary Surfaces (Cross-Sectional
View of Aircraft)

Two-dimensional potential problems for analyt-
ically intractable boundary surfaces are easily solved using
resistance paper. Since Kirchoff's current law ($\nabla \cdot \vec{J} = 0$)
holds at every point in the paper, $\nabla \cdot (\varepsilon \vec{E}) = \varepsilon \vec{\nabla} \cdot (\nabla V) =$
$\varepsilon \nabla^2 V = 0$ as well, permitting a solution for $v(,)$. Experimen-
tally, the procedure consists of painting the boundary surfaces
on the resistance paper with silver paint, applying D.C.
voltages across the constant potential surfaces, and then mea-
suring the interior voltages with a high impedance D.C. volt-
meter.

The above procedure was performed on the boundary
surfaces of Figure 20 and the constant potential contours of
Figure 21 were plotted. It is clear that there is signifi-
cant "bunching" (i.e. high $E_n = \rho_s$) of the potential lines
at the point on the fuselage NEAREST the ground return path.
*This implies that the observed $\vec{J}$ should be greatest nearest the ground
return and should be at its minimum at the top of fuselage as was in
fact confirmed experimentally.* As it turns out, the $\vec{J}$ variation
around the fuselage (or one set of measurements) follows
quite closely the variation in length of a radius vector
from the center of the ground return to the point of interest
on the aircraft skin.

The variation of $\vec{J}$ around the fuselage could
perhaps have been approached more directly through the $\vec{H}$
vector since $H_{TAN} = \vec{J}$ avoids the use of the continuity
relationship. The two approaches are really equivalent,
however, since $\vec{H} = -\nabla^2 U$ and $\nabla^2 U = 0$, where U is the scalar
magnetic potential, in the TEM mode. Furthermore, $\vec{E}$ and
$\vec{H}$ are orthogonal with their magnitudes in fixed ratios which
allows the same conclusions to be drawn from Figure 21.

17
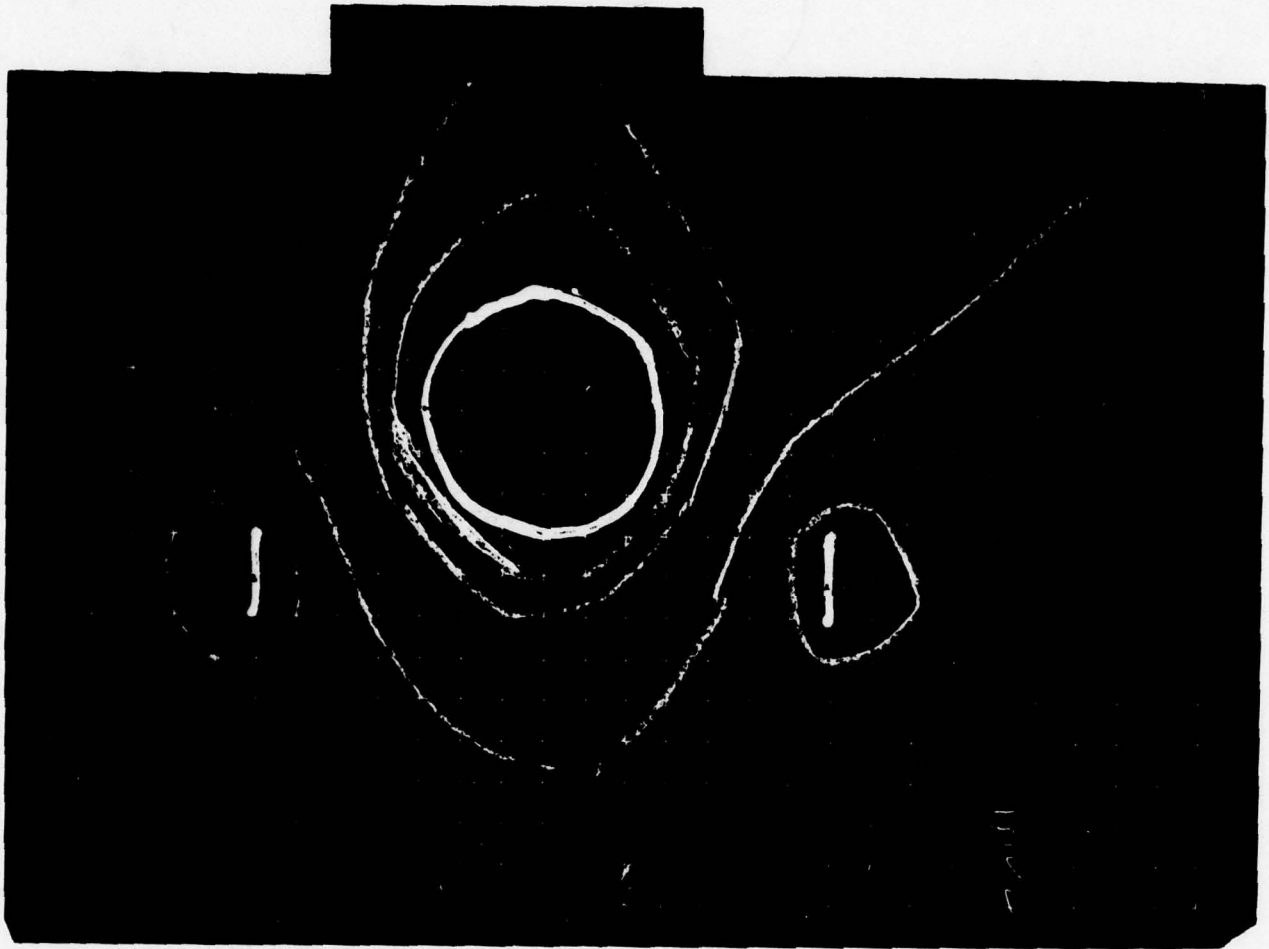
Figure 21. Constant Potential Contours

18

2.4.2.2 Confirming the TEM Assumption by Calculating the Capacitance per Unit Length from the Resistance Paper Model

A convenient feature of the resistance paper is that capacitance per unit length can be related directly to the bulk D.C. resistance actually measured between the boundary surfaces. The actual C and R are related as follows:

$$R C = \frac{\varepsilon_0}{\sigma} \qquad (28)$$

where σ is the known conductivity of the resistance paper.

For the LST configuration of Figure 21, the capacitance is referenced to one of the ground paths as shown:
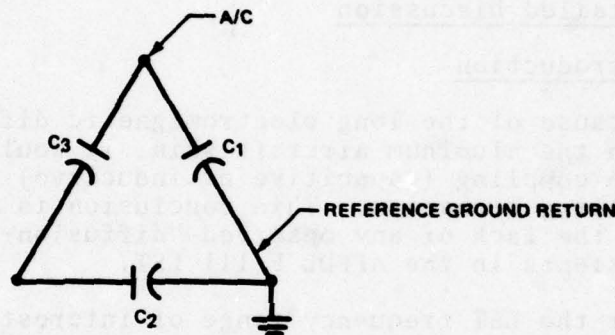
where C_1 is capacitance between aircraft and ground #1,

C_2 is capacitance between ground returns, and

C_3 is capacitance between aircraft and ground #2.

Figure 22.   Capacitance Diagram of Figure 21

Since $C_2 \ll C_1, C_3$, the measured capacitance will be $C \approx C_1$. From the resistance paper, a bulk R of 43K was measured yielding from equation (28) a C of

$$C \approx 2\varepsilon_0 \approx 17 \ pf/m$$

which is greater than the value of the C = 14.4 pf/m predicted from the reciprocity relationship. Stray capacitance in series with the fuselage-ground return configuration along with scaling errors account for the slight difference.

19

3. SMALL APERTURE STUDIES

Significant work has been done on the classical small aperture problem. However, the work has not, in general, been experimental in nature and has not addressed itself to a number of significant questions of great concern to the LTA program. Specifically, the near-field $\vec{E}$ and $\vec{H}$ behavior, and the effects of cavity, panel, strut, etc. shielding have not been considered. This section is an initial attempt at resolving some of those questions.

3.1 Extension of Van Bladel's Work to the Near-Field

3.1.1 General Discussion

The following text represents an analytical approach for near-field calculations that is both general and straight-forward in application.

3.1.2 Detailed Discussion

3.1.2.1 Introduction

Because of the long electromagnetic diffusion times through the aluminum aircraft skin, it would appear that aperture coupling (capacitive or inductive) is the dominant coupling mechanism. This conclusion is further supported by the lack of any observed "diffusion-type" voltage transients in the AFFDL F-111 LST.

For the LST frequency range of interest (f < 30 MHz), all aperture dimensions, including the cockpit, are much less than a wavelength. Apertures of this type are referred to in the literature as "small apertures"; the outstanding property of the small aperture is that the $\vec{E}$ and $\vec{H}$ fields in the aperture will equal, to a good approximation, the $\vec{E}$ and $\vec{H}$ fields which would be observed if the aperture were not present. For the prefectly conducting aircraft skin, $E_{TAN} = 0$ and $H_{NORM} = 0$ (time-varying components), so it follows that $E_{TAN} = H_{NORM} = 0$ in the aperture itself. Further, the H_{TAN} component, at the aperture, will equal the current density, $\vec{J}$, of the neighboring aircraft skin and E_{NORM} will equal $\frac{\rho(t)}{\epsilon_0}$ where $\vec{J}$ and ρ on the aircraft skin are related by the continuity equation, $\nabla \cdot \vec{J} = \frac{\partial \rho}{\partial t}$.

The "small aperture" problem is a classical problem that is still to some extent an active research area despite the simplifying assumptions. The "time-honored" approach (H. A. Bethe, 1944) to the problem is to represent the penetrating $\vec{E}$ and $\vec{H}$ as generated by electric charges and currents, and fictitious

20

magnetic charges and currents lying within the aperture itself.
Since magnetic charges and currents have never been observed
physically, it is necessary, at this point, to provide a back-
ground and a motivation for this approach. The fundamental
theoretical justification for the approach is an underlying
symmetry of the Maxwell's equations that leads to the "Field
Equivalence Theorem" advanced by Schelkunoff (Ref. 16).
Essentially the magnetic and electric charges are postulated
in the aperture to account for the step discontinuity in
both E_{TAN} and H_{NORM} at the aperture plane as shown in Figure 23.
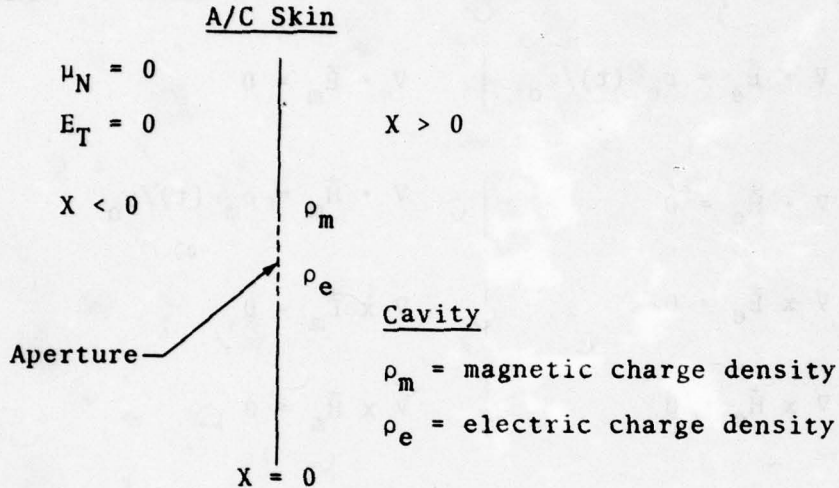
Figure 23. Aperture Plane

Using the equivalence relationship, the $\vec{E}$ and $\vec{H}$
inside the cavity can be decomposed into respective components
$\vec{E}_m$, $\vec{H}_m$, $\vec{E}_e$, $\vec{H}_e$, such that $\vec{E} = \vec{E}_e + \vec{E}_m$ and $\vec{H} = \vec{H}_e + \vec{H}_m$ where the
respective components obey the following symmetrical sets of
Maxwell's equations:

$$\nabla \cdot \vec{E}_e = \rho_e \quad \bigg| \quad \nabla \cdot \vec{E}_m = 0$$

$$\nabla \cdot \vec{H}_e = 0 \quad \bigg| \quad \nabla \cdot \vec{H}_m = \rho_m/\mu_o$$

$$\nabla \times \vec{E}_e = -\mu_o \frac{\partial \vec{H}_e}{\partial t} \quad \bigg| \quad \nabla \times \vec{E}_m = -\vec{J}_m - \mu_o \frac{\partial \vec{H}_m}{\partial t} \qquad (29)$$

$$\nabla \times \vec{H}_e = \vec{J}_e + \varepsilon_o \frac{\partial \vec{E}_e}{\partial t} \quad \bigg| \quad \nabla \times \vec{H}_m = \partial_o \frac{\partial \vec{E}_m}{\partial t}$$

Since every important dimension of our problem is much less than a wavelength, the radiation terms are zero and the situation reduces to the quasi-static region of electromagnetics. In addition, the continuity equations, $\nabla \cdot \vec{J}_e = \frac{\partial \rho_e}{\partial t}$ and $\nabla \cdot \vec{J}_m = \frac{\partial \rho_m}{\partial t}$, imply that the effects of $\vec{J}_m$, $\vec{J}_e$ are negligible when compared to the ρ_m, ρ_e effects in regions with dimensions much less than the wavelength, λ. Accordingly, the equations reduce to

$$\nabla \cdot \vec{E}_e = \rho_e(t)/\varepsilon_o \quad \bigg| \quad \nabla \cdot \vec{E}_m = 0$$

$$\nabla \cdot \vec{H}_e = 0 \quad \bigg| \quad \nabla \cdot \vec{H}_m = \rho_m(t)/\mu_o \qquad (30)$$

$$\nabla \times \vec{E}_e = 0 \quad \bigg| \quad \nabla \times \vec{E}_m = 0$$

$$\nabla \times \vec{H}_e = 0 \quad \bigg| \quad \nabla \times \vec{H}_m = 0$$

The above equations are most interesting since they imply that $\vec{H}_e = 0 = \vec{E}_m$ for $x > 0$ and that $\vec{E}_e$ and $\vec{H}_m$ are gradients of magnetic and electric scalar potentials generated, respectively, by electric and magnetic charge distributions lying within the aperture. Such an interpretation leads to many simplifications. For example, as the offset distance from the aperture increases, the continuous charge distributions can be well represented by orthogonal electric and magnetic dipoles. Indeed, this has been the usual approach taken in LTA analysis (e.g., References 5 and 13), and it is a valid approach provided the offset distances are large compared to the aperture. Unfortunately, this is not always true for the larger apertures and major errors could well be introduced by continuing to regard the aperture as a dipole when observing to within a few feet of the aperture plane itself. The accuracy of the dipole approximation can only be determined by a comparison with the correct method and ultimately through an experimental test procedure presented in a later section of this report.

3.1.2.2 Correct Procedure for Calculating $\vec{H}$ in a Cavity Near a Small Aperture

Continuing with the above discussion, the $\vec{H}$ field can be expressed as the gradient of a scalar potential ($\nabla \times \vec{H} = 0$), $\psi(r)$, where $\psi(r)$ can be expressed as Eq. 20 of Van Bladel:

$$\psi_a(\overline{r}) = \frac{1}{2\pi} \int\int_{\text{Aperture}} \frac{\partial\psi(\overline{r}')}{\partial n'} \frac{1}{|\overline{r} - \overline{r}'|} dS' \qquad (31)$$

where

$$\frac{\partial\psi(\overline{r}')}{\partial n} \bigg|_{\text{at aperture}} = \boxed{H_n = \frac{1}{2} \rho_m(\overline{r}') H_0} \qquad (32)$$

where $H_0 = J_s$, the LST aircraft surface current density.

The important $\rho_m(\overline{r}')$ can be calculated on the charge distribution required to impose the condition $H_{TAN} = 0$ along the aperture. Taking every aperture as circular, the $\rho_m(\overline{r}')$ has been calculated by Bethe as:

$$\rho_m(\overline{r}') = \frac{4}{\pi} \frac{\overline{\mu}'}{\sqrt{a^2 - \overline{r}'}} \qquad (33)$$

where a is radius of the aperture.

The above integral is to be solved in spherical coordinates as shown in Figure 24. The origin is at the center of aperture.
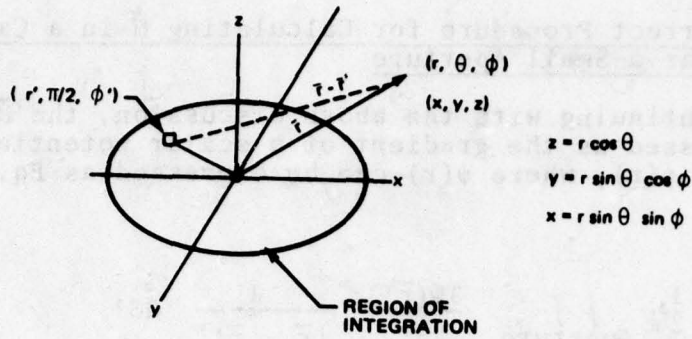
Figure 24. Spherical Coordinates

It is apparent from analytic geometry that:

$$\frac{1}{|\bar{r} - \bar{r}'|} = \frac{1}{\sqrt{(4\cos\theta)^2 + (r\sin\theta\cos\phi - r'\cos\phi')^2 + (r\sin\theta\sin\phi - \mu'\sin\phi')^2}}$$

(34)

The function $\psi_a(r)$ can then be written, for a fixed (r,θ,ϕ), as the iterated integral:

$$\psi_a(\mu,\theta) = \frac{2J_s}{\pi} \int_0^{a-\delta} \frac{r'^2\, dr'}{\sqrt{a^2 - r'^2}} \int_0^{2\pi} f(r,\theta;\phi',r')d\phi' \quad (35)$$

where δ is a small positive quantity designed to avoid the singularity at $r' = a$ and $f(r,\theta,\phi')$ is the above function

$\frac{1}{|\bar{r}-\bar{r}'|}$. Only the r,θ are listed since it is clear that

$\psi_a(r,0)$ has ϕ spherical symmetry (i.e., set $\phi = 0°$ in equation 35 above).

24

Solution of Eq. 35 for various r's and plotting
will result in Figure 25.
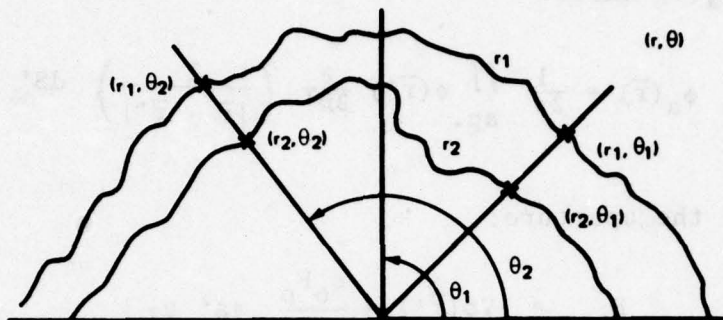
Figure 25. Sample Computer Output

$\vec{H}$ can then be immediately calculated from the above figure
as:

$$\vec{H} = \text{gradient } \psi_a(r, \theta) = \frac{\partial \psi}{\partial r}\vec{a}_r + \frac{1}{r} \frac{\partial \psi}{\partial \theta}\vec{a}_\theta \qquad (36)$$

This solution for $\vec{H}$ is valid for any point within a distance
$\ll \lambda$ from aperture.

As was mentioned in Section 3.1.1.1, $\psi_a(r,\theta)$ should
approach the classic dipole potential field as the observa-
tion point gets further from the aperture. In this case,
there are two magnetic dipoles at right angles aligned along
the principal axes of the aperture. Both dipoles have a

magnetic moment equal to $k H_0 = k J_S$ where $k = \frac{2a^3}{\pi}$ (Bethe).
It would be of interest to calculate $\psi_a(r,\theta)$ from the dipole

model and observe at what ratio of $|\bar{r}|/a$ the results begin to
diverge. It would be desirable if the dipole model could be
retained well into the near-field since dipoles can be easily
represented with potential analog ($\nabla^2\psi = 0$) methods; e.g.,
Telledeltos or resistance paper (Ref. 11). In particular,
resistance paper methods can simulate conductive struts and
panels inside the aircraft cavity. This convenient feature
permits a study of any resulting field distortion. More
will be said about the resistance paper method in later
sections.

25

3.1.2.3 Correct Procedure for Calculating $\vec{E}$ in a Cavity Near a Small Aperture

The solution for the $\vec{E}$ field due to aperture coupling is quite analogous to the above solution for $\vec{H}$. According to equation (35) by Van Bladel, the $\vec{E}$ in the neighborhood of the aperture can be expressed as the gradient of $\phi_a(\bar{r})$ where:

$$\phi_a(\bar{r}) = \frac{1}{2\pi} \iint_{ap.} \phi(\bar{r}') \frac{\partial}{\partial n'} \left(\frac{1}{|\bar{r} - \bar{r}'|} \right) dS' \qquad (37)$$

where on the aperture:

$$E_{tan} = -\nabla\phi(\bar{r}') = \frac{\varepsilon_o E_o}{\partial\varepsilon_o} \pi a^2 \nabla\tau \qquad (38)$$

where the plane of definition of the τ function is orthogonal to the aperture plane. From inspection, it follows that:

$$\phi(\bar{r}') = \frac{E_o \sqrt{\pi} a}{2} \tau \qquad (39)$$

where τ is a function defined to maintain $E_n = E_0/2$. The τ function can be derived from the basic potential theory as:

$$\tau(r) = \frac{2}{\pi\sqrt{\pi}} \sqrt{1 - \frac{r^2}{a^2}} \qquad (40)$$

to yield the final expression for $\phi(\bar{r}')$ given as:

$$\phi(r') = \frac{E_o}{\pi} a \sqrt{1 - \frac{r'^2}{a^2}} \qquad (41)$$

The second term of the integrand of Eq. 37 contains the interesting term, $\frac{\partial}{\partial n'}$, $\frac{1}{|\bar{r}-\bar{r}'|}$, which is the normal component of the gradient of $\frac{1}{|\bar{r}-\bar{r}'|}$.

26

Referring to the geometry below:
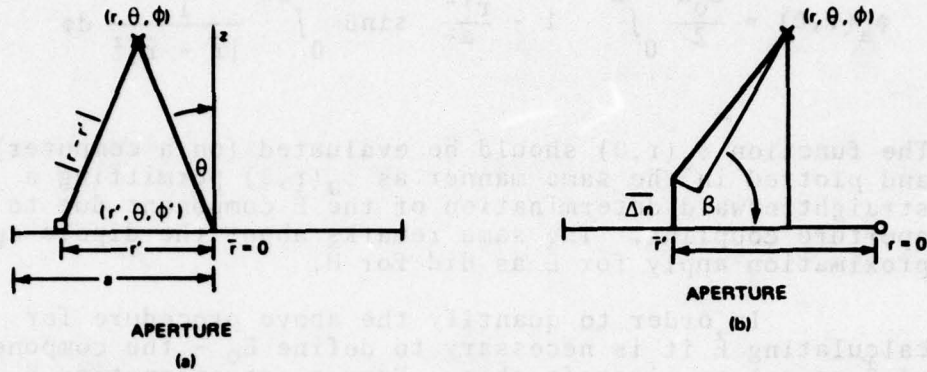
Figure 26. Aperture Geometry

it can be shown from simple trigonometry that an infinitesimal normal increment, Δn, produces an incremental change in $|\bar{r}-\bar{r}'|$ equal to:

$$\Delta s = \Delta n \sin \beta \text{ where}$$

$$\beta = \tan^{-1} \left[\frac{r' - r \sin \theta}{r \cos \theta} \right]$$

to give, from the $\frac{1}{x}$ form in differential calculus:

$$\frac{\partial}{\partial n} = \left[\frac{1}{|r - r'|} \right] = \frac{\sin \beta}{|r - r'|^2}$$

where the expression for $|\bar{r}-\bar{r}'|$ is given in the previous section. The final expression for $\phi(\bar{r})$ becomes:

$$\phi_a(r, \theta) = \frac{E_o a}{4\pi} \iint_{\text{aperture}} \sqrt{1 - \frac{r'^2}{a^2}} \frac{\sin \beta}{|\bar{r} - \bar{r}'|^2} dS' \qquad (42)$$

27

where dS' = 2πr'dr'. The expression can be written in iterated form as (φ = 0):

$$\phi_a(r,\theta) = \frac{E_o a}{2} \int_0^a \left(1 - \frac{r'^2}{a^2}\right) \sin\beta \int_0^{2\pi} \frac{1}{|\bar{r} - \bar{r}'|^2} \, d\phi \qquad (43)$$

The function $\phi_a(r,\theta)$ should be evaluated (on a computer) and plotted in the same manner as $\psi_a(r,\theta)$ permitting a straightforward determination of the $\vec{E}$ component due to aperture coupling. The same remarks about the dipole approximation apply for $\vec{E}$ as did for $\vec{H}$.

In order to quantify the above procedure for calculating $\vec{E}$ it is necessary to define E_o - the component of $\vec{E}$ normal to aircraft skin. From electromagnetics $E_n = \rho_s/\varepsilon_0$, the electric charge density on skin, which can in turn be derived from the continuity equation:

$$\nabla \cdot \vec{J} \approx \frac{\partial J}{\partial x} \approx \frac{\partial \rho_s}{\partial t}, \qquad (44)$$

where x lies along the aircraft axis. Repeated skin current measurements at different axis locations have suggested the separable form (for f < 5 MHz at least) given as:

$$J(x,t) = g(x) \, s(t) \qquad (45)$$

with:

$$0 \le s(t) \le 1$$

Therefore:

$$\frac{\partial J}{\partial x} \approx \frac{dg}{dx} \, s(t) \approx \frac{\partial \rho_s}{\partial t}$$

so that:

$$\rho_s(t) \approx \frac{dg}{dx} \int_{0^+}^t s(\tau) d\tau \qquad (46)$$

for a 2000 amp peak current and a 6 foot diameter aircraft body, $\frac{dg}{dx} \approx 88$ amps/m^2 so that:

28

$$E_n(t) \approx \frac{88}{\varepsilon_o} \int_{0^+}^{t} s(\tau) d\tau \qquad (47)$$

For a phasor analysis, with $s(t) = e^{+j\omega t}$,

$$E_o(t) \approx \frac{88}{j\omega\varepsilon_o} e^{j\omega t}$$

3.2 Experimental Investigation of Small Aperture Problem Using a CW Yoke Coil Approach

3.2.1 General Discussion

A novel experimental approach to the small aperture problem has been conceived and implemented. By simulating the peripheral skin current density with a yoke coil, a simple but accurate method has been developed to analyze near and far field effects as well as shielding.

3.2.2 Detailed Discussion

3.2.2.1 Design for the H-Field Test

The chosen approach is to simulate the aircraft skin current effects by establishing a comparable skin current density in a region close to the aperture. Such an approach avoids the high-current drive requirements of the capacitor bank and allows CW (sine wave) operation. The approach is based on the reasonable assumption that only current density components near the aperture will generate leakage $\bar{E}$ or $\bar{H}$ flux internal to the aircraft.

The local current density is established by a yoke coil positioned around the periphery of the aperture as shown in Figure 27.
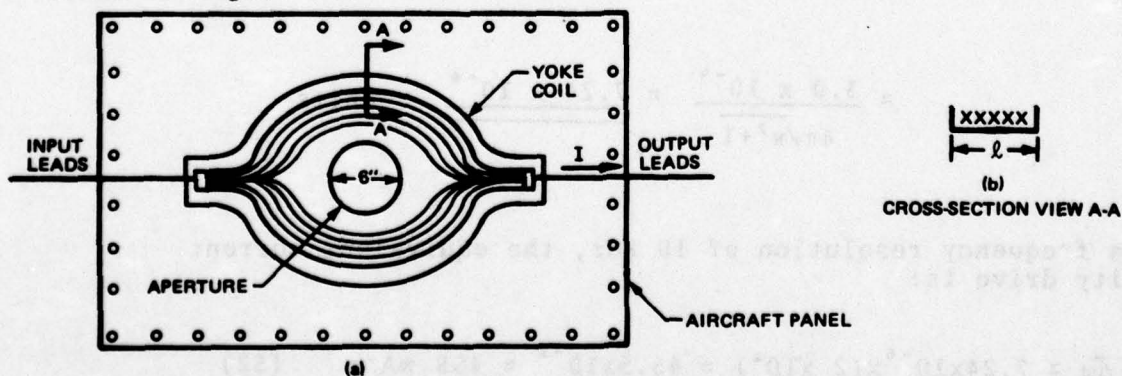
Figure 27. Yoke Coil on the Periphery of an Aperture

29

From Figure 26, the simulated current density, J, equals:

$$J = \frac{NI}{2\ell} \qquad (48)$$

where I is the current through the coil. Unfortunately, for a reasonable N, the peak J (2200 amp/m) for unipolar pulse operation requires ($\ell = 6"$) currents greater than 1 amp which cannot be conveniently delivered by most pulse generators. Fortunately, it is not necessary to deliver the entire J_{peak} to the aperture periphery. Instead, we can consider $J(t)$; from its inverse fourier transform, as a superposition of sine waves ($-\infty < t$) as follows:

$$J(t) \approx \frac{1}{2\pi} \int_{-\infty}^{\infty} J(\omega)\, e^{j\omega t}\, d\omega \approx \sum J(\bar{\omega})\, e^{j\bar{\omega}t}\, \Delta f \qquad (49)$$

Continuing with the experimental design, the Fourier transform of J(t), for an aircraft circumference of 8m, can be expressed as

$$|J(\omega)| \approx \frac{E/8L}{|\omega|\ |j\omega + R/L|} \qquad (50)$$

or for $f = 10^6$, $R/L = 2 \times 10^6$, $E = 40,000$, $L = 17\mu h$,

$$J(\bar{\omega})\Big|_{\omega = \bar{\omega} = 2\pi \times 10^6} \approx \frac{3 \times 10^8}{(2\pi \times 10^6)\ \sqrt{(2\pi \times 10^6)^2 + (2 \times 10^6)^2}} \qquad (51)$$

$$\approx \frac{3.0 \times 10^{-4}}{4\pi\sqrt{\pi^2 + 1}} \approx \underline{7.24 \times 10^{-6}} \quad \text{units}$$

For a frequency resolution of 10 kHz, the equivalent current density drive is:

$$J(\bar{\omega})\,\overline{\Delta \omega} \approx 7.24 \times 10^{-6} \times (2 \times 10^4) \approx 45.5 \times 10^{-2} \approx 455 \text{ mA/m} \qquad (52)$$

From equation (48) with L = 6", N = 5, the calculated I equals:

$$\boxed{I = (0.455)\ 2L/N = 28\ mA} \tag{53}$$

which is a reasonable current drive level.

For our intended 6" circular test aperture, the inductance of the yoke coil can be calculated from the formula:

$$L/m = \frac{\mu_o\ N^2}{\pi}\ \ln\left[\frac{h-r}{r}\right] \tag{54}$$

where N = 5, h = 6", r = 1 mil (wire thickness), L/m = 4 x 10^{-7} x 25 ln [6000] = 87 µh/m or, for a width of 0.16 m, an overall:

$$\bar{L} = 14\ \mu h \qquad \text{(to be checked experimentally)}$$

At a frequency of 1 MHz, the required C for series-resonance is given by:

$$C = \frac{1}{4\pi^2\ f^2\ L} = 1.81 \times 10^{-9}\ f \tag{55}$$
$$= 1800 \times 10^{-12}\ f$$

which can be realized simply.

The pick-up coil should have a diameter around one centimeter since it must be physically small compared to the dimensions of the aperture and aircraft cavity. The open-circuit voltage of the coil, v_{oc}, can be expressed as:

$$v_{oc} = \omega\ A\ H_{INT}\ \bar{N}\ \mu_o \tag{56}$$

where $\bar{N}$ equals the number of turns in the pick-up coil and A is its cross-sectional area. For an $\bar{N}$ = 20 (any more would be physically awkward), the:

31

$$v_{oc} = 1.24 \times 10^{-2} H_{INT} \text{ volts.}$$

To provide a rough estimate of H_{INT}, we turn to Van Bladel's expressions for the equivalent aperture magnetic dipole. According to these expressions, the dipole moment can be expressed as:

$$\rho_m = 2 H_o v_m S^{3/2} = 2 \times 2.46 \times 10^{-3} \times 0.479 H_o \quad (57)$$

$$= 2.36 \times 10^{-3} H_o$$

The H_{INT} can be conveniently expressed as:

$$H_{INT} \simeq \frac{1}{4\pi} \rho_m \text{ grad} \left(\frac{\cos \theta}{R^2} \right) \simeq \frac{\rho_m}{4\pi R^3} \quad (58)$$

which for a worst case of $R = 1$ m equals:

$$H_{INT} \simeq 0.188 \times 10^{-3} H_o \quad (59)$$

to give for $H_o = 0.48$ amp/m. An open circuit voltage, v_{oc}, from equation (56):

$$v_{oc} \simeq 0.188 \times 10^{-3} \times 1.24 \times 10^{-2} \text{ volts}$$

or:

$$v_{oc} = 2.33 \text{ } \mu\text{volts}$$

While microvolt levels can be dealt with, it may be desirable to increase the v_{oc} by at least a factor of 10. Since it is the ratio of $\frac{H_{INT}}{H_o}$ that is desired, there is no compelling reason to insist on matching the $J(\omega) \Delta\bar{\omega}$ of the unipolar pulse. Accordingly, the current drive can be in-

creased to 320 mA (available with a conventional oscillator), the "pick-up" coil area, A, by a factor of 6.45 (diameter of 1") to give an increased open circuit voltage of:

$$v_{oc} = \underline{78 \text{ }\mu\text{volts}} \quad \text{which is easier to work with.}$$

Using an op-amp video preamplifier with a voltage gain of 100, the experimental set-up would appear as follows:

YOKE DRIVE
(a)

PICK-UP COIL
(b)
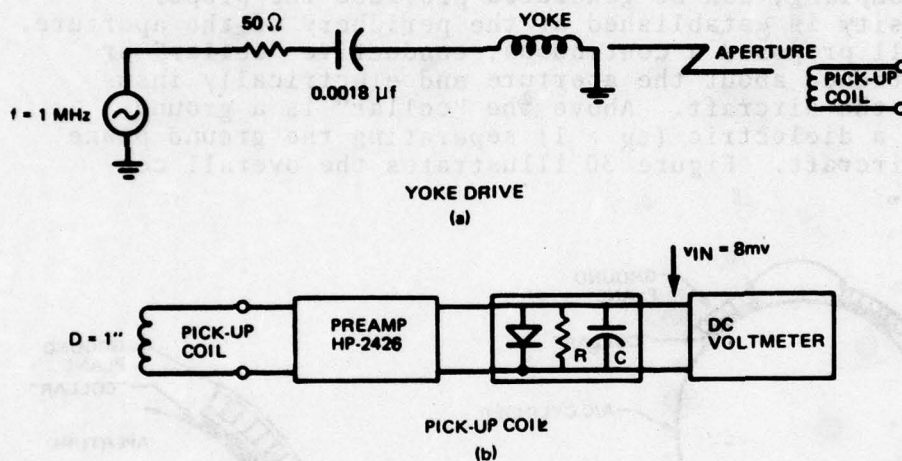
Figure 28. Yoke Coil Experimental Circuits

The RC time constant of the envelope detector is set at 10^{-2} sec. (Δf = 10 kHz). In the event of S/N problems, the following steps can be taken:

a. Using a simple auto transformer (see Figure 29) current gains of 10 = n_1/n_2 should be attainable.
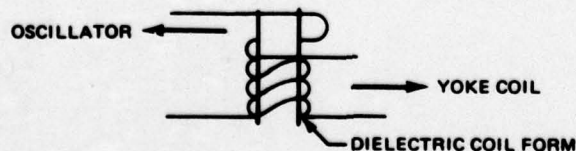
Figure 29. Autotransformer Circuit

33

b. Lowering the bandwidth by a factor of 100 will give a S/N increase of 10.

c. By increasing N, ω, A, $\bar{N}$, the induced signal can be increased, but these changes will require adjustments in the above circuit (e.g., N = 20 implies a C of 112 pf and an improvement factor of 4).

d. Synchronous detection with lock-in amplifier

3.2.2.2 Design for the $\vec{E}$-Field Test

As with the magnetic field, $\vec{H}$, the $\vec{E}$ field, due to aperture coupling, can be generated provided the proper charge density is established at the periphery of the aperture. Reference 11 proposed a continuous, conductive "collar" or sheet positioned about the aperture and electrically insulated from the aircraft. Above the "collar" is a ground plane with a dielectric ($\epsilon_R > 1$) separating the ground plane from the aircraft. Figure 30 illustrates the overall configuration.
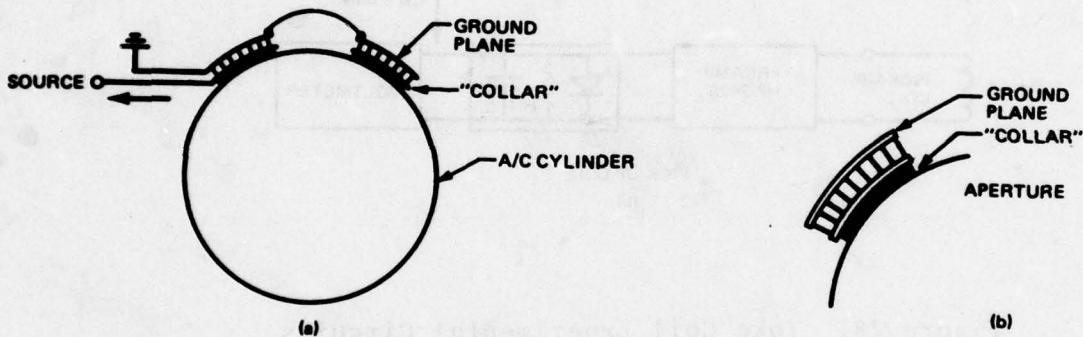
Figure 30. Continuous Conductive Collar Configuration

Assuming a TEM mode, resistance paper analog methods have indicated that the field pattern in the configuration of Figure 30 is quite similar to the actual LTA pulse situation. The resulting capacitance of the configuration, C_T, can be expressed as:

$$C_T = C_1 + (C_2||C_3) \qquad (60)$$

34

where: C_1 is the capacitance of the collar to ground;

C_2 is the capacitance of the collar to the aircraft;

and: C_3 is the capacitance of the aircraft to ground.

Since C_1, $C_2 \gg C_3 \approx 10$ pf, it follows that $C_T \approx C_1$.

Assuming a worst case analysis where the aperture is near the cockpit, the voltage (LST) between the aircraft and ground return, in the pulse mode, has a time dependence $\approx \frac{di}{dt}$ and an initial peak value of 40,000 volts. With a separation distance of 3m, the maximum $E_n = 1.33 \times 10^4$ volts/m so that:

$$\sigma = D_n = \epsilon_o E_n = 11.77 \times 10^{-8} \text{ coulomb/m}^2 \qquad (61)$$

where D_n is electric flux density.

For a collar about a 6" diameter aperture with a 6" width, the collar area = A = 0.145 M^2 to give a charge on the collar equal to:

$$Q = \sigma A = 1.71 \times 10^{-8} \text{ coulomb} \qquad (62)$$

Using a dielectric spacer with a relative dielectric constant, ϵ_R, equal to 6, the capacitance of the collar to ground equals:

$$C_T = \frac{\epsilon_R \epsilon_o A}{d} = 774 \text{ }\rho f \qquad (63)$$

The voltage across this capacitance is then:

$$v = Q/C_T = \frac{1.71 \times 10^{-8}}{774 \times 10^{-12}} = 22.1 \text{ volts} \qquad (64)$$

Accordingly, at some frequency, ω, we must drive C_T hard enough to reach 22 volts at its positive peak. A useful compromise frequency, f, is 500 kHz which gives a current requirement of:

$$I \approx (\omega C_T) \; 22 \approx 2\pi \times 5 \times 10^5 \times 7.74 \times 10^{-10} \times 22$$

$$\approx 542 \times 10^{-10} = 5.42 \text{ mA} \qquad (65)$$

To provide series resonance at f = 500 kHz, we need an L equal to:

$$L = \frac{1}{4\pi^2 \; f^2 \; C_T} = 130 \; \mu h \qquad (66)$$

which is a very convenient value.

The $\vec{E}_{INT}$ can be measured with a small dipole. The expected signal levels can be calculated using the electric dipole expressions of Van Bladel. From Equation 8 in Reference 11:

$$\bar{\rho} = 2 \; \epsilon_o \; S^{3/2} \; E_o \; \tau_{av}$$

A rough approximation for $|\vec{E}|$ can be determined for $\mu = 1m$ as:

$$|\vec{E}_{INT}| = \frac{\bar{\rho}}{4\pi\epsilon_o r^3} = \frac{2S^{3/2} \; E_o \tau_{av}}{4\pi} \approx 9.43 \times 10^{-4} \; E_o \qquad (67)$$

For our originally assumed $E_n = 1.33 \times 10^4$ volts/m, $|E_{INT}|$ will then equal:

$$|E_{INT}| \approx 1.25 \text{ v/m} \qquad (68)$$

which will provide, for a 1 cm dipole, the open circuit voltage:

$$v_{oc} \approx E_{INT} \; \ell \approx 12.5 \text{ mV} \qquad (69)$$

36

which suggests that a pre-amp may be avoided given a sensitive enough scope amplifier. The final circuit is essentially that as proposed for the magnetic field, $\vec{H}$, measurement.

The above yoke coil experiment was implemented using an F-111 cavity. The predicted levels were observed. A useful series of near-field measurements was made and are presented in the next section. Much more additional useful work can be done with the yoke coil approach.

3.3 Application of Two-Dimensional Potential Methods to the Analysis of Near-Field and Shielding Effects

3.3.1 General Discussion

Because the $\vec{E}$ and $\vec{H}$ fields in a current-free region are gradients of scalar potential fields in the low frequency quasi-static case, it is possible to apply traditional potential theory techniques to evaluate $\vec{E}$ and $\vec{H}$. With the simplifying assumption of cylindrical symmetry, the two-dimensional potential techniques of resistance paper and the conjugate harmonic method become applicable. These methods have been applied and have been found to agree with the yoke coil experimental results.

3.3.2 Detailed Discussion

3.3.2.1 Introduction

For the case of the long aperture or "slot," symmetry alone requires that the $\vec{E}$ and $\vec{H}$ fields be transverse (i.e., no axial components). With transverse $\vec{E}$ and $\vec{H}$ fields, the curl of both $\vec{E}$ and $\vec{H}$ is zero in the transverse plane, and both fields can then be represented as gradients of scalar potential fields. Furthermore, the $\vec{E}$ and $\vec{H}$ fields will be orthogonal in the transverse plane and will maintain a constant magnitude ratio, $|\vec{E}|/|\vec{H}|$, throughout the plane.

Given the above properties of the TEM mode, it then becomes possible to analyze aperture coupling and shielding in one step. All that is required is a potential function solution ($\nabla^2 V = 0$) for the geometry in question. Referring to Figure 31, the LST cross section is shown where the region of solution is now the interior of the fuselage instead of the exterior. Because the $\vec{H}$ field is orthogonal to the $\vec{E}$ field, the constant electric potential contours will correspond to $\vec{H}$ field streamlines. The dipole nature of the $\vec{H}$ streamlines can be observed in Figure 31. Also, the termination of the $\vec{H}$ streamlines on "fictitious" magnetic charges in the aperture plane is apparent, which then suggests the possibility that near-field effects can now be analyzed with a resistance paper approach.
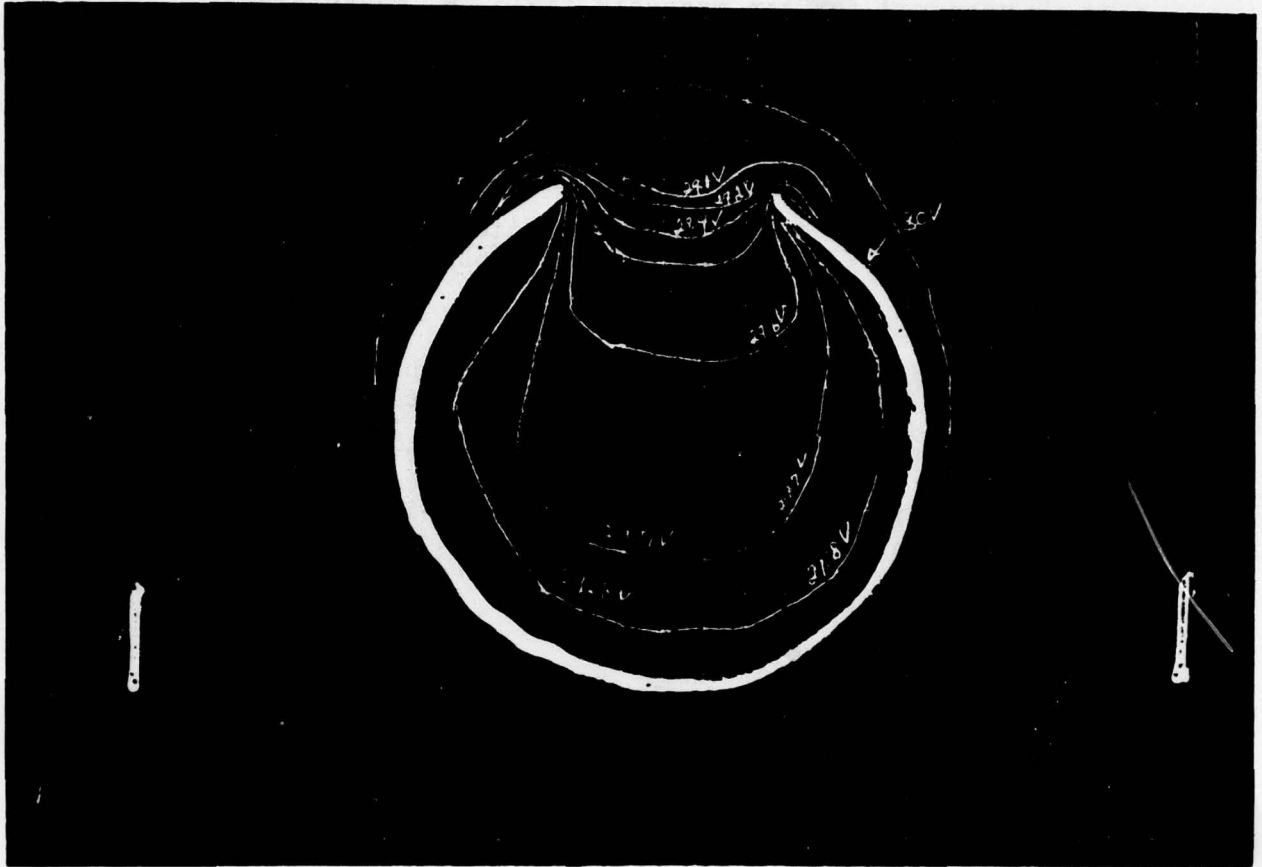
37

Figure 31.   Constant Electric Contours in the Interior

Although the TEM assumption can only be an approximation for the more common circular aperture, the advantages of the method are considerable since near-field and shielding effects can now be treated as well as the analytically intractable field distortion effects due to internal struts, panels, etc. The following sections develop the TEM method and also present some actual yoke-coil experimental results.

3.3.2.2 Added Justification for the TEM Assumption and a Discussion of the Near-Field Effect

Since $\vec{E}$ and $\vec{H}$ field penetration, in the small aperture case, has been well approximated in the far-field by the dipole model, it was reasonable to investigate the effects of shielding using the dipole itself. For the magnetic field case of Figure 32, a dipole was formed in the aperture plane and the $H_{NORM} = 0$ boundary condition was imposed by cutting the circular boundary out of the resistance paper. The constant potential lines in Figure 32 are not $\vec{H}$ streamlines but are instead contours of constant magnetic potential. Close inspection of the solution without shielding (solid line) and the solution with shielding (dashed line) suggests the general effect of the aluminum fuselage. The electric dipole case is presented in Figure 33 with the distorted $\vec{H}$ streamline indicating the shielding effect of the induced surface currents. A comparison of Figure 31 with Figures 32 and 33 suggests that the LST geometry (TEM mode) will yield $\vec{E}$ and $\vec{H}$ field patterns very similar to those of the dipole model. This tends to support the original TEM assumption.

A more quantitative support for the TEM model is provided by a study of the near-field pattern. Figure 34 plots the ratio v_{n-1}/v_n along the traverse perpendicular bisector of the aperture plane using measured values from the resistance paper (RP) model and also including values from the ideal dipole. *The important observation is that the ratio v_{n-1}/v_n is relatively constant for the TEM RP model over the near-field region, suggesting that the near-field variation for the small aperture is actually EXPONENTIAL in nature* (Ke^{-kx}). The apparent exponential behavior in the near-field is not mentioned in the open literature reviewed. Yet it is of potential significance to the LTA program. The ratio v_{n-1}/v_n in the far-field is also of interest since it illustrates the shielding effects of the induced surface currents. In particular, the increase in v_{n-1}/v_n near the fuselage boundary is the result of lower field levels caused by an opposing field component developed by the induced skin currents.

Recent yoke-coil experiments fully support the exponential variation in the near-field. With a circular 6" aperture, the normalized (X = 0) near-field measurements are given along with the exponential variation in Table I.
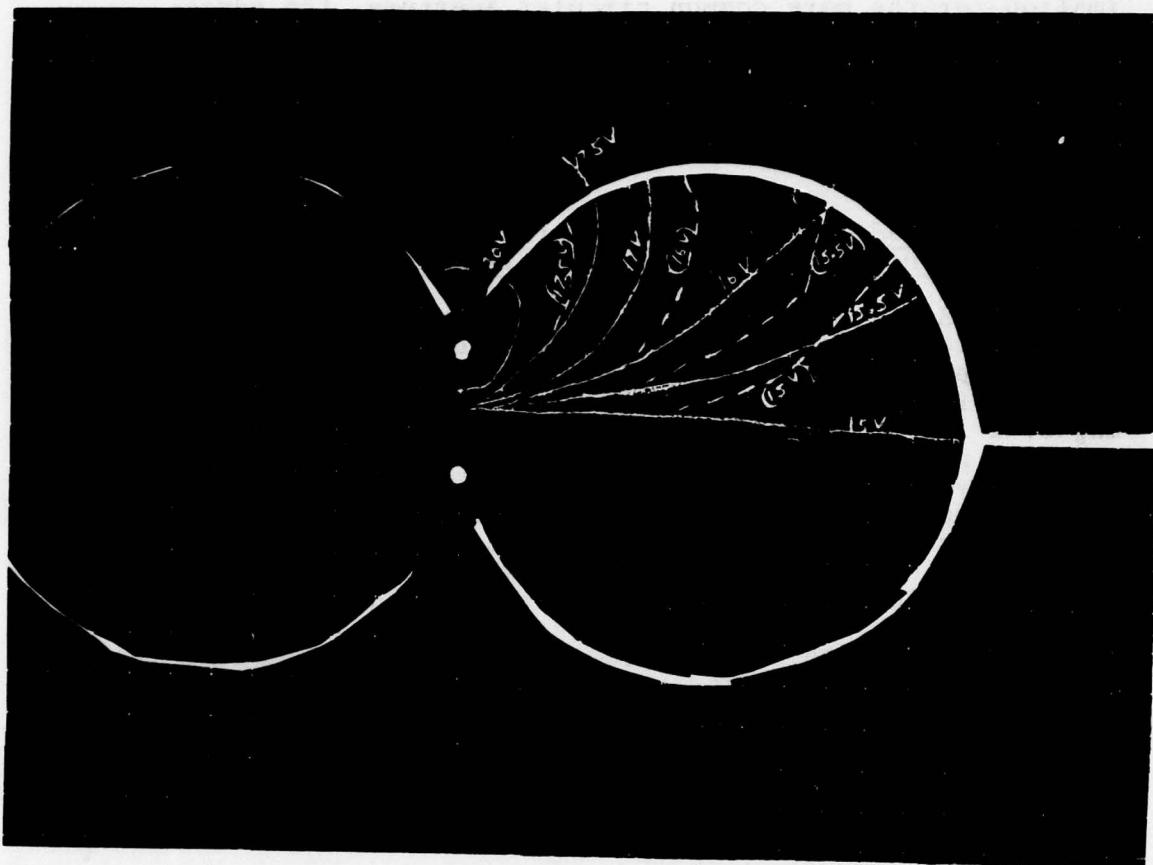
Figure 32.   Constant Magnetic Potential Contours
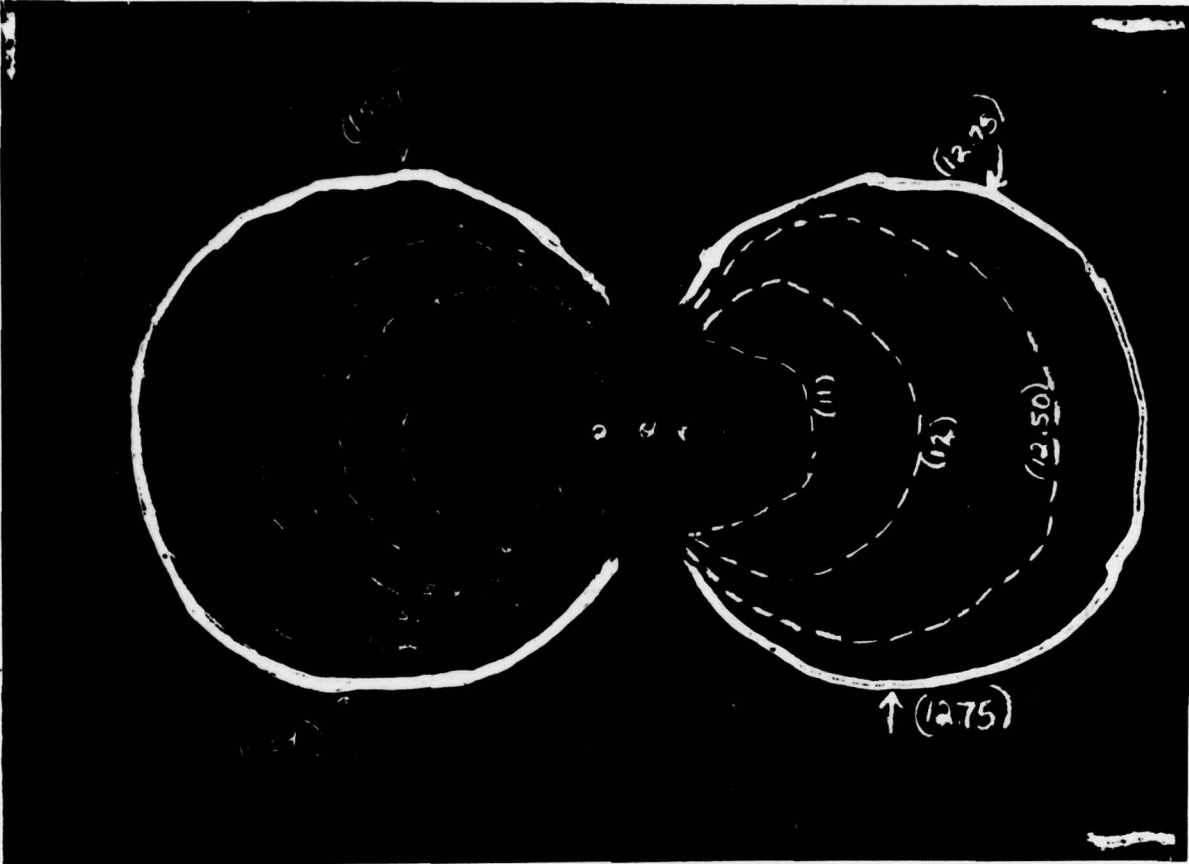
Figure 33. Electric Dipole Case
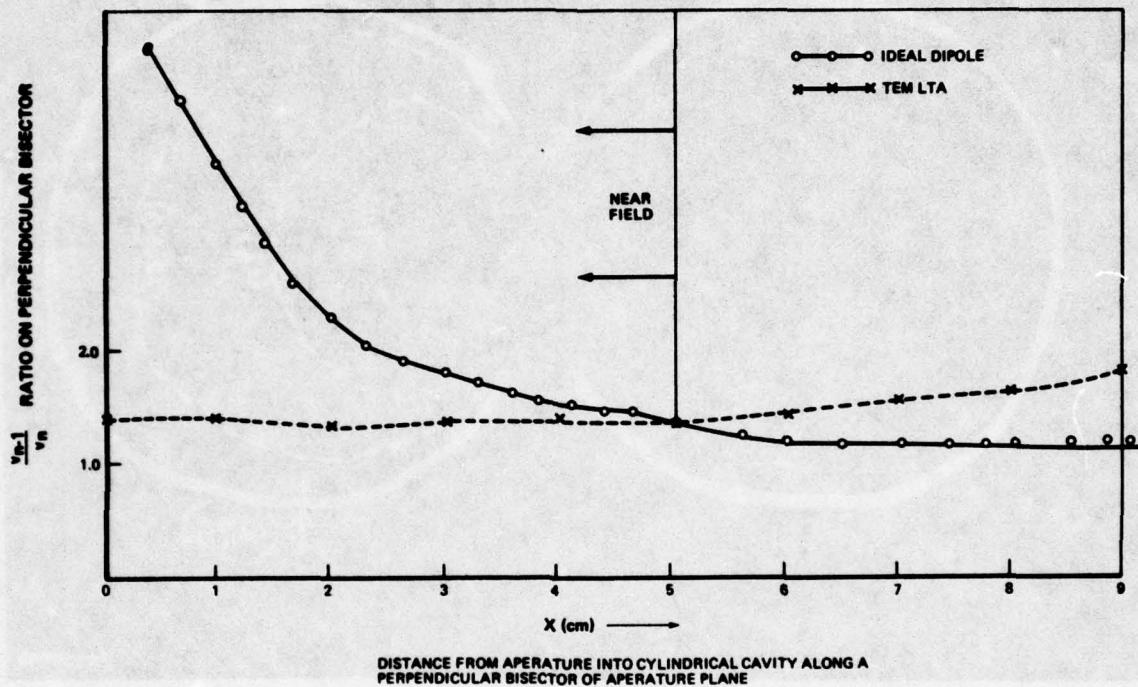
Figure 34. Comparison of $\dfrac{v_{n-1}}{v_n}$ Ratio from Resistance Paper (RP) and Ideal Dipole

42

TABLE I.   COMPARATIVE STUDY OF FIELD BEHAVIOR ALONG
PERPENDICULAR BISECTOR OF APERTURE

X (cm.) P. Bisector	Far Field Dipole Resistance to TEM	TEM (Resistance Paper)	Exponential Reference to TEM of X=0	Yoke-Coil Near-Field Results	Yoke-Coil Exponential Approximated
0	--	0.668	0.668	1.20	1.20
1	--	0.481	0.481	0.80	0.80
2	--	0.350	0.346	0.50	0.53
3	--	0.266	0.249	0.33	0.35
4	--	0.191	0.180	0.25	0.23
5	0.143	0.143	0.129	0.17	0.16
6	0.104	0.104	0.093	--	--
7	0.076	0.076	0.067	--	--
8	0.058	0.054	0.048	--	--
9	0.046	0.035	0.0348	--	--
10	0.037	0.021	0.0250	--	--
11	0.031	0.014	0.018	--	--

Also included in the table are the TEM-RP measurements along with a near-field exponential approximation and a far-field ideal dipole listing. *It is interesting to note that the TEM RP models follow the dipole law in the unshielded far-field region, and also that the exponential variation is a surprisingly good approximation even in the shielded far-field.*

The above observations are of great interest. Analytically, the exponential character should be implicit in the variation of the following integral with X (circular aperture):

$$V(X) = K \int_0^{a-\delta} \frac{\tau^2 \, d\tau}{(\sqrt{a^2 + \tau^2})(\sqrt{\tau^2 + X^2})} \qquad (70)$$

(Magnetic Potential)

Additional far-field yoke-coil measurements are of interest and are currently in progress.

3.3.2.3   Some Preliminary Applications of the TEM RP Model

Some calculations were made which illustrated the value of the resistance paper approach. Referring to Figure 31, the property that the magnitudes of the $\vec{E}$ and $\vec{H}$ fields maintain a constant ratio in the TEM mode provides a method of estimating $|\vec{H}|$ anywhere in the cavity given only the skin current density near the aperture. For example, with a 100 amp/m (typical for LST) near the aperture, we can form the following proportion:

$$\frac{|\vec{H}| \text{ aperture}}{|\vec{H}| \text{ internal}} = \frac{|\vec{E}| \text{ aperture}}{|\vec{E}| \text{ internal}} = \frac{|\nabla V| \text{ aperture}}{|\nabla V| \text{ internal}} \qquad (71)$$

Taking an internal point near the shield at X = 12 cm, the observed potential gradient from the RP solution of Figure 30 is approximately 0.05 V/cm, while the observed gradient at the aperture edge is higher at 1 V/cm. Applying equation (71) the $|H|_{\text{internal}}$ can be estimated as:

$$|H|_{\text{internal}} \approx \left(\frac{0.05}{1}\right) \times 100 \text{amp/m} \approx 5 \text{amp/m} \qquad (72)$$

which can be used to predict the induced voltage levels in the aircraft cabling. As a very crude check on the above result, the H_{internal} was estimated using Van Bladel's (Ref. 11) dipole expression. For a long slot aperture, we can write:

44

$$H_{internal} \approx \frac{\rho_m \cos \theta}{4\pi \; R^3} \approx \frac{2A \; H_o \; (0.476)}{4\pi \; R^3} \qquad (73)$$

The F-111 fuselage has a diameter roughly equal to 6 feet which results in a RP equivalent aperture dimension of 0.77m which, for a unit axial length, yields the following value for the internal magnetic field:

$$H_{internal} \approx \frac{2 \times 0.77 \times 100 \times 0.476}{4\pi \; (1.53)^3} \approx 3.27 \; amp/m \qquad (74)$$

This value is in reasonable agreement with the 5 amp/m previously calculated, considering the crudeness of the approach. At the very least, however, the above analysis does tend to support the usefulness of the TEM assumption.

The TEM model can also be used to investigate the field distortion effects caused by panels and struts contained within the fuselage. Because the situation is hopelessly intractable analytically, potential solutions like the resistance paper method may well be the only approach possible. As an example, a fuselage-grounded navigation receiver chassis is simulated in Figure 35. The high gradients around the sharp corner of the chassis suggest that aircraft cabling should perhaps avoid these locations. Of course, these conclusions are only tentative and must be verified by "yoke-coil" experiments.

3.3.2.4   Remarks on Shielding

For the time-varying case, $H_{NORM} = 0$ at a conductive surface. Physically, the skin currents on the inside surface of the fuselage are induced in such a way as to require $H_{NORM} = 0$. However, the skin currents may develop significant H_{TAN} in the vicinity of the fuselage. It would also be expected that the shielding effects should attenuate as $1/R^2$ from Biot-Savart law considerations alone.

3.3.2.4.1   Conjugate Harmonic Method of Solution

Two-dimensional potential problems can be solved directly if a one-to-one analytic function of a complex variable can be found that will map one boundary surface into another boundary surface with a known potential solution. In our case, the two sets of boundary surfaces are as shown in Figure 36.
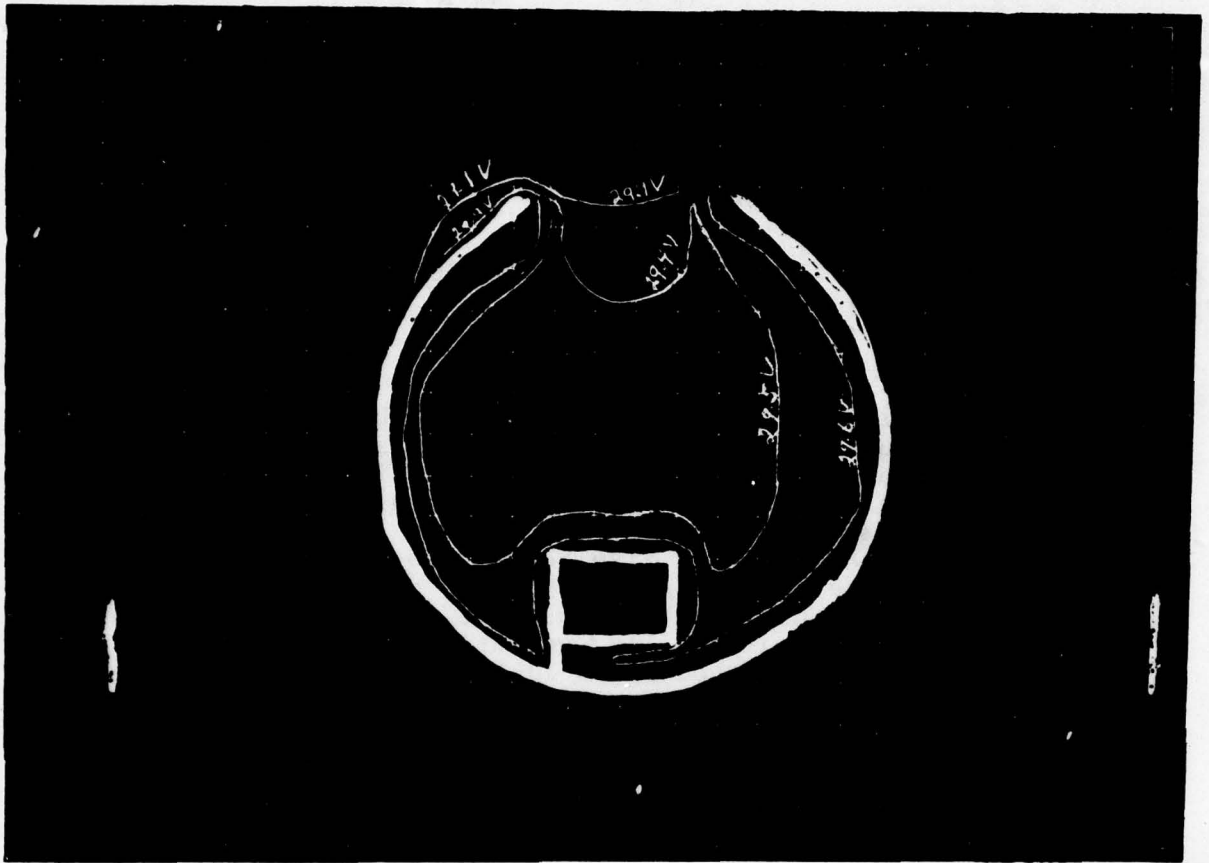
Figure 35. Fuselage-Grounded Navigation Receiver
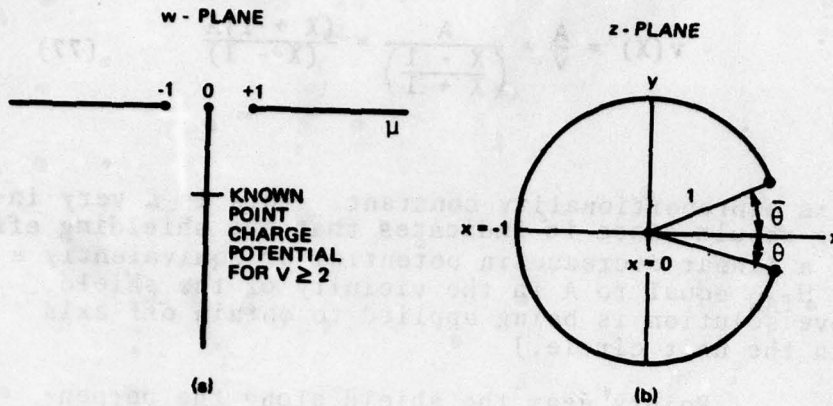Chassis Simulation

Figure 36.   Conformal Map of Fuselage
Boundary Surfaces

Fortunately, the preceding map is a special form of the bi-
linear transformation known as the "Cayley" transformation
and can be given directly as:

$$w = j \left(\frac{Z - 1}{Z + 1} \right) \cot \overline{\theta}/2 \qquad (75)$$

The transformation of (75) maps the interior of the unit
circle into the lower-half of the w-plane. *It is tempting
to treat the w-plane boundary problem as a "small aperture" problem
but this would be incorrect.* The real solution is a continuous,
differentiable electrostatic potential function, $v(\mu,v)$,
that is generated by a charge density distributed around the
aperture.   For the far-field region of interest, the charge
density would appear to be concentrated in the center of the
aperture to yield a potential function at large distance
equal to:

$$v(\mu, v) = \frac{K}{|w|} = \frac{K}{\sqrt{\mu^2 + v^2}} \qquad (76)$$

which when reflected back onto the negative real axis of the
Z-plane becomes:

47

$$v(X) = \frac{A}{v} = \frac{A}{\left(\dfrac{X-1}{X+1}\right)} = \frac{(X+1)A}{(X-1)} \qquad (77)$$

where A is a proportionality constant. This is a very interesting result since it indicates that the shielding effect produces a linear decrease in potential or equivalently a constant H_{TAN} equal to A in the vicinity of the shield. (The above solution is being applied to obtain off-axis points in the unit circle.)

Points near the shield along the perpendicular bisector have been measured on the resistance paper LST model and also on the ideal dipole in the presence of a conductive shield. These measurements, along with the ideal dipole and conjugate harmonic solution, are tabulated in Table II. Excellent agreement is observed which both supports the TEM model and also implies that $\left(\dfrac{X+1}{X-1}\right)$ (normalized) is the true description of the shielding effect, at least along the perpendicular bisector. These results are offered as tentative conclusions and must await experimental confirmation.

TABLE II. VARIOUS PREDICTIONS OF THE SHIELDING EFFECT

X (cm)	Dipole Alone	Dipole with Shield	TEM R.P. Method	$\left(\dfrac{Z+1}{Z-1}\right)$
5	1.0	1.0	1.0	1.0
6	0.707	0.69	0.72	0.74
7	0.52	0.51	0.53	0.53
8	0.36	0.39	0.38	0.36
9	0.20	0.30	0.25	0.23
10	0.10	0.25	0.15	0.13
11	0.005	0.008	0.098	0.039

3.4 An Aperture Coupling Prediction of the Level of Induced Voltage on Aircraft Cabling

3.4.1 General Discussion

This section presents an attempt to predict the induced voltage levels in an aircraft cable from small aperture dipole expressions. Many assumptions are made in the analysis but the assumptions are quite reasonable and the predicted results themselves are similar to actual measured values.

3.4.2 Detailed Discussion

The discussion in the preceding section strongly implied that the shielding effect is not all that significant, at least for offset distances from the shield smaller than 1/3 of the radius of curvature of the shield itself. Accordingly, the H_{INT} should be well represented by the dipole expression of Van Bladel (Ref. 11). Specifically, the induced voltage in a cable can be expressed as:

$$v \approx \mu_o \frac{H_o}{\Delta t} Ak \approx \frac{d\phi}{dt} \tag{78}$$

where for our case:

$H_o = 100$ amps/m (at aperture periphery)

$\Delta t = 0.7$ μsec.

Ak is to be determined

The results on transmission line pulse response suggest that the observed peak-to-peak voltage magnitude in the yaw computer and yaw damper servo circuits is actually the peak-to-peak level of the induced voltage level itself. For the Figure 6 circuit, V can be considered as 50 mV which then leads to an estimate of Ak as follows:

$$Ak \approx \frac{v \, \Delta t}{\mu \, H_o} \approx 2.78 \times 10^{-4} \tag{79}$$

For typical #22 gauge twin lead, $A \approx \ell d$ where $d = 0.3$ cm was measured and ℓ equals the length of the cable subjected to the flux coupling to give:

49

$$k \approx \frac{0.00927}{\ell} \qquad (80)$$

The length ℓ can be estimated provided k is known. The constant k can itself be estimated from the Van Bladel expression in Ref. 11 as:

$$k \approx \frac{\rho_m \, A \, H_o}{4 \, R^3} \qquad (81)$$

or for H_o = 100 amp/m, R = 1.23 m, and an A of 1.23 m^2 which represents the aircraft cockpit aperture:

$$k = 0.1013 \Big|_{R = 1.23 \, m} \qquad (82)$$

The calculated value of k suggests an ℓ equal to:

$$\ell = \frac{0.009}{0.10} = 0.09m = \underline{9 \; cm} \qquad (83)$$

which is a reasonable value. The exact numerical value of the length is of no great significance. It is presented merely for illustrative value only. *The interesting observation is that the length is not some ridiculous value like 5 km or 5 microns.*

4. PULSE RESPONSE OF AIRCRAFT CABLING

The third linear transfer function of the overall LTA system represents the pulse response of the A/C cabling to the aperture flux induced excitation voltage. In this section, the transient response is analyzed in the time domain through the impulse response and in the frequency domain through the voltage transfer function. Another subsection includes a detailed series of actual pulse and CW tests performed on an F-111. The results strongly support the analytical modeling. The final subsection predicts, from the Van Bladel expressions, the relative magnitudes of the inductive and capacitive voltage excitation.

4.1 Time Domain Model; Impulse Response and Convolution

4.1.1 General Discussion

This section deals with a time representation of A/C cable transient response. The experimental work was entirely performed using RG-58 cabling. The new approach is well suited to experimental testing and represents a significant new tool in the analysis of the LTA problem.

4.1.2 Detailed Discussion

4.1.2.1 Discussion of New Method

The pulse response of transmission lines is of central importance to the present study since the transient LST waveforms of interest are actually the responses of aircraft cabling (transmission lines) to induced (inductive or capacitive) voltage pulses. The transient (lossless) situation will be completely defined by the characteristic impedance (Z_0) of the transmission line, its length and terminating impedances, and the position and waveform of the excitation pulse. For the LST application, the transmission lines are excited by a high impedance voltage source ($>>Z_0$) and are usually terminated at the two ends by either an open circuit ($>>Z_0$) or a short circuit ($<<Z_0$). Ideally, a complete definition of the transmission line model permits prediction of the observed waveform at any point of the circuit given a known excitation pulse or, conversely, a determination of the excitation waveform given the observed induced transient waveform. As knowledge is gained, it is expected that observed transient waveforms will suggest the dominant type of coupling (inductive or capacitive), the magnitude of that coupling, and also the position of application of the excitation.

The transmission line model to be considered is illustrated in Figure 37 where Z_1, Z_2 are the terminating impedances and:
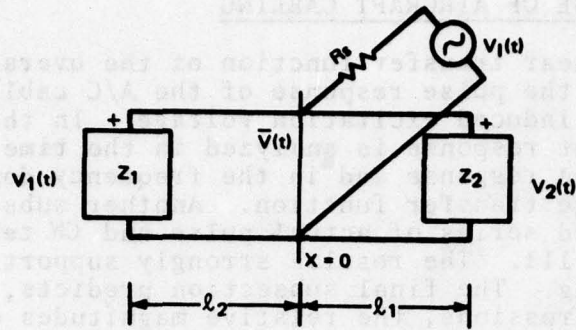
51

Figure 37. Transmission Line Model

where R_s is the source impedance. For this application, Z_1 and Z_2 usually assume the values of 0 or ∞ while R_s is $>> Z_0$ (characteristic impedance) to approximate the magnetic or electric induction effect. Assuming either short circuit or open circuit termination, the impedance at $x = 0$, $Z(\omega)$, will be a parallel combination of impedances having the form $jZ_0 \tan (\omega \ell/V_p)$ or $jZ_0 \cot (\omega \ell/V_p)$ where V_p is the propagation velocity of the transmission line. The complete transient solution, in the frequency domain, for $\overline{V}(\omega)$ will then equal:

$$\overline{V}(\omega) = \frac{V_I(\omega) \, Z_{in}(\omega)}{R_s + Z_{in}(\omega)} \tag{84}$$

where $V_I(\omega)$ is the Fourier transform of the induced voltage waveform. With $\overline{v}(t)$ defined from Eq. 84, $v_1(t)$, $v_2(t)$ can be easily determined by operating on $\overline{v}(t)$ with the appropriate propagation delay. That is, $v_1(t) = \overline{v}(t-\ell_1/V_p)$ and $v_2(t) = \overline{v}(t-\ell_2/V_p)$ in the lossless case. Unfortunately, the representation of Eq. 84 is not physically intuitive and requires taking the inverse transform of a complicated function of ω. A more useful representation is through the convolution integral where any $v(t)$ can be expressed in terms of $v_I(\tau)$ as:

$$v(t) = \int_{0+}^{t} h(t-\tau) \, v_I(\tau) \, dt \tag{85}$$

52

where h(t) is the response measured at the point of v(t) to an impulse applied at the point of $v_I(t)$. One great advantage of the convolution integral is that h(t), for the low-loss case, is a sequence of delta functions separated by integer multiples of the propagation time, e.g.:

$$h(t) \approx \sum_{n=0}^{\infty} a_n \, \delta(t - T_n) \qquad (86)$$

where $a_n = (k)^n$ is the attenuation (k<1) due to the non-zero loss factor. Because h(t) is a linear combination of time-displaced delta functions, the convolution of Eq. 85 becomes straightforward as a result of the sampling property of $\delta(t)$.

That is: $\int_{-\infty}^{\infty} \delta(t-A) \, X(t) \, d\tau = X(t=A)$ which reduces Equations 85 and 86 to:

$$v_1(t) \ \underline{or} \ v_2(t) = \sum_{n=0}^{\infty} a_n \, v_I(t - T_n) \qquad (87)$$

An even more desirable feature of the convolutional approach is the ease with which the impulse response, h(t), can be predicted analytically and measured experimentally for the open and short-circuit termination case. Because short-circuit ($|Z| << Z_0$) and open-circuit ($|Z| >> Z_0$) terminations are commonly found in aircraft cabling, the impulse function approach can be of great importance in the overall LTA program. Very little direct mention is made of this approach in the published literature since the two-termination, infinite source impedance case is not all that common in most applications. In the following subsections, however, many examples will be given illustrating the great value of the technique in analyzing LTA related problems.

4.1.2.2 Experimental Procedure

In order to simulate the aircraft cabling situation, various lengths of RG-58 ($Z_0 = 50\Omega$) cabling were prepared (e.g. 3',6',16',50'). Although the F-111 has unshielded cabling (#22 gauge), it was considered too difficult to work with unshielded cabling because of excessive 60 Hz interference. Fortunately, shielded cable yields essentially the same results given the assumption that cable cross-talk can be neglected.

53

In the actual lab set-up, a source resistance, R_s, of 10K was used which appeared as an infinite resistance to the 50 ohm cable. Higher source resistances ($\approx$2Meg) were tried but the excitation voltage pulse magnitude on the cable was attenuated to such an extent that spurious inductance and capacitance effects were observed. The actual set-up used is illustrated in Figure 38. The excitation pulse was 13V in magnitude and 40 nanoseconds in width which well approximates the Dirac delta function since its width is significantly less than the propagation times of the cabling.
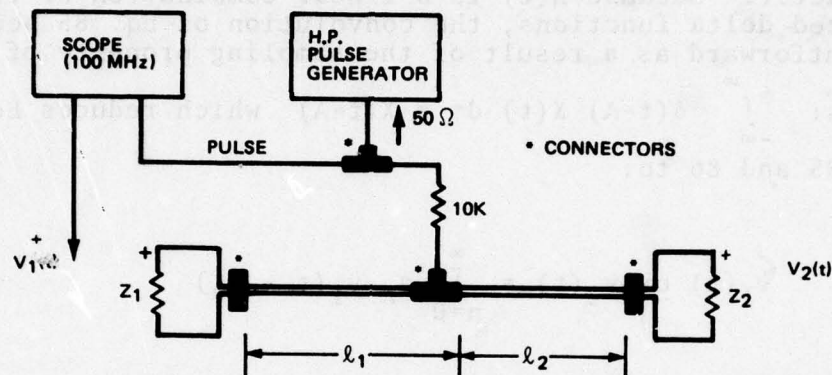
Figure 38.   Experimental Set-Up to Simulate
Aircraft Cabling

As an example of the approach and also as a means of introducing the labeling legend of the figures to follow, the impulse response, h(t), of Figure 39 is presented. The top trace is the 13V (5V/div) excitation pulse and the bottom trace is the response of a 50 foot open-circuited cable measured at the point of application of the excitation pulse. The magnitude of the response waveform is measured on a 50mV/div scale. As expected, the excitation pulse is reflected without inversion and is separated by the round-trip propagation time of 150 nanoseconds (n.s.) from adjacent pulses. The 150 n.s. time interval is expected from the formula:

$$t_p \approx \frac{2\ell}{V_p} = \frac{2\ell\sqrt{\epsilon_R}}{c} \tag{88}$$

where ℓ = 50 ft ~ 15.24 meters

$c = 3 \times 10^8$ m/s

and ε_R is the relative dielectric constant of the plastic spacer in the cable with a known value of ε_R = 2.23, giving a t_p of $\approx$ 153 n.s. *which agrees almost exactly with the observed value.*

The first reflected pulse is observed to be larger than the initial excitation pulse. This somewhat unexpected result can be simply explained by observing that the first reflected pulse is actually the algebraic sum of the pulse reflected from the 50 foot line and the nearly instantaneous re-reflection of the reflected pulse from the open-circuited (ℓ_1=0) end of a "T" connector. Each successive reflection is at a lower magnitude due to the finite resistance of the line (k=0.82). It also possesses a progressively wider pulse width because of the frequency-dependent dispersion effect.

The legends in the many figures to follow will be formated as follows:

$(Z_1-10K\Omega-Z_2)$ corresponds to the left-to-right impedances of Figure 38

(ℓ_1,ℓ_2) corresponds to the lengths of the two cables

$(X - -)$ refers to an observation at the end of ℓ_1 (i.e., at Z_1).

The above notations are always positioned to the left of the figure while the voltage and time scales are always positioned to the right. The legends are illustrated in Figure 39.

$(\infty-10K\Omega-\infty)$ 5V/div

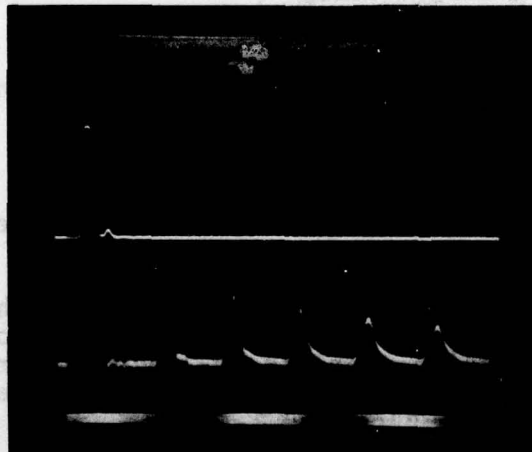$(0',50')$ 50mV/div

$(-X-)$ 100n.s./div

Figure 39. Impulse Response from Experimental Set-Up

The impulse response shown in Figure 39 can be compactly written as:

$$h(t) \approx K \left\{ \delta(t) + (1.4) \sum_{n=1}^{\infty} (0.82)^{n-1} \delta[t-n(150ns)] \right\} \quad (89)$$

It should be observed that the initial pulse magnitude $K \approx 60mV$ is to be expected since the cable appears as 50Ω (infinite line) before the initial reflection to give as a predicted value:

$$K \approx V \left(\frac{Z_o}{R_s + Z_o} \right) \approx 13 \left(\frac{50}{10,000 + 50} \right) \approx 65mV \quad (90)$$

which is good agreement.

Using the $h(t)$ of Eq. 89, the output for an input, $v_I(t)$, is:

$$v_1(t) \approx K \left\{ v_I(t) + (1.4) \sum_{n=1}^{\infty} (0.82)^{n-1} v_I[t-n(150ns)] \right\} \quad (91)$$

where $v_I(t)$ is the waveform of the induced voltage pulse which should have a waveform corresponding to the time derivative of the unipolar current pulse; i.e., a waveform similar to Figure 40.
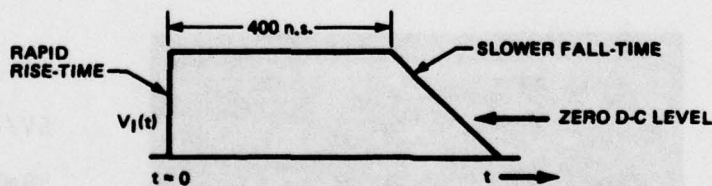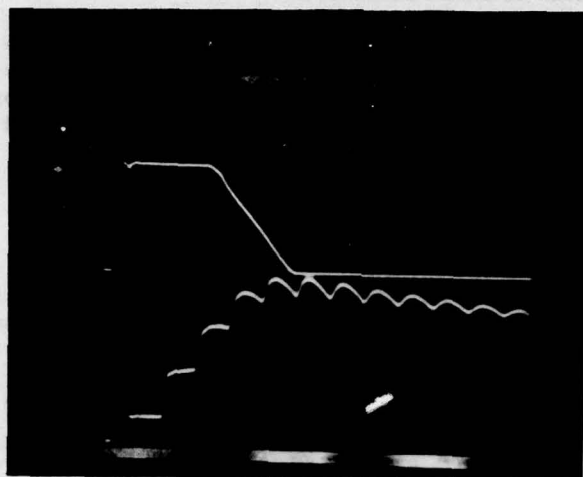

Figure 40.   Predicted Induced Voltage Waveform

Accordingly, since the $h(t)$ is always positive, the $v_I(t)$ will represent "stair-case" ramp or build-up in voltage as suggested by Eq. 91 which expresses $v_I(t)$ of Figure 40. This prediction is beautifully confirmed by Figure 41.

56

(∞—10KΩ—∞)   5V/div

(0',50')   100mV/div

(—X—)   200n.s./div

Figure 41. Measured Induced Voltage Waveforms

Referring to the Z_{in} of an open-circuited line, Z_{in} = $jZ_0 \cot\left(\frac{2\pi\ell}{\lambda}\right)$, the waveshape of Figure 41 can be explained as the charging of the low-frequency capacitance: $\left(Z_{in} \approx \frac{-j\,V_p}{\omega\,\ell} => C_{low}\,\underline{\omega} \approx \frac{\ell}{V_p}\right)$ through R_s = 10K for a period of 400 n.s. followed by the decay through the same R_s. The square-wave reflection component is superimposed on the low-frequency waveform and is composed of harmonics as suggested by the equivalent circuit of Figure 42:
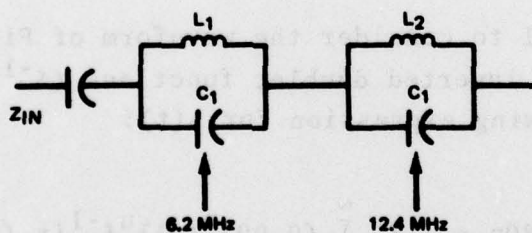

Figure 42. Equivalent Circuit of Cabling Set-Up

Many more examples of the above approach are presented in subsequent sections.

57

4.1.2.3 Applications of the Method

In order to illustrate how the new method is applied five different conditions, or examples, have been selected. Each of these conditions is presented with illustrations depicting the impulse, cable response, voltage pulse and current pulse observed at selected points in the circuit. Each condition is discussed to highlight its significance.

Condition I

Figures 43 and 44 present the same situation as in Figures 40 and 41 with the _important_ exception that now the end of the 50' line is short-circuited ($Z_2=0$) instead of open-circuited. The presence of the resulting inversion has important LTA implications since $h(t)$ now has a zero D.C. level which means that any output must also have zero D.C. level. That is, it does not grow linearly to the large magnitudes of Figure 41, but instead oscillates at 6.2 MHz with a peak-value of 65mV as shown.

Condition II

There are many variations of the first condition possible. To illustrate, ℓ_1 is chosen to be 3 inches and Z_1 is set to 0 (short-circuit) while ℓ_2, Z_2 remain at 50' and ∞ respectively. With the measurement at Z_2, an interesting effect is observed. As before, the excitation pulse begins 80 n.s. after $t = 0^+$ but the pulse is never allowed to build to its full value since an inverted pulse (reflected from the shorted end) begins 10 n.s. after $t = 80$ n.s. and produces the interesting waveform of Figure 45. As expected, the peak value of the waveform has been reduced from 60mV to 20mV. It is also observed that successive reflected pulses are inverted due to the presence of the shorted-end. As before, there is a progressive widening and decrease in magnitude at each successive reflection.
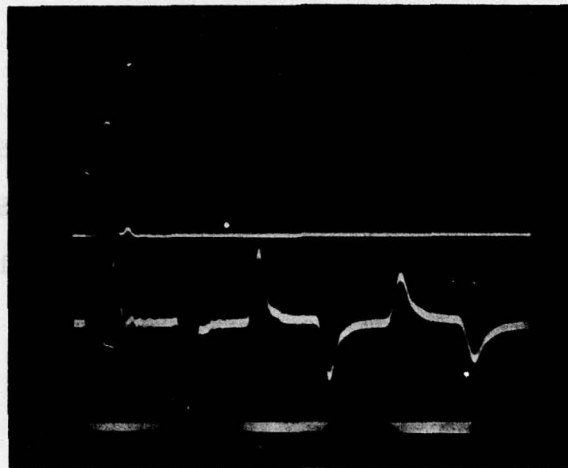
It is useful to consider the waveform of Figure 45 as a time sequence of inverted doublet functions ($\delta^{-1}(t) = \frac{d}{dt}\delta(t)$) giving the following expression for $h(t)$:

$$h(t) \approx K\left\{\delta^{-1}(t-80\text{n.s.}) + \sum_{n=1}^{\infty}(0.90)^n(-1)^n\delta^{-1}[t-(80+n150)]\right\} \quad (92)$$

which leads to:

$$v_2(t) \approx K\left\{\frac{d}{dt}v_I(t-80) + \sum_{n=1}^{\infty}(0.90)^n(-1)^n\frac{d}{dt}v_I[t-(80+n150)]\right\} \quad (93)$$
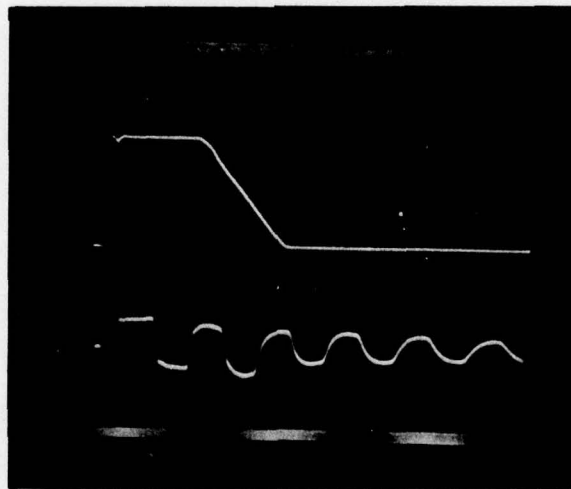
58

(∞—10KΩ—

(0',50')

(—X--)

5V/div

50mV/div

100n.s./div

Figure 43.   Impulse Response from Short Circuit Condition

(∞--10KΩ—0)
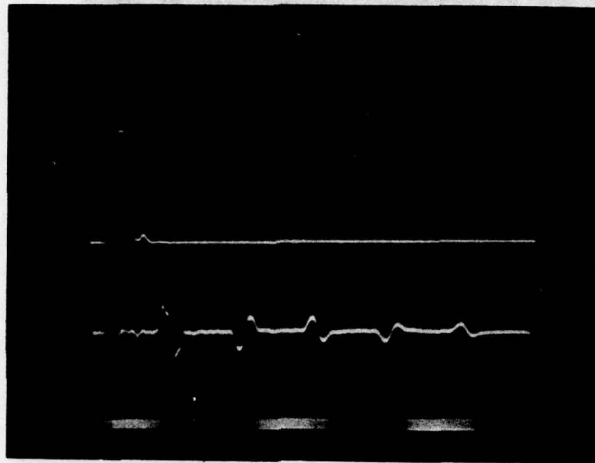
(0',50')

(—X—)

5V/div

50mV/div

200n.s./div

Figure 44.   Voltage Across Z_1 for Short Circuit Condition

(0—10KΩ—∞)   5V/div

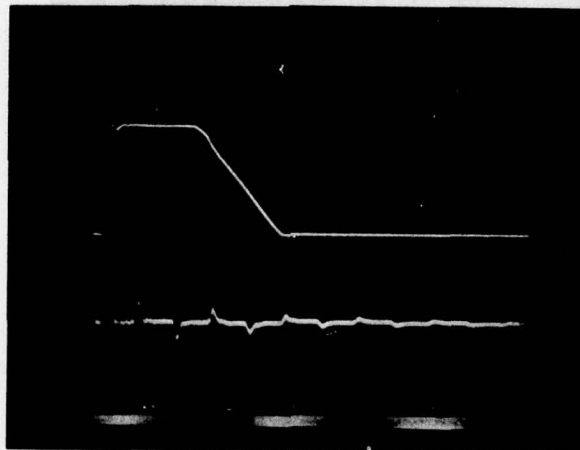(3",50')   50mV/div

(— — X)   100n.s./div

Figure 45.   Impulse for Condition II

(0—10KΩ—∞)   5V/div

(3",50')   50mV/div

(-- — X)   200 n.s./div

Figure 46.   Response for Condition II

Expressions 92 and 93 are completely verified by Figures 45 and 46.

It may be suggested that the actual waveform for h(t) (Figure 45) is strongly influenced by the finite pulse width of the simulated delta function. Although this is undoubtedly true, the situation is actually desirable since the finite pulse width ($\approx$30 n.s.) provides nearly the exact band limiting ($\approx$30 MHz) as provided by the fiber-optic instrumentation system.
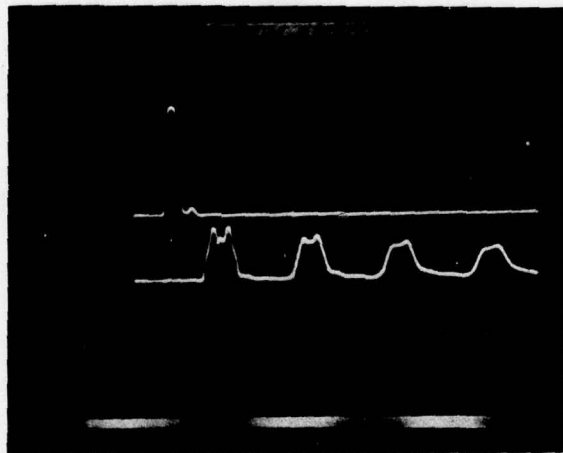
Condition III

In order to provide additional background and also to introduce (ℓ_1, ℓ_2) pairs that approximate the postulated yaw-damper circuit situation, Figures 47, 48 and 49 are presented. With both ends open (not yaw-damper situation) the h(t) measured at the 50' end consists of time displaced train of pulses that are the sum of a 50' delay and a 62' (6' + 56') delay. Figures 48 and 49 give the expected response for the all open-circuit case.

$(\infty-10K\Omega-\infty)$ 5V/div

$(6',50')$ 50mV/div
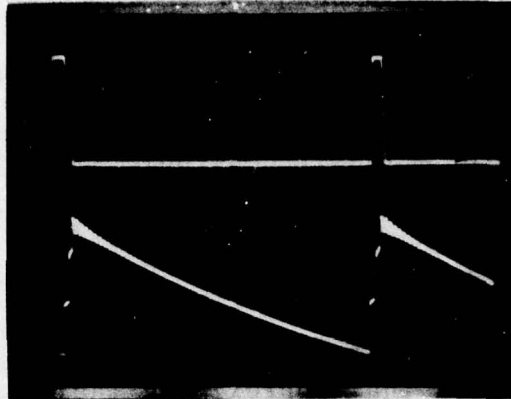
$(- - X)$ 100n.s./div

Figure 47.   Impulse for Condition III

(∞–-10KΩ–∞)	5V/div
(6',50')	100mV/div
(– – X)	500n.s./div

Figure 48.   Response for Condition III
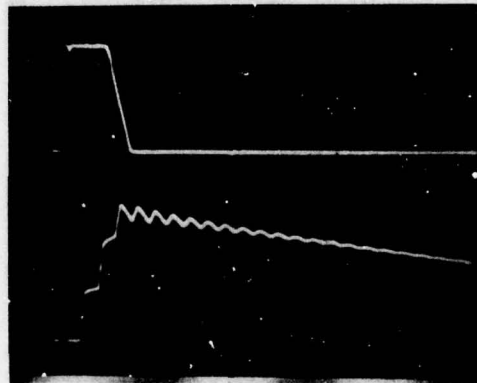
(∞—10KΩ—∞)	5V/div
(6',50')	100mV/div
(– – X)	2μsec/div

Figure 49.   Response for Condition III (Expanded Scale)

62

YAW COMPUTER

APERTURE FLUX
APPLIED 6' FROM
SHORTED-END AND
5' FROM OPENED
END

SERVO OUTPUT AMPLIFIER

BREAK OUT
CABLE

CIRCUIT
13 M FROM NO. 4
SHIELD FROM LTA
SURFACE CURRENT

YAW DAMPER
SERVO

D

S1

SHORTING
CAPACITORS

R ≫ Z₀

R ≫ Z₀

CIRCUIT
NEAR
APERTURE

S2

P204   J204

A
20   L

A
16   V
            E

A
18

3   WL ≫ Z₀

2   BRANCH B
          SERVO VALVE

1   WL ≫ Z₀

13M

OPEN CIRCUIT
WL

TEST
RECEPTACLE

H

G

-12V
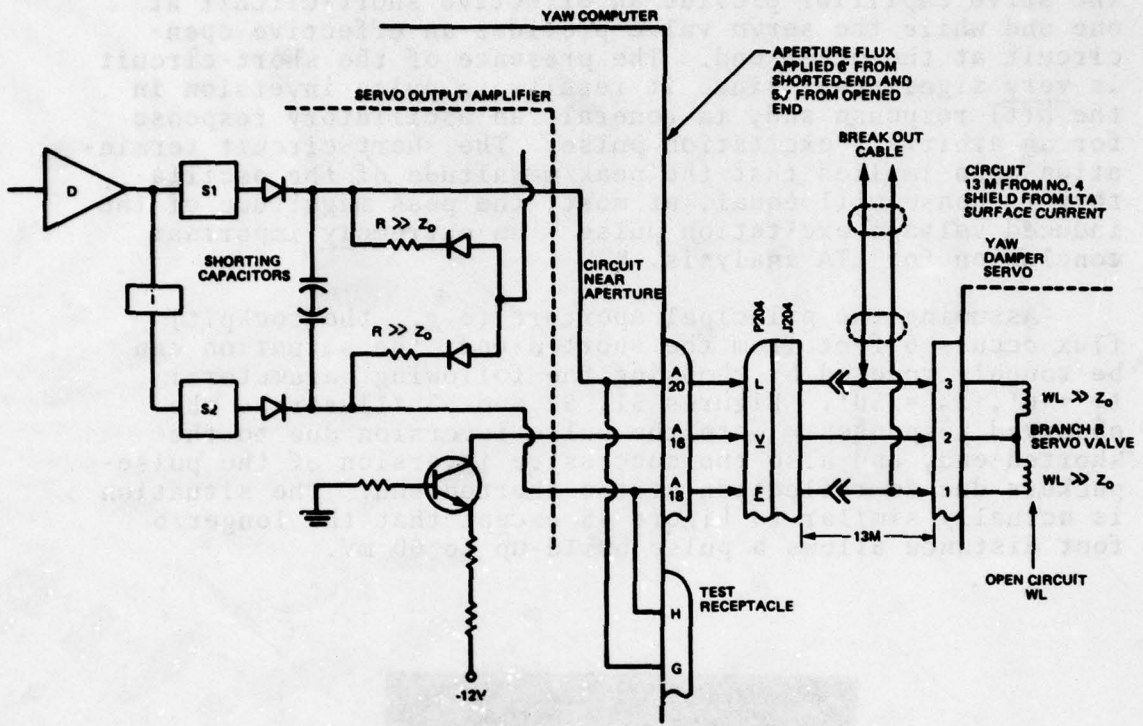
Figure 50. Yaw Circuit Schematic

Condition IV

The F-111 yaw circuit schematic is given in Figure 50. As is discussed in later sections, the by-pass capacitors in the servo amplifier provide an effective short-circuit at one end while the servo valve provides an effective open-circuit at the other end. The presence of the short-circuit is very significant since it results in pulse inversion in the $\overline{h(t)}$ response and, in general, an oscillatory response for an arbitrary excitation pulse. The short-circuit termination also implies that the peak magnitude of the oscillatory response will equal, at most, the peak magnitude of the induced voltage excitation pulse - an extremely important conclusion for LTA analysis.

Assuming the principal aperture (e.g., the cockpit) flux occurs 6 feet from the shorted-end, the situation can be roughly modeled by choosing the following parameters: $\ell_1 = 6'$, $\ell_2 = 50'$. Figures 51, 52 and 53 illustrate the observed responses. Note the pulse inversion due to the shorted-end, and also the successive inversion of the pulse-packets due to reflection at the shorted-end. The situation is actually similar to Figure 45 except that the longer 6 foot distance allows a pulse build-up to 60 mV.
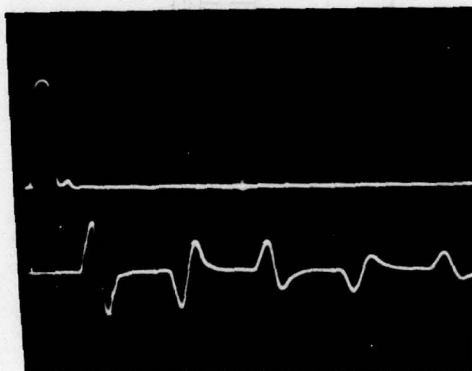
|	
$(0-10K\Omega-\infty)$	5V/div
$(6',50')$	50mV/div
$(- - X)$	100n.s./div

Figure 51. Impulse for Condition IV

Figures 52 and 53 clearly illustrate the damped oscillatory nature of the transient response. This is, of course, similar to the situation actually observed in LTA experiments. Referring to Figure 52, the response within the time interval, $0 \leq t < 2\mu sec.$, is nonsinusoidal due to the presence of higher modes or harmonics. Because of the increased skin resistance at the higher harmonics, the waveform approaches the 6.25 MHz sinusoidal response for $t \geq 2\mu sec.$

64

(0–10KΩ–∞)   5V/div

(6',50')   50mV/div
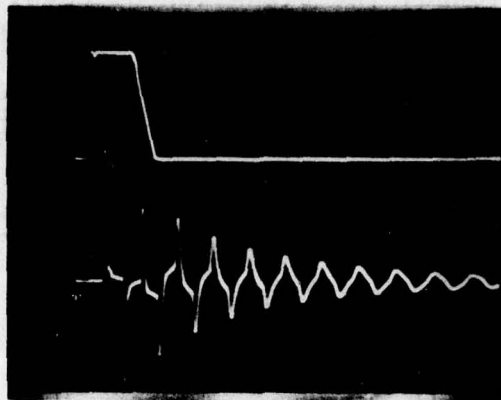
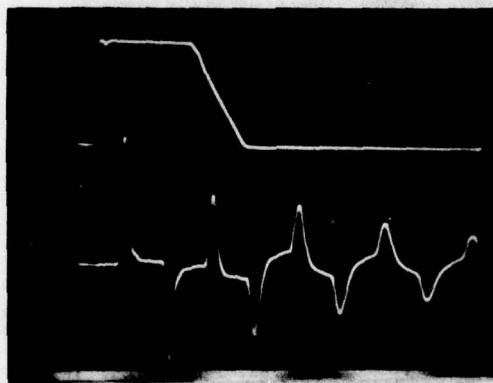(– – X)   500n.s./div

Figure 52.   Response for Condition IV

(0–10KΩ–∞)   5V/div
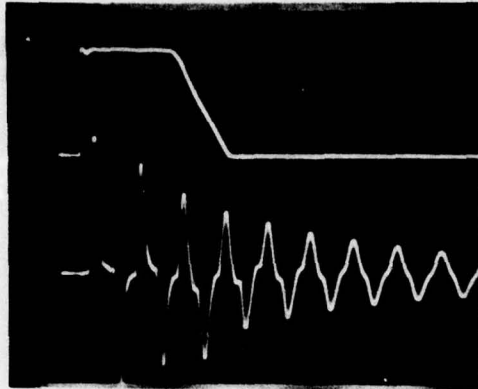
(6',50')   50mV/div

(– – X)   200n.s./div

Figure 53.   Response for Condition IV
             (Expanded Scale)

Condition V

For added background, the situation of Condition IV was repeated except that ℓ_2 was shortened to 16 feet from 50 feet. Because of the shorter ℓ_2, all responses became more symmetrical and approximated the damped sinusoid earlier in the transient interval. *In the case where* $\ell_1 = \ell_2$, *the responses would be perfectly symmetrical - a potentially useful observation!* Figure 56 illustrates the response to the 500 n.s. pulse at two observation points and is added for completeness.

$(0-10K\Omega-\infty)$ 　　　　　　　　　　　　　　5V/div

$(6',16')$ 　　　　　　　　　　　　　　　　　　50mV/div
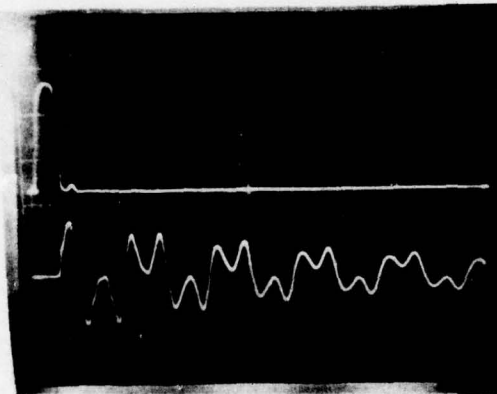
$(- - X)$ 　　　　　　　　　　　　　　　　　　100n.s./div

Figure 54. Impulse for Condition V

66

$(0-10K\Omega-\infty)$ 5V/div

$(6',16')$ 50mV/div

$(- - X)$ 200n.s./div

Figure 55.   Response for Condition V

$(0-10K\Omega-\infty)$ 20mV/div
                                                               $(- X -)$
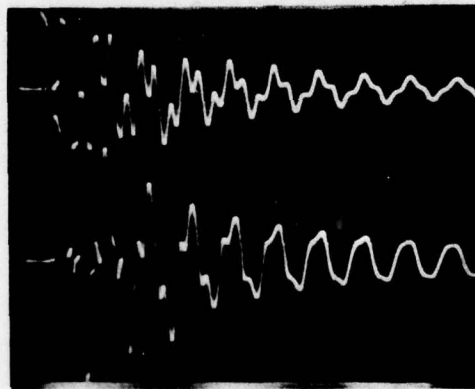
$(6',16')$ 20mV/div
                                                               $(- - X)$

                                                               200n.s./div

Figure 56.   Condition V Response to 500 Nanosecond Pulse

67

4.2 Investigation on How $h(t)$ is Affected by Varying the Terminating Impedances (Z_1 and Z_2)

In general, when the initial impulse, $\delta(t)$, reaches a terminating impedance, $Z(s)$, the equivalent circuit is as shown:
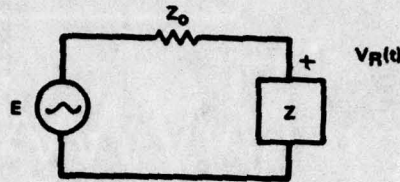
where $V_R(t)$ is the reflected pulse

Figure 57. Equivalent Circuit for Terminating Impedance

Now, $V_R(s) = \dfrac{E\,Z(s)}{Z_0 + Z(s)}$, so that the reflected pulse can be (94) determined in general (except for $Z = 0$ where an admittance model must be used).

For a 6' and 50' cable case the 50 foot end is terminated with a $10\mu h$ inductor. Using the above model, the inductor case can be solved in general as:

$$V_R(s) = \frac{Es}{R_0/L + s} \qquad (95)$$

which implies that:

$$V_R(t) = E\,\frac{d}{dt}\left[e^{-t\,R_0/L}\,\mu(t)\right] \qquad (96)$$

$$= E\,\delta(t) - \frac{E\,R_0}{L}\,e^{-t\,R_0/L}\,\mu(t)$$

68

It is apparent that as L(or ωL) gets larger, h(t) approaches
E δ(t) which corresponds to the open-circuit case (e.g., yaw
damper circuit in Figure 6). As L is reduced in value,
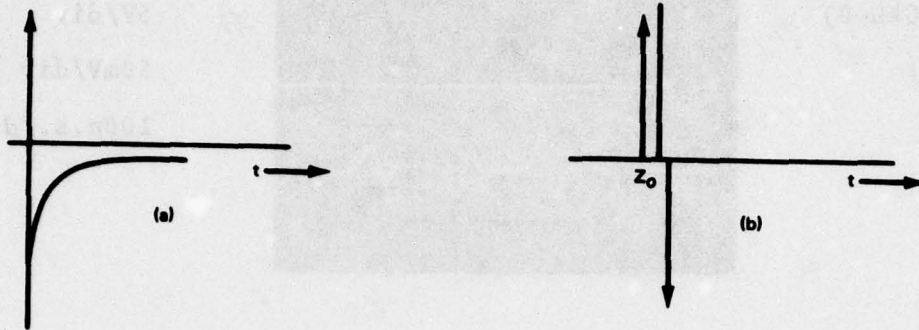the v_R(t) begins to assume the shape of Figure 58(a).

Figure 58. Results of Variations in L

Eventually, the h(t) approaches $\frac{d\ \delta(t)}{dt}$ which has the shape
of Figure 58(b). Figures 60 and 61 illustrate this effect.
Specifically, in Figure 60, the 50' section is terminated in
10μh which essentially open-circuits the termination while
the 50' section in Figure 61 is terminated in 0.1μh which
results in the differentiation effect shown in Figure 58.
The rather "odd" pulse waveform in Figure 61 is the summation
of a differentiated δ(t) at the end of the 50' section added
to an inverted $\frac{d}{dt}$ δ(t) delayed because of the reflection at
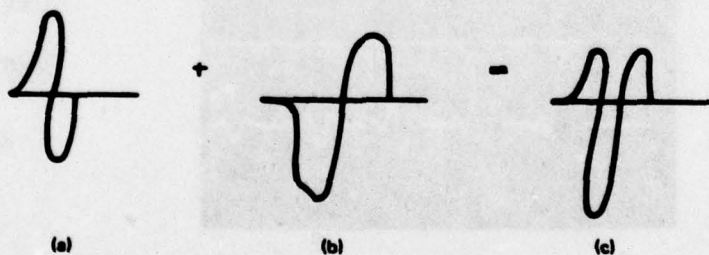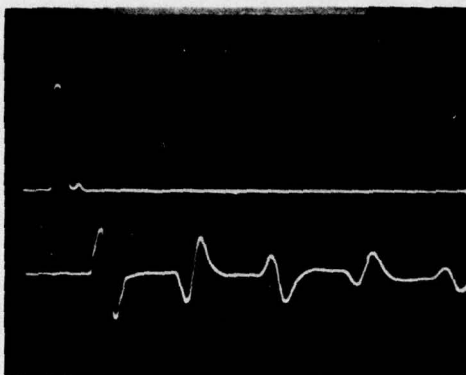the shorted 6 foot section as illustrated in Figure 59.

Figure 59. Addition of Pulses

69

It is apparent that for d/λ gets larger, $M(t)$ approaches
$I(t)$, which corresponds to the open circuit case (e.g., few
damper circuit, in phase ... ...
the $N(t)$ begins to ... ... (a).

(10μh–10KΩ–0)
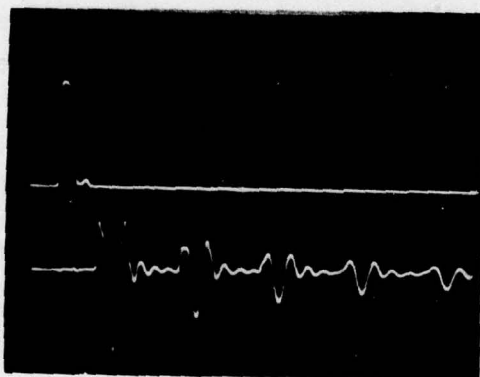
(50',6')

(X – –)

5V/div

50mV/div

100n.s./div

L = 10μh

Figure 60. Impulse for 50-Foot Cable with 10μh Termination

(0.1μh–10KΩ–0)

(50',6')

(X – –)

5V/div

50mV/div

100n.s./div

L = 0.1μh

Figure 61. Impulse for 50-Foot Cable with 0.1μh Termination

An entirely similar analysis was made with regard to shorting the end of the 6 foot section with capacitance. As expected, the situation approaches the shorted case as C gets larger with lower C values producing differentiation. Figures 62 and 63 illustrate waveforms for 1800 pf and 300 pf terminations.

(∞—10KΩ—1800pf)   5V/div

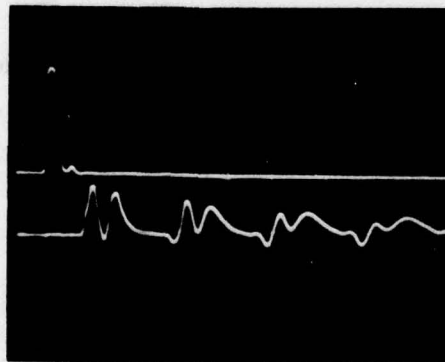(50',6')   50mV/div
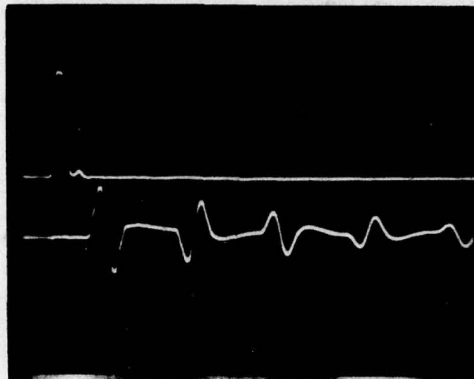
(X − −)   100n.s./div

C = 1800 pf

Figure 62.   Impulse for 6-Foot Cable
with 1800 pf Termination

(∞—10KΩ—300pf)   5V/div

(50',6')   50mV/div

(X ·· −)   100n.s./div

C = 300 pf

Figure 63.   Impulse for 6-Foot Cable
with 300 pf Termination

71

4.3 Frequency Domain Model, Voltage Transfer Function

4.3.1   General Discussion

The following development derives the $G_{A/C}(\omega)$ transfer function and as such constitutes an important step in the linear system analysis of the LTA problem. Included in the derived transfer function is the attenuation and dispersive effect due to the skin resistance term. Also included is a proposed identification technique for $G_{AP}(\omega)$ using the derived $G_{A/C}(\omega)$.

4.3.2   Detailed Discussion

4.3.2.1   Transfer Function Derivation

It is desired to determine the voltage transfer function of two low-loss transmission lines (one end open, the other end shorted) connected in parallel and driven from a high source impedance. Such a configuration closely approximates typical aircraft circuitry as will be justified in later sections.

The following discussion deals exclusively with the configuration of Figure 64.
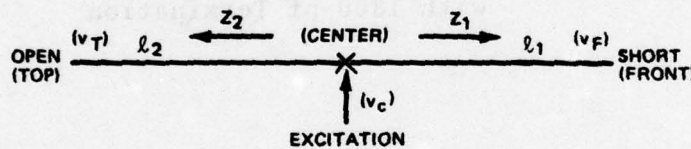

Figure 64.   Low-Loss Circuit Configuration

which is a specific example of the general parallel arrangement of Figure 65.
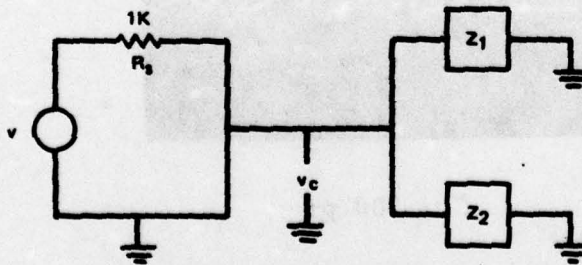

Figure 65.   General Parallel Circuit Arrangement

72

From Figure 65:

$$v_c = \frac{v \; Z_3}{R_s + Z_3} \approx \frac{v}{R_s} \; (Z_1 || Z_2) \; (R_s \gg Z_1, \; Z_2) \qquad (97)$$

where

$$Z_3 = \frac{Z_1 Z_2}{Z_1 + Z_2}$$

In the steady state, standing waves are established for the loss-less under sinusoidal excitation.

Therefore, we have:

$$|v_T| = \frac{|v_c|}{\cos\left[-\dfrac{\omega \; \ell_2}{V_p}\right]}; \quad |v_F| = \frac{|v_c|}{\sin\left[\dfrac{\omega \; \ell_1}{V_p}\right]} \qquad (98)$$

Now from the open and shortened terminations, it follows that:

$$Z_1 = j \; Z_0 \; \tan\left[\frac{\omega \; \ell_1}{V_p}\right]$$

and: $\qquad\qquad\qquad\qquad\qquad\qquad\qquad\qquad\qquad\qquad\qquad (99)$

$$Z_2 = j \; Z_0 \; \cot\left[\frac{\omega \; \ell_2}{V_p}\right]$$

With $\quad v = 1 \underline{|0^0} = 1$, the voltage transfer function becomes:

$$|v_c| = Z_0 \; \frac{\tan\left[\dfrac{\omega \; \ell_1}{V_p}\right] \cot\left[\dfrac{\omega \; \ell_2}{V_p}\right]}{\tan\left[\dfrac{\omega \; \ell_1}{V_p}\right] - \cot\left[\dfrac{\omega \; \ell_2}{V_p}\right]} \qquad (100)$$

where: $\quad Z_0 \approx 100\Omega; \; V_p = 2 \times 10^8 \; m/sec$

$\qquad\qquad \ell_1 + \ell_2 = 17 \; m$

$\qquad\qquad 0 \leq f \leq 15 \; MHz.$

For added realism, it is necessary to include the low but non-negligible loss term in the transfer function. This can be accomplished by expressing the frequency varying skin resistance term, $\alpha(f)$, as the real part of a complex propagation constant. (The justification for this derivation is beyond the scope of this report but is given clearly in Reference 14. The actual open and shorted driving point impedances are given in terms of the hyperbolic tangent and cotangent functions of a complex agreement as indicated in equations (101) and (102).

Shorted Section

$$Z_1 = Z_0 \tanh(\gamma \ell_1) = Z_0 \tanh[(\alpha + j\beta)\ell_1]$$

$$= Z_0 \left\{ \frac{\sinh(\alpha \ell_1) \cos\left[\dfrac{\omega \ell_1}{V_p}\right] + j \cosh(\alpha \ell_1) \sin\left[\dfrac{\omega \ell_1}{V_p}\right]}{\cosh(\alpha \ell_1) \cos\left[-\dfrac{\omega \ell_1}{V_p}\right] + j \sinh(\alpha \ell_1) \sin\left[\dfrac{\omega \ell_1}{V_p}\right]} \right\} \tag{101}$$

FOOTNOTE

$d = R/\alpha Z_0$

$R = 0.123 \sqrt{f \times 10^{-5}}$ ohm/meter   (f in MHz) referenced to 100 MHz

$Z_0 = 100$

so

$\alpha(f) = \dfrac{R}{2Z_0} = 5 \times 10^{-3} \sqrt{f \times 10^{-5}}$

74

Open Section

$$Z_2 = Z_0 \coth (\gamma \ell_2)$$

(102)

$$= Z_0 \frac{\cosh (\alpha \ell_2) \cos \left[\frac{\omega \ell_2}{V_p}\right] + j \sinh (\alpha \ell_2) \sin \left[\frac{\omega \ell_2}{V_p}\right]}{\sinh (\alpha \ell_2) \cos \left[\frac{\omega \ell_2}{V_p}\right] + j \cosh (\alpha \ell_2) \sin \left[\frac{\omega \ell_2}{V_p}\right]}$$

For added background, equations (101) and (102) have been broken into the elemental forms listed below used to program the transfer function on the digital computer.

$$\frac{Z_1}{Z_0} = \frac{A_1 + j A_2}{B_1 + j B_2} ; \qquad A_1 = \sinh (\alpha \ell_1) \cos \left[\frac{\omega \ell_1}{V_p}\right]$$

$$A_2 = \cosh (\alpha \ell_1) \sin \left[\frac{\omega \ell_1}{V_p}\right]$$

$$B_1 = \cosh (\alpha \ell_1) \cos \left[\frac{\omega \ell_1}{V_p}\right]$$

$$B_2 = \sinh (\alpha \ell_1) \sin \left[\frac{\omega \ell_1}{V_p}\right]$$

(103)

$$\frac{Z_2}{Z_0} = \frac{C_1 + j C_2}{D_1 + j D_2} ; \qquad C_1 = \cosh (\alpha \ell_2) \cos \left[\frac{\omega \ell_2}{V_p}\right]$$

$$C_2 = \sinh (\alpha \ell_2) \sin \left[\frac{\omega \ell_2}{V_p}\right]$$

$$D_1 = \sinh (\alpha \ell_2) \cos \left[\frac{\omega \ell_2}{V_p}\right]$$

$$D_2 = \cosh (\alpha \ell_2) \sin \left[\frac{\omega \ell_2}{V_p}\right]$$

75

$$\frac{Z_1}{Z_0} = \frac{\sqrt{A_1^2 + A_2^2}}{\sqrt{B_1^2 + B_2^2}} \quad \bigg/ \tan^{-1}\left(\frac{A_2}{A_1}\right) - \tan^{-1}\left(\frac{B_2}{B_1}\right)$$

$$= M_1 \bigg/ \overline{\theta}_1$$

$$\frac{Z_2}{Z_1} = \sqrt{\frac{C_1^2 + C_2^2}{D_1^2 + D_2^2}} \quad \bigg/ \tan^{-1}\left(\frac{C_2}{C_1}\right) - \tan^{-1}\left(\frac{D_2}{D_1}\right)$$

$$= M_2 \bigg/ \overline{\theta}_2$$

$$\frac{Z_1}{Z_0} = \frac{Z_2}{Z_0} = (M_1 \cos \overline{\theta}_1 + M_2 \cos \overline{\theta}_2) + j(M_1 \sin \overline{\theta}_1 + M_2 \sin \overline{\theta}_2)$$

$$= F_1 + j F_2$$

Therefore, it follows, from (103) that:

$$|V_c| = \frac{Z_0 M_1 M_2}{\sqrt{F_1^2 + F_2^2}} \qquad \text{[Center Observed]}$$

$$|V_T| = \frac{|V_c|}{\cos\left[\dfrac{\omega \ell_2}{V_p}\right]} \qquad \text{[Top Observed]} \qquad (104)$$

$$|V_F| = \frac{|V_c|}{\sin\left[\dfrac{\omega \ell_1}{V_p}\right]} \qquad \text{[Front Observed]}$$

The expressions of (104) have been programmed on a digital computer. A comparison with experimental measurements is given in the next section of this report.

4.3.2.2   A Possible Frequency Domain Test for the Nature of the Aperture Coupling

For inductive coupling:

$$v_L(t) \; \alpha \; \frac{di}{dt} \text{ where } i(t) \text{ is LTA current}$$

so that, in the frequency domain:

$$|V_L(j\omega)| = \frac{(V_{C/L}) \, \omega}{\sqrt{\left(\frac{1}{LC} - \omega^2\right) + (\omega \, R/L)^2}} \qquad (105)$$

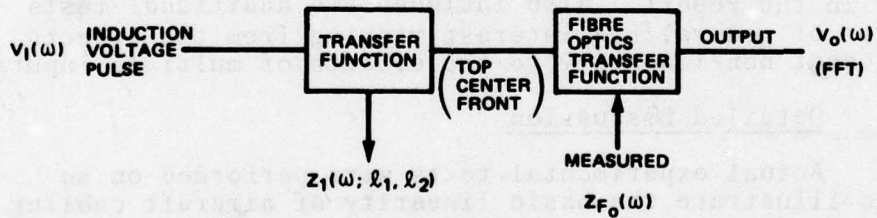while for capacitive coupling:

$$|V_C(j\omega)| = \frac{(V_{C/L}) \, \omega^2}{\sqrt{\left(\frac{1}{LC} - \omega^2\right) + (\omega \, R/L)^2}} \qquad (106)$$

Figure 66.   Diagram for Frequency Domain Test

The identification proceeds by considering the following two hypotheses:

77

a.   Inductive Coupling

$$|V_O(\omega)| = |V_I(\omega)||Z_T(\omega)||Z_{F_O}(\omega)| \qquad (107)$$

We can then step through ℓ_1, ℓ_2 to get optimum least squares fit to $V_O(\omega)$.

b.   Capacitive Coupling

$$|V_O(\omega)| = |V_C(\omega)||Z_T(\omega)||Z_{F_O}(\omega)| \qquad (108)$$

The influence of the different input $|V(\omega)|$ should provide the identification. This procedure constitutes a proposed identification technique that has not been implemented at this time.

4.4   Various Pulse and CW Tests on RG-58 Cabling and on the F-111 Yaw Damper Control Circuit

4.4.1   General Discussion

The test results in this section include confirmation of both the time and frequency domain techniques advanced earlier in the report. Also included are additional tests on topics of general LTA interest ranging from the effects of component non-linearity to the effects of multiple inputs.

4.4.2   Detailed Discussion

Actual experimental tests were performed on an F-111 to illustrate the basic linearity of aircraft cabling and also to demonstrate the power of the new time domain analysis technique. The yaw damper control circuit was chosen because it is long in length, has easily accessible terminations, and is, moreover, a highly critical circuit. During these pulse experiments a pulse generator was employed to generate 30 n.s. wide pulses through a high impedance ($>>$ Z_0 of cable). The 30 n.s. pulse width adequately simulated an impulse since the fiber optics bandwidth itself is around 33 MHz and the propagation times ($\approx$150 n.s.) are sufficiently longer than 30 n.s.

4.4.2.1   Open Circuit Yaw Damper Circuit Results

In order to test the low-loss assumption, both the servo-computer termination (front) and the servo-valve termination (top) were open-circuited. A pulse was applied at the "top" and measured at the "front". The response is shown in Figure 67. It is clear that the pulse structure is maintained for six (6) round-trip propagations. Some attenuation and pulse widening is observed as is expected.
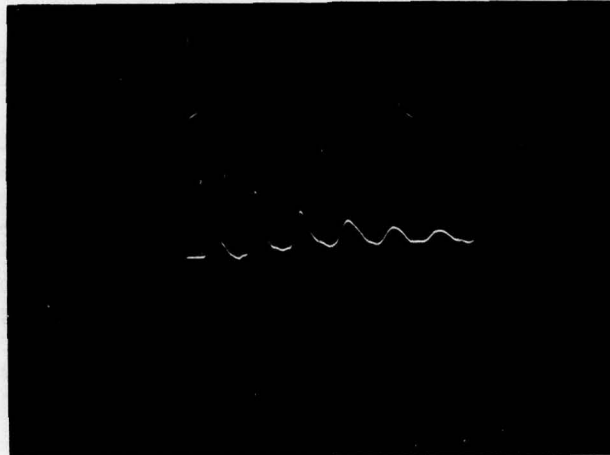
100 n.s./div

Figure 67.   Open Circuit Case; Top Excited,
Front Observed

4.4.2.2   Propagation Effects as Observed When Pulse Exciting at Cable Center

In order to better approximate the lightning excitation, a cable entry point near the cockpit aperture was prepared by removing a panel and "stripping" bare the appropriate pair of wires in the cable bundle. The overall situation was as shown in the schematic of Figure 68.
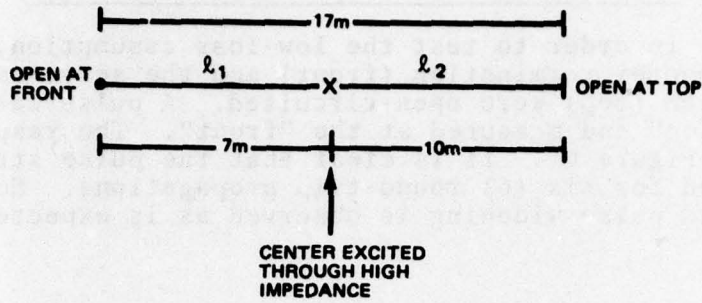
Figure 68.   Cable Entry Point Diagram

Figures 69, 70 and 71 illustrate the propagation
effects for three observation points and serve to emphasize
the "displaced" impulse nature of the low-loss cable impulse
response.   Figure 69 is both center-excited and center-
observed so it can include both the excitation and response
waveform on the same dual trace image.   The separate returns
from the front-end and top-end reflections are clearly
visible as is the effect of the small but non-zero cable
attenuation and dispersion.   Figures 70 and 71 present the
front-end and top-end observations.
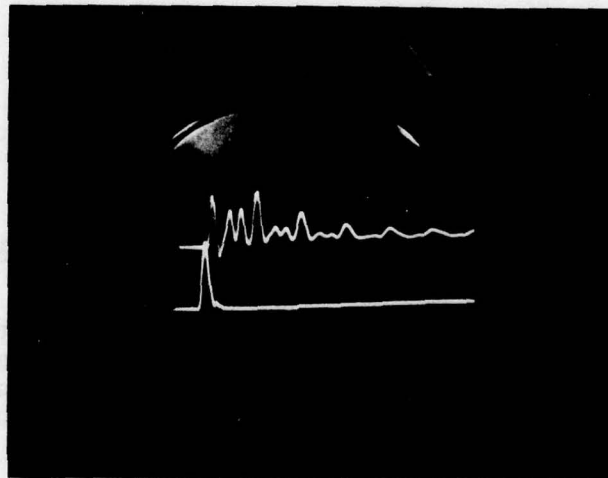
100 n.s./div

Figure 69.   Center Observed
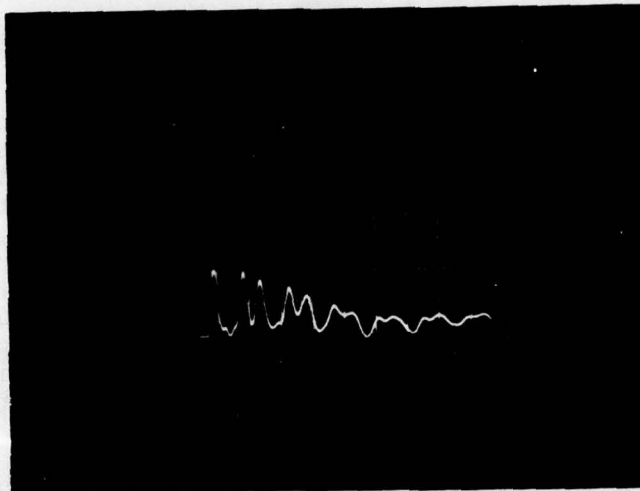
100 n.s./div

Figure 70. Front Observed
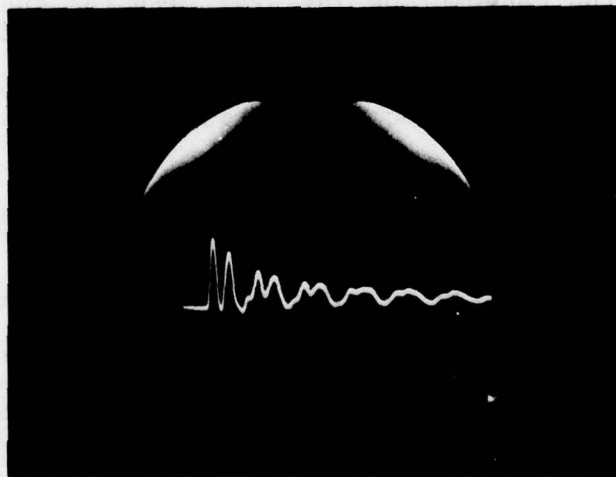
100 n.s./div

Figure 71. Top Observed

81

4.4.2.3 Linearity and Convolution Studies of the Yaw Damper Circuit

According to the abbreviated F-111 servo-computer circuit schematic (Figure 50), the computer itself should appear as a short-circuit to an incident impulse pulse because of the shunting action of the capacitor. At the servo valve end (top), the high inductive reactance, ωL, presents an effective open circuit to the incident pulse. The alternate inversion due to the shorted end is evident in Figures 72a, b and c for the impulse responses measured respectively at the center, top, and front. Although the actual waveshapes are quite complicated due to the inter-action of reflection, attenuation, and dispersion, the presence of the inversion is clearly indicated.

Given the impulse responses, h(t), of Figure 72, the output to any arbitrary input pulse can be calculated from the convolution integral as:

$$y(t) = \int_{-\infty}^{t} x(\tau) \, h(t - \tau) \, d\tau \tag{109}$$

Simulated di/dt lightning pulses scaled to laboratory propor-tions were applied at the center point. The recorded pulse waveforms are presented in Figures 73 and 74. With careful application of the convolution integral with the specific input, x(t), and the three distinct h(t) yields predicted output pulses that agree quite well with the output pulses of Figures 73 and 74. The ability of the convolution inte-gral to predict the output to a known input provides an elegant confirmation of linearity.

4.4.2.4 Verification of Servo-Computer Short Circuit Termination Using RG-58 Cabling

The actual servo-computer module was pulled from the F-111 and used directly in a test configuration using RG-58 cabling. The RG-58 cable configuration allowed a carefully controlled study of the driving point impedance of the servo-computer. In Figure 75, the yaw computer ter-minated the end of a 50 foot section of cable. The short circuit nature of the termination is clearly demonstrated in Figure 76.
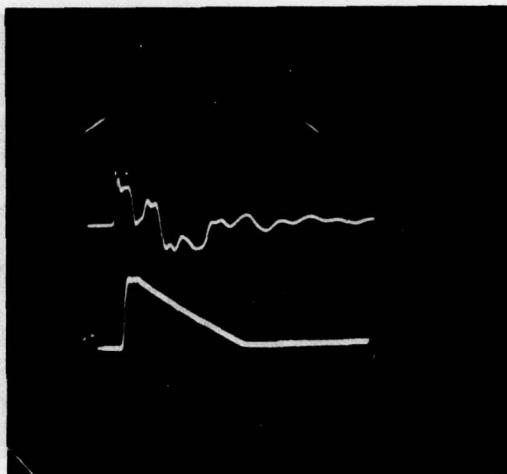
82
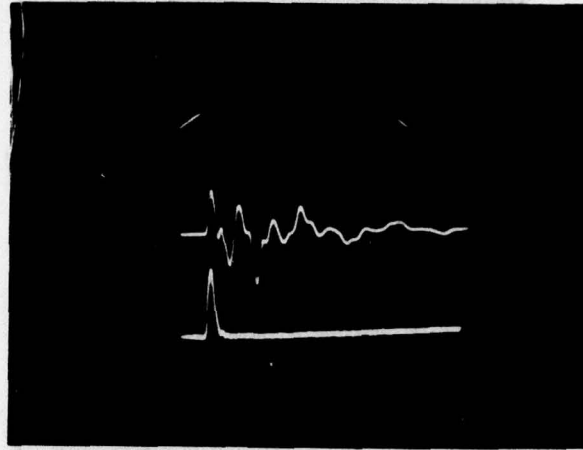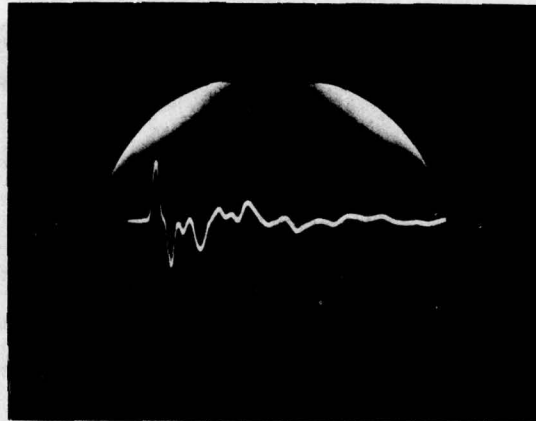
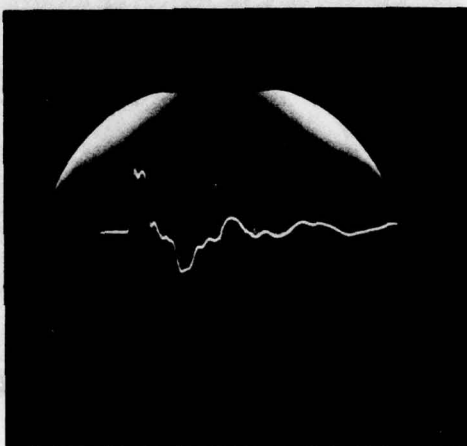(a) Center Observed
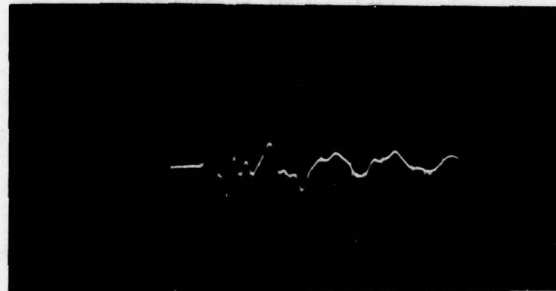
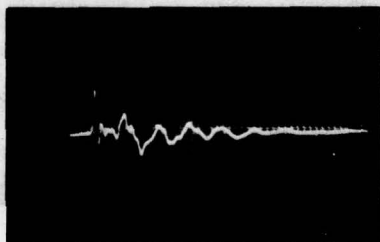

(b) Top Observed

(c) Front Observed

Figure 72. Impulse Response to Top Input of
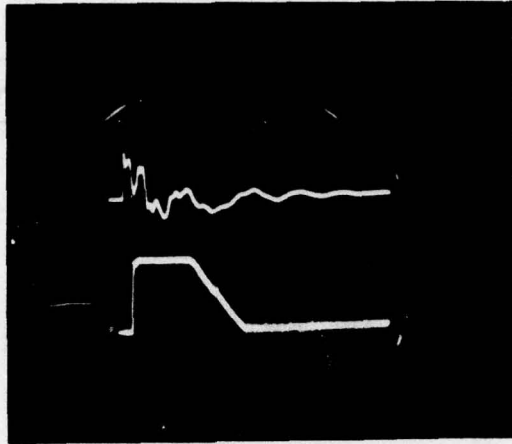Yaw Computer Circuit

83

(a) Center Observed
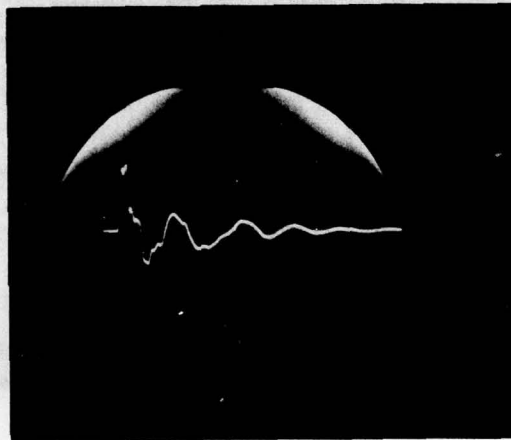

(b) Top Observed
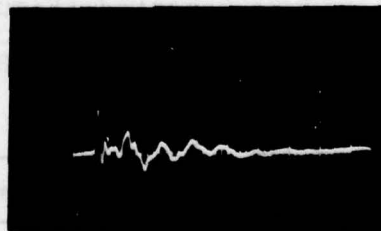

(c) Front Observed

Figure 73. Impulse Response to Center Input
of Yaw Computer Circuit

84

(a) Center Observed

(b) Top Observed

(c) Front Observed

Figure 74. Impulse Response to Front Input of Yaw Computer
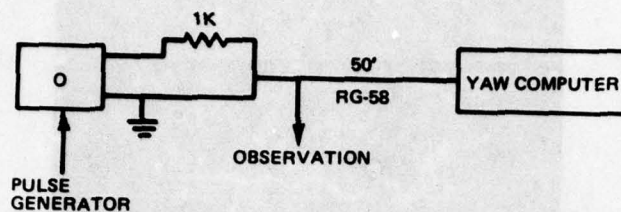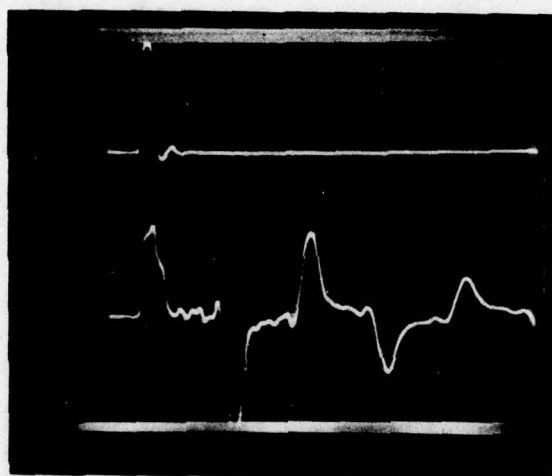
Figure 75. Yaw Computer Test Circuit
for Observation at End of
Cable

200mV/div

100n.s./div

Figure 76. Inverted Return

The identical experiment was repeated (Figure 77) with
the observation now taken at the output jack of the computer
itself. The results are shown in Figure 78.
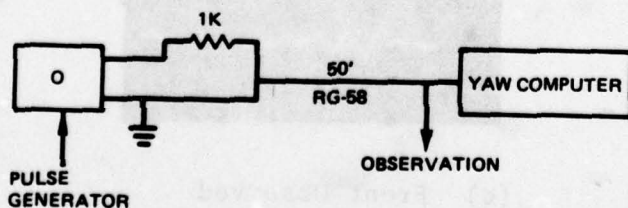
Figure 77. Yaw Computer Test Circuit for
Observation at Output of Yaw Computer

86
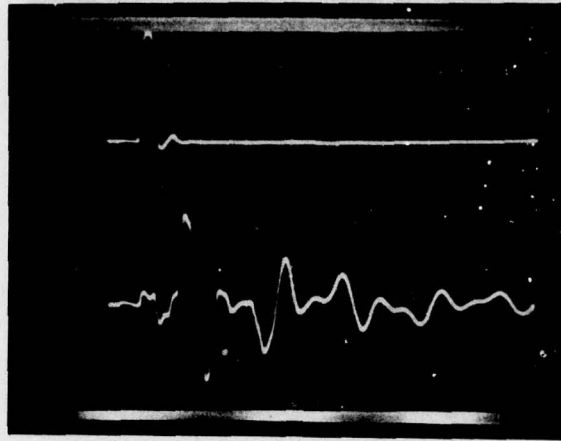
200mV/div

100n.s./div

Figure 78.   Observed at Computer Jack

As a compelling proof of the shorted termination assumption, the servo-computer module was removed and replaced with a four foot (4') section terminated in a dead short (Figure 79). The Figure 80 response was nearly identical to Figure 76, thereby verifying the assumption of a dead-short.
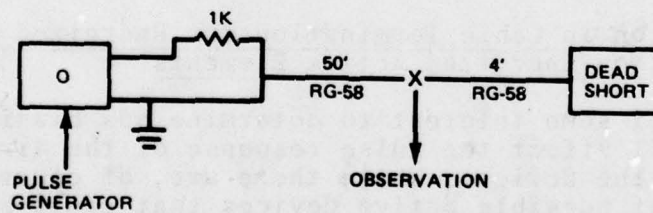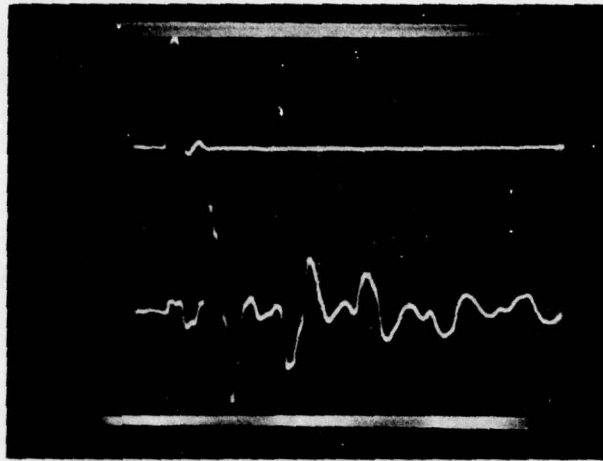

Figure 79.   Yaw Computer Test Circuit for
Observation with Dead Short
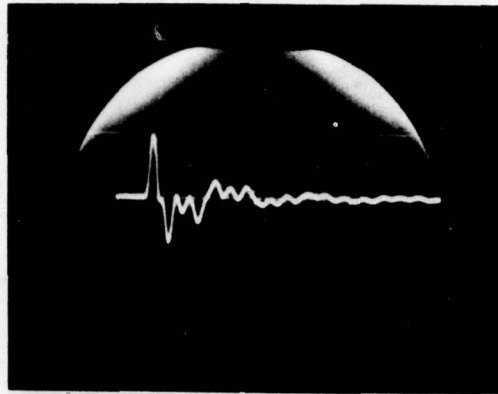
200 mV/div.

100 n.s./div.

Figure 80.   Dead Short Section

4.4.2.5   Amplitude Test for Yaw Damper Circuit Linearity

A simple, direct test for circuit nonlinearity was
performed on the yaw damper circuit. By reversing the
polarity of the excitation impulse and by continuously
varying its magnitude from zero to some maximum value, the
property of homogeneity (i.e., superposition) can be veri-
fied. This test was performed from a center excited, top
observed configuration. Figure 81 presents the results
which clearly illustrate the homogeneity of the circuit.
The amplitude test is simpler than the convolution test and
is particularly well suited to unsymmetrical nonlinearities
like the p-n junction.

4.4.2.6   Variation in Cable Termination for Energized
           Versus Non-Energized Active Elements

It is of some interest to determine how biasing an
active device will affect the pulse response of the aircraft
cable leading to the device. While there are, of course, an
infinite number of possible active devices that could be
considered, the following general statement can still be
made. Namely, that biased or not, most active devices have
input impedances much greater than the characteristic im-
pedance of the cable and, therefore, the device will appear
to the cable as an open circuit. At the other extreme, when
capacitors shunt to ground, the device tends to appear as a
dead-short. For no special reason, a common-emitter ampli-
fier was used to terminate RG-58 cabling in Figure 82 with no
noticeable change being observed in the biased versus un-
biased mode.

88

500mV/div

100n.s./div

(a)　　Uninverted Input
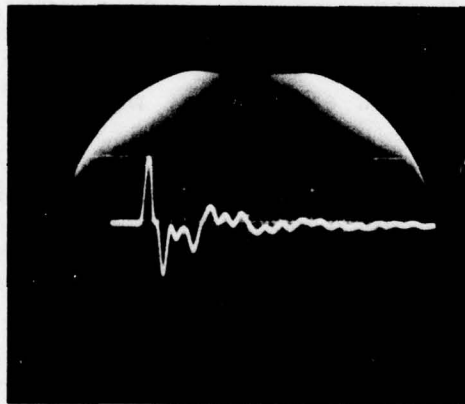
(b)　　Inverted Pulse and Inverted
Amplifier.　Same Image.

Figure 81.　Results of Amplitude Test for Yaw Damper
Circuit Linearity Verification

Input Pulse

Unbiased

Biased

Figure 82.   Effect of Active Element Biasing

4.4.2.7   Time Domain Illustration of the Effect of
Multiple Inputs Using RG-58 Cabling

The significant effects of multiple input excita-
tion are illustrated in Figure 83. As shown in Figure 83(a),
multiple inputs were applied at separate points of the
aircraft cable. Figure 83(b) shows, in the bottom trace,
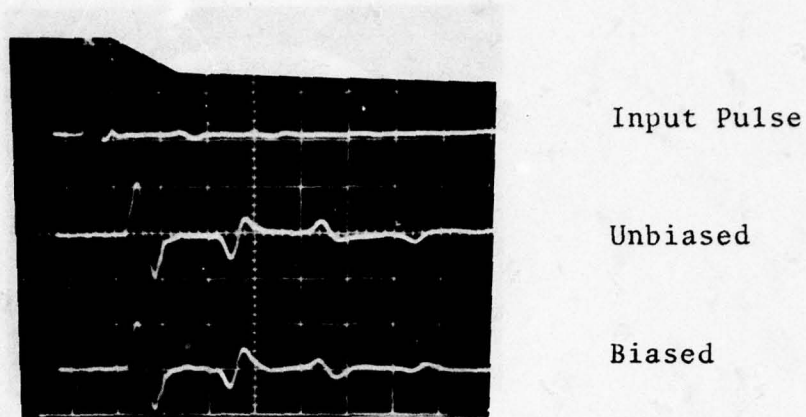the significant effect of the second input. Although the
situation remains linear, various time and frequency domain
techniques should be developed to identify the multiple
input situation.

4.4.2.8   RG-58 Modeling of Yaw Damper Circuit and a
Confirmation of the Analytical Frequency Response
with the Experimental Observed Frequency

Although this discussion could be included in the
frequency response section, it is presented here since it
involves an RG-58 cable simulation. The intent of the
experiment was to model with RG-58 cable the actual yaw
damper experiment carried out on the F-111. From propaga-
tion time measurements it was determined that the "stripped,"
center-excited point was around 7.5 meters from the shorted
servo computer termination. The RG-58 configuration of
Figure 84 most nearly approximates the correct length propor-
tionality. Figures 85, 86 and 87 illustrate the response of
the cable to various inputs and should be compared to the
top observed pulses of Figures 70, 71 and 72. The similarity
is clearly evident confirming the validity of the present
modeling of the damper circuit.

90
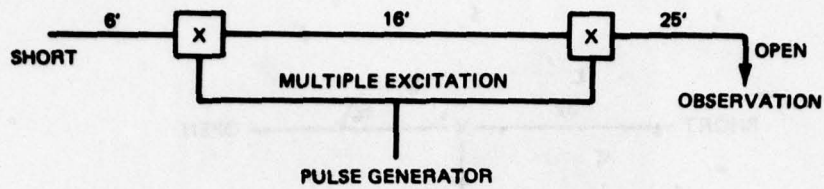
(a) Circuit for Multiple Input Study
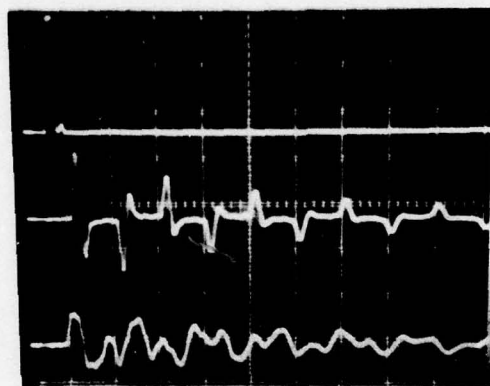
(b) Effect of Multiple Input

Figure 83.   Effects of Multiple Inputs
Using RG-58 Cabling

91

SHORT ———— 32' ——— X —— 50' ———— OPEN

PULSE GENERATOR

Figure 84.   RG-58 Circuit Configuration of
Analytical Frequency Response

200mV/div

100n.s./div

Figure 85.   Impulse Excitation;
Open End Observed

92
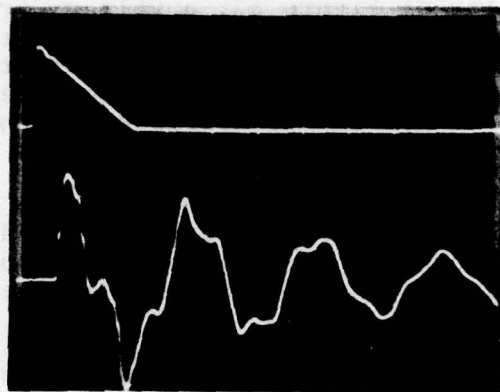
200mV/div

100n.s./div

Figure 86. "Saw Tooth" Excitation;
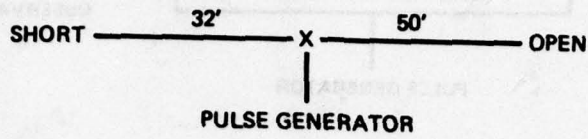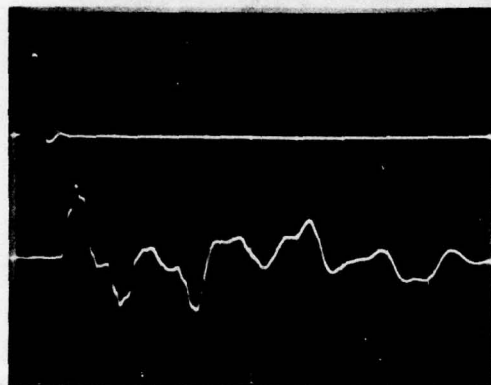Open End Observed
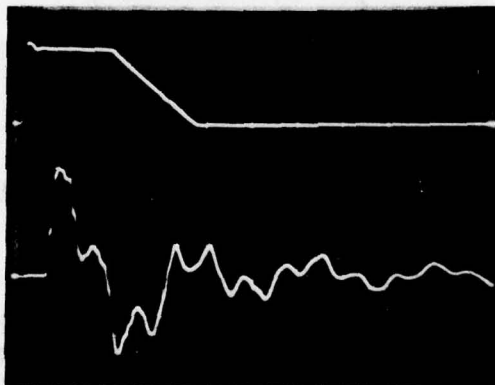
200mV/div

100n.s./div

Figure 87. Trapezoidal Excitation;
Open End Observed

93

With the configuration of Figure 87, a voltage transfer function was measured and then calculated using the accurately known lengths and attenuation characteristics of RG-58 cable. Figure 88 shows the remarkable agreement between measured and analytical which reconfirms again the basic accuracy of the analytical model of the previous section.

Frequency tests were also performed on the yaw damper circuit of the F-111 from a center-excited configuration. Figures 89 through 91 illustrate the measured transfer function. As expected, the three resonant peaks are clearly in evidence.

As a final remark on the frequency domain, a series of tests were performed to investigate the skin resistance effect. From electromagnetics, the skin resistance should vary directly as $\sqrt{f}$ so that the Q = Center Frequency/Bandwidth should increase with increasing frequency. For the RG-58 cable, Table III presents the increasing bandwidth at ever increasing resonant frequencies. This result was expected.

TABLE III.   BANDWIDTH vs RESONANT FREQUENCY

f_c (MHz)	BW (MHz)
6.25	0.70
12.50	1.10
18.75	2.00

4.5 Capacitive versus Inductive Coupling Using Van Bladel's Expressions

4.5.1   General Discussion

The following short subsection could perhaps have been included in the aperture coupling section. However, since it involves a direct prediction of the peak voltage magnitudes of the respective capacitive and inductive voltage excitations, it constitutes an important link between the aperture coupling and the pulse response of the aircraft cabling. Therefore, it is included here.
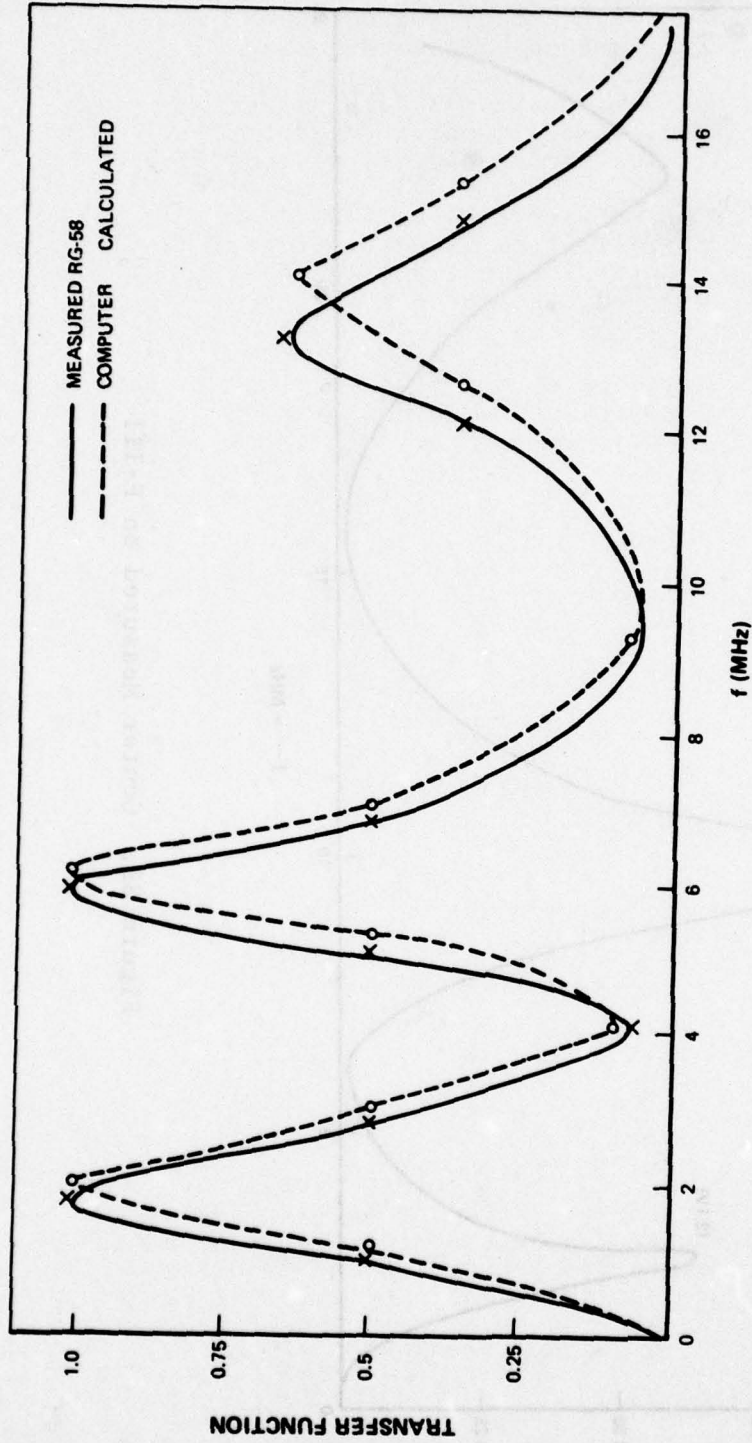
Figure 88. Comparison of Measured and Calculated Transfer Function

95
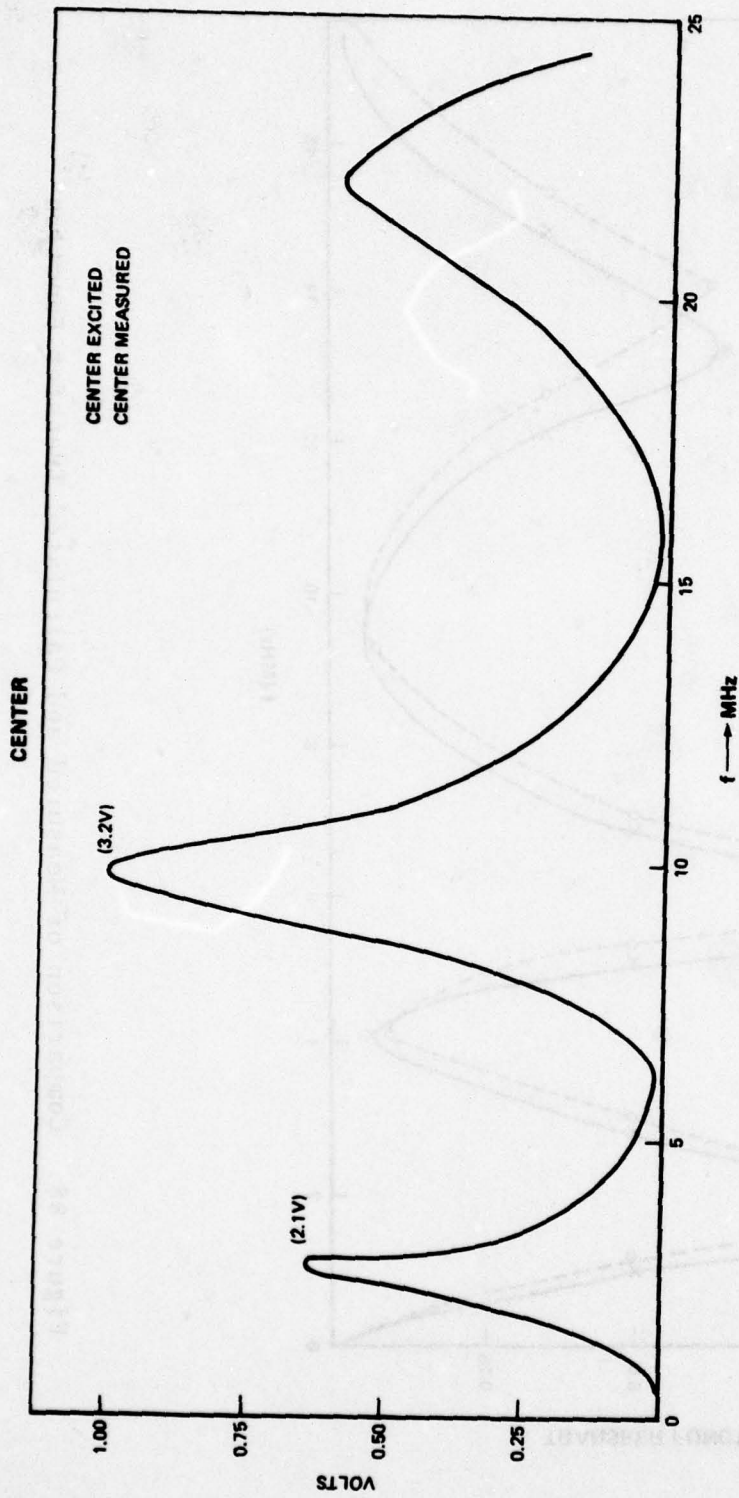
Figure 89. Center Measured on F-111
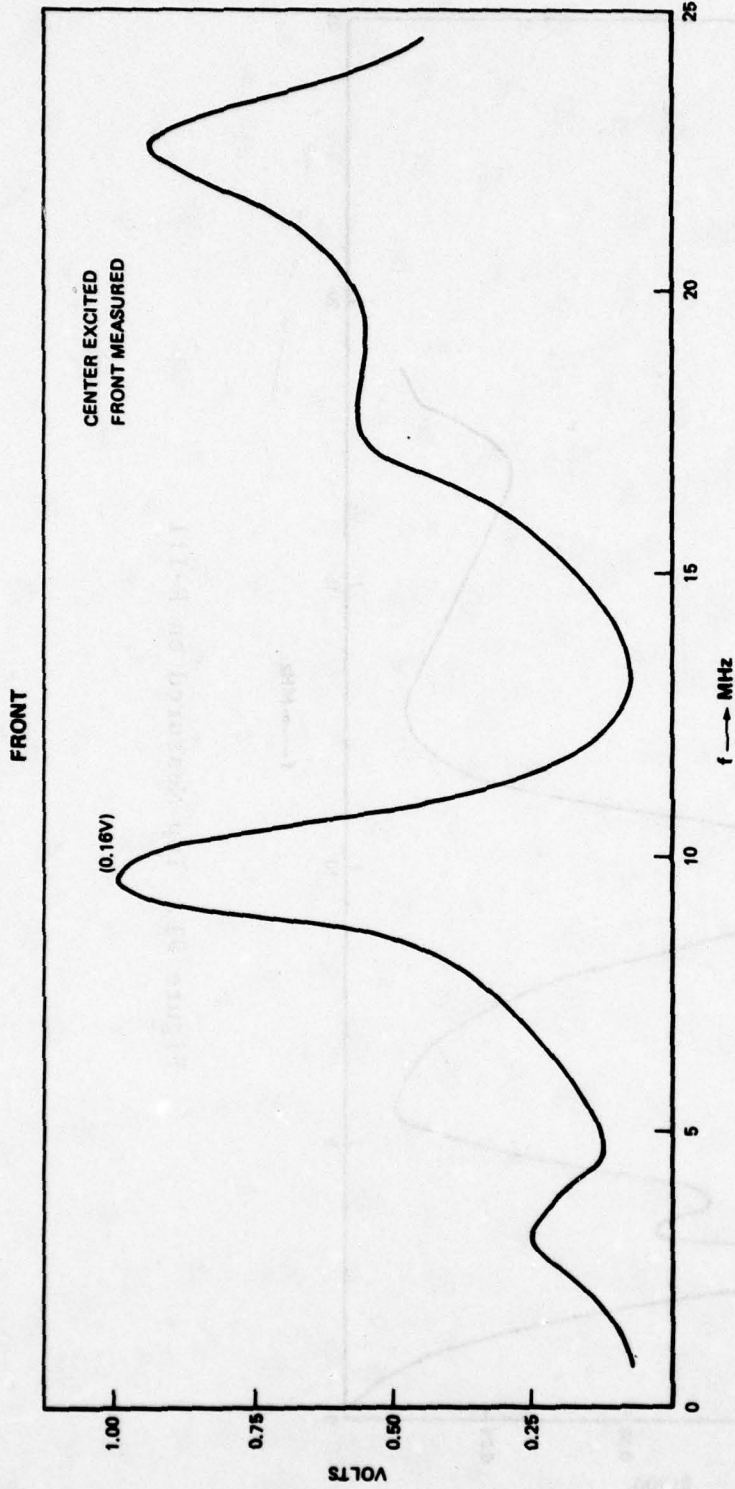
Figure 90. Front Measured on F-111
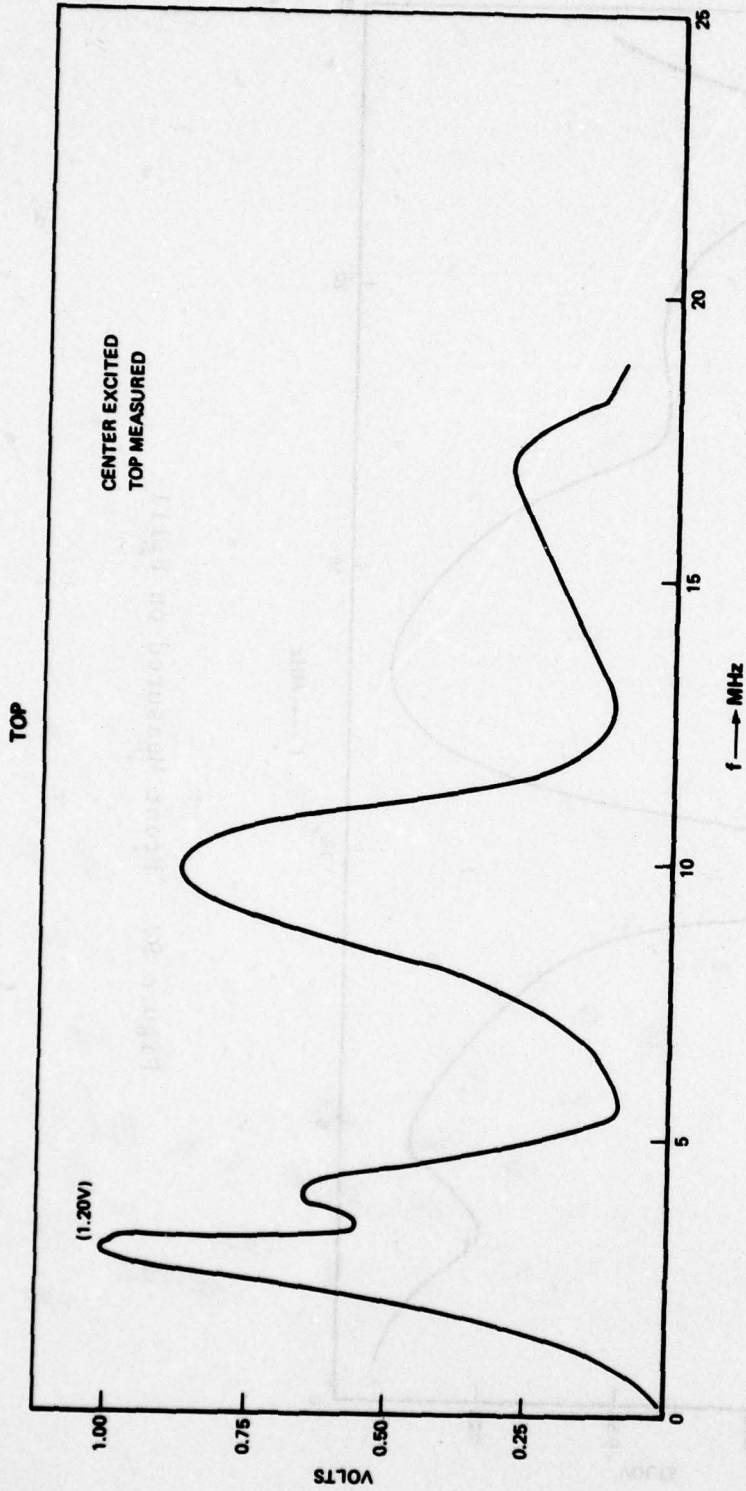
Figure 91. Top Measured on F-111

98

4.5.2 Detailed Discussion

4.5.2.1 $\vec{E}$ Field (Capacitive Effect)

Voltage excitation appears on the circuit due to induced displacement current (see Figure 92).
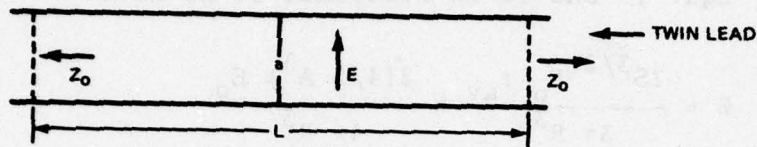
L = LENGTH OF SIGNIFICANT $\vec{E}$ FIELD COUPLING

Figure 92. Diagram of $\vec{E}$ Coupling

Under a worst case assumption, the displacement current can be expressed as:

$$I_D = J_D \times L \times a \qquad (110)$$

Now:

$$J_D = \epsilon_o \frac{\partial E}{\partial t}$$

and:

$$E = \frac{k^E v_A}{d}$$

where E is the electric field at the cable,

k^E is the far-field ratio of E to the aperture field E_o,

v_A is the LST aircraft voltage to ground at aperture, and

d is distance from aperture to ground return (NOTE: $E_o = \frac{v}{d}$).

The resulting voltage pulse on the line then equals $I_0 Z_0$ <u>or</u>:

99

$$v_c(t) = \frac{\varepsilon_o \, k^E \, v_A \, L \, a \, Z_0}{d} \, \delta(t) - \frac{1}{T_c} \, e^{-t/T_c} \, \mu(t) \qquad (111)$$

4.5.2.2 Calculation of k^E from Van Bladel's Dipole Expression

Eqs. 13 and 15 in Reference 11 we have:

$$E \approx \frac{2S^{3/2} \, E_o \, \tau_{av}}{3\pi \, R^3} \approx \frac{2(4/3 \, A^3) \, E_o}{4\pi \, R^3} \qquad (112)$$

where A equals the radius of the aperture ($A \approx 0.63$ m for cockpit). It follows that:

$$k^E = \frac{E}{E_o} = 14.4 \times 10^{-3} \Bigg|_{\substack{A = 0.63 \text{ m} \\ R = 1.23 \text{ m}}} \qquad (113)$$

Therefore, with the following parameters,

$V_A = 20,000$ (LST) (With linear variation; cockpit at mid-point; capacitor charge voltage equals 40,000 volts)

$d = 2$ m

$Z_0 = 100\Omega$

$a = 5$ mm $= 5 \times 10^{-3}$ m

$L = $ to be determined

$k^E = 7.2 \times 10^{-3}$

It follows that:

$$v_c(t) \approx L \, 6.38 \times 10^{-9} [\delta(t) - 1.4 \times 10^6 \, e^{-t/0.7 \times 10^{-6}} \, \mu(t)] \qquad (114)$$

100

4.5.2.3 Interpretation of $\delta(t)$

The Dirac delta function can, of course, not be supported on a finite bandwidth system. For the LST 30 MHz system, the $\delta(t)$ appears as a 33 nanosecond pulse with a magnitude of 30×10^6 [area of unity] to give:

$$v_c(t) \simeq 210 \times 10^{-3} L[\mu(t) - \mu(t - 33 \times 10^{-9})]$$

$$- 8.84L \times 10^3 e^{-t(0.7 \times 10^{-6})} \mu(t) \quad \text{(volts)}$$

For input-output impulse responses that contain at least one inversion (one shorted termination), the output peak value can not exceed the initial maximum value of the input. Therefore, only the 33×10^{-9} sec. pulse will produce a significant response and the $e^{-t(0.7 \times 10^{-6})} \mu(t)$ component can be neglected.

Accordingly, $v_c(t)$ can be well represented by:

$$v_c(t) \simeq 210L[\mu(t) - \mu(t - 33 \times 10^{-9})] \text{ millivolts.}$$

4.5.2.4 Calculation of $\vec{H}$ Field (Inductive) Effect

Calculation of the inductive effect is done from Figure 93 as follows:
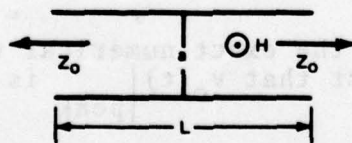
Figure 93. Diagram of $\vec{H}$ Coupling

Now:

$$v_L(t) \Big|_{peak} \approx \frac{d\phi}{dt} \approx \mu_o \frac{H_{peak}}{\Delta t} 5 \times 10^{-3} L a k^H \quad (115)$$

where:

$$\frac{H}{H_o} = k^H \approx \frac{2\rho_n}{4\pi R^3} \approx \frac{2 \times 0.47a S^{3/2}}{4\pi \times (1.53)^3} \approx 0.03$$

for the parameters given in the $\vec{E}$-field case. For an
$a = 5 \times 10^{-3}$ m, a H_{peak} of 200 amp/m, a current rise time,
Δt, of 0.7 μsecs, we get:

$$v_L(t) \approx L 55 \times 10^{-3} e^{-t/0.7 \times 10^{-6}} \mu(t) \text{ (volts)} \quad (116)$$

Assuming that the regions of influence for both the $\vec{E}$ and $\vec{H}$
are equal, the ratio of peak values for $v_L(t)$, $v_c(t)$ can be
given as:

$$\frac{v_c(t) \Big|_{peak}}{v_L(t) \Big|_{peak}} \approx 4:1 \quad (117)$$

As before, the exact numerical values are <u>not</u>
important but the fact that $v_c(t) \Big|_{peak}$ is of the same order

of magnitude as $v_L(t) \Big|_{peak}$ is of <u>great</u> interest.

102

5. SYSTEM CONSIDERATIONS

Because this section addresses certain problems that have been controversial throughout the history of LTA, its impact is significant and should be of great interest to the reader. Specifically, this section deals with the following topics: Which physical variable may be scaled, the proper procedure for amplitude scaling, a technique for compensating for configuration effects, a postulated LTA model, an input/output linear system analysis, and a frequency technique for determining the relative amounts of capacitive versus inductive coupling.

5.1 Choice of Physical Variable for Amplitude Scaling

5.1.1 General Discussion

The question of which physical variable may be scaled is addressed. It is concluded that any of the physical effects of the pulsing capacitor energy (i.e., i, v, $\frac{di}{dt}$, or $\frac{dv}{dt}$) may be defined by measurement and scaled to the levels of interest as a direct consequence of system homogeneity.

5.1.2 Detailed Discussion

This discussion considers the proper amplitude scaling of the physical variables i, $\frac{di}{dt}$, v, and $\frac{dv}{dt}$. It specifically addresses the proposition that "the lack of a transient voltage oscillation at all zero crossings of an oscillatory current input proves conclusively that the coupling is capacitive and not inductive" (Reference 9).

For the current and voltage levels of interest, there is no compelling reason to assume that the system is not linear. Assuming linearity and an initially relaxed system before pulsing, the measured output (voltage or current) must obey the homogeneity property of linear system with respect to the physical cause or input (current or voltage). Simply put, the homogeneity property states that if an x(t) input produces y(t) output, then βx(t), as an input, produces an output of βy(t). It is emphasized that the fundamental nature of the coupling is totally irrelevant. The important quality is linearity which, because of homogeneity, allows extrapolation on the physical cause (i.e., the driving current).

Considering the LTA configuration as a series, R-L-C circuit, the LTA discharge current waveform as a function of bank capacitance, C, bank voltage, V, overall series resistance, R, and aircraft bulk inductance, L, is as follows:

103

$$i(t) = \frac{V}{R} \left\{ e^{-t/RC} - e^{-R/L\,t} \right\} \mu(t)$$

$$\approx \frac{V}{R} \left\{ 1 - e^{-R/L\,t} \right\} \mu(t) \tag{118}$$

since $1/RC \ll R/L$.

Since the initial transient is excited by some capacitive or inductive coupling, the direct physical input or cause will be proportional to di/dt (or dv/dt). We can now evaluate di/dt for $1/RC \ll R/L$ as:

$$\frac{di}{dt} \approx \frac{V}{L} e^{-R/L\,t} \mu(t) \qquad \text{(discontinuous at t=0)} \tag{119}$$

which can be rewritten as:

$$\frac{di}{dt} = \frac{V}{L} \mu(t) - \frac{V}{L} \left\{ 1 - e^{-R/L\,t} \right\} \mu(t) \tag{120}$$

$$= \nu_1(t) - \nu_2(t)$$

which is the sum of an input $\nu_2(t)$, continuous at t=0 and an input $\nu_1(t)$, discontinuous at t=0. With the leading edge of the oscillatory wave matched to the unipolar pulse, the expression for di/dt becomes:

$$\frac{di}{dt} = \frac{V}{L} \mu(t) - \frac{V}{L} (1 - e^{-\alpha t} \sin \omega_o t) \mu(t) \tag{121}$$

where the $\frac{V}{L} \mu(t)$ is the same $\nu_1(t)$ input as the $\nu_1(t)$ of the unipolar $\frac{di}{dt}$ of Eq. 119. It is postulated here that the induced transient is produced by the $\nu_1(t) = \frac{V}{L} \mu(t)$ step function input and is, in fact, the oscillatory response of some resonant circuit to a step input. Since the $\nu_1(t)$

104

input is common to both unipolar and oscillatory inputs, the damped oscillatory transient must be the same for both inputs and should occur only once after the instant of firing as is, in fact, observed. By superposition, the common step response is then added to a response given by the convolution integral:

$$Y_2(t) = \int_0^t \nu_2(\tau) \, h(t-\tau) d\tau \qquad (122)$$

where $\nu_2(t)$ is the unipolar or oscillatory input and the $h(t)$ is the impulse response between the input and the measurement point. It is this $Y_2(t)$ which is added to the common transient step response to give the total response. Because $\nu_2(t)$ differs in the unipolar and oscillatory inputs, the $Y_2(t)$ will differ also. In both cases, neither the unipolar nor oscillatory $\nu_2(t)$ inputs have enough energy at frequencies high enough to excite the illustrated frequency responses. Only the discontinuous $\nu_1(t)$ step function can effectively excite the transient. Thus, the question of capacitive versus inductive coupling is irrelevant since the system remains linear regardless of the coupling mechanism.

In summary, the homogeneity property alone permits proper amplitude scaling on any physical variable (i, $\frac{di}{dt}$, v, $\frac{dv}{dt}$) provided only that the waveform remains invariant. The nature of the coupling affects only the detailed structure of the linear operation but not its basic linearity or homogeneity.

5.2 Proper Technique for Amplitude Scaling

5.2.1 General Discussion

The technique presented here defines a proper procedure for LTA amplitude scaling. It permits the prediction of the system response to a desired input from the recorded response of the system to a known input. The proposed procedure does not compensate for LTA configuration effects (see next section) but does allow a simple, direct, easily programmable output extrapolation for any arbitrary input. As a result, it allows a rapid calculation of system outputs to a large ensemble of possible inputs.

5.2.2 Detailed Discussion

The following analysis considers the proper technique for amplitude scaling. Referring to Section 1.2, the LST situation can be represented as:

105

$$\boxed{k_1 I_1(\omega)} \text{---} \boxed{T(\omega)} \text{---} = S_{LST}(\omega)$$

Figure 94.   LST Situation

where k_1 is the magnitude of the peak skin current, $i_1(t)$, and $T(\omega)$ represents both the aperture coupling and cable responses. The airborne situation can be described in a similar manner as:

$$\boxed{k_2 I_2(\omega)} \text{---} \boxed{T(\omega)} \text{---} = S_{AIR}(\omega)$$

Figure 95.   Airborne Situation

Combining Figures 94 and 95:

$$\left[\frac{k_2}{k_1}\right]\left[\frac{I_2(\omega)}{I_1(\omega)}\right] S_{LST}(\omega) = S_{AIR}(\omega) \tag{123}$$

For the case where $i_2(t) = i_1(t)$, $I_2(\omega) = I_1(\omega)$, and simple amplitude scaling is proper. However, when $i_1(t) \neq i_2(t)$, the proper expression for $S_{AIR}(t)$ is:

$$\left[\frac{k_2}{k_1}\right] F^{-1}\left[\frac{I_2(\omega)}{I_1(\omega)}\right] * S_{LST}(t) = S_{AIR}(t) \tag{124}$$

where * represents a convolution in the time domain. When $i_1(t) = i_2(t)$:

$$F^{-1}\left\{\frac{I_2(\omega)}{I_1(\omega)}\right\} = \delta(t) \quad \text{(Dirac Delta Function)}$$

106

and, as expected:

$$\left[\frac{k_2}{k_1}\right]\left[\delta(t) * S_{LST}(t)\right] = \left[\frac{k_2}{k_1}\right] S_{LST}(t) = S_{AIR}(t) \quad (125)$$

However, this is not the usual case. Assuming a double exponential for $i_2(t)$, $i_1(t)$, we can perform the inverse transform as indicated in Eq. 126. Specifically, let:

$$i_2(t) = i_{AIR}(t) = k_2\left[e^{-\alpha_2 t} - e^{-\beta_2 t}\right]\mu(t)$$

$$(126)$$

$$i_1(t) = i_{LST}(t) = k_1\left[e^{-\alpha_1 t} - e^{-\beta_1 t}\right]\mu(t)$$

which yields, after considerable manipulation:

$$\left(\frac{k_2}{k_1}\right) F^{-1}\left\{\frac{I_2(\omega)}{I_1(\omega)}\right\} = \left[A e^{-\alpha_2 t} + B e^{-\beta_2 t}\right]\mu(t) \quad (127)$$

where:

$$A = \left(\frac{k_2}{k_1}\right) \frac{(\alpha_1 - \alpha_2)(\beta_1 - \alpha_2)}{(\beta_1 - \alpha_1)}$$

$$B = \left(\frac{k_2}{k_1}\right) \frac{(\alpha_1 - \beta_2)(\beta_1 - \beta_2)}{(\beta_1 - \alpha_1)}$$

The convolution of Eq. 124 can be computer-calculated and correct amplitude scaling performed on the output.

107

5.3 Decoupling LST Configuration Effects

5.3.1   General Discussion

The technique for decoupling LST configuration effects presented here promises to be the most significant contribution of this study. Using concepts very similar to those of the previous subsection, a technique is advanced that can predict the actual airborne response from the observed LST response. One added physical measurement is required along with a knowledge of how the aircraft skin current density vector field responds to various types of lightning excitation (e.g., remote, direct with varying entrance and exit points, etc.). With this technique the LST tests can be applied with confidence to the airborne situation.

5.3.2   Detailed Discussion

The following advances a method to isolate or decouple the LST configuration response from the aircraft response permitting thereby a realistic extrapolation from measured LST induced voltages to the actual voltages expected in flight.

The principal assumption is that the aircraft cabling does not significantly load the aircraft cylinder. With this assumption, we can then define a separate cylinder and avionics transfer function whose product equals the overall LTA transfer function. The assumption of no loading allows the aircraft cylinder transfer function to be measured with the avionics in place. The overall configuration can be drawn as follows:
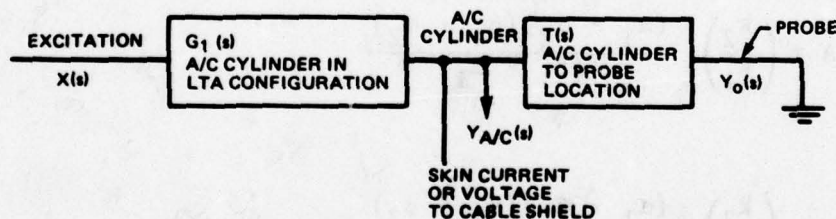

Figure 96.   Aircraft Cylinder and Avionics
Transfer Function

$G_1(s)$ can be estimated experimentally by measuring the air-craft cylinder response to a known input and solving for $G_1(s)$ as:

$$G_1(s) = -\frac{Y_{A/C}(s)}{X(s)} \qquad (128)$$

With the $G_1(s)$ defined, the important $T(s)$ transfer function can be determined as:

$$T(s) = \frac{Y_o(s)}{X(s)\ G_1(s)} \qquad (129)$$

To extrapolate to the airborne situation, a new $G_2(s)$ must be defined which relates the skin response to a real-life light-ning strike. Since the lightning current enters at one point and leaves the aircraft at another point, the transfer function will probably be the surge impedance of the aircraft cylinder --an impedance which can be defined from the dimensions of the aircraft. As a final step, the overall in-flight transfer function can be stated as:

$$G_2(s)T(s) \qquad (130)$$

which should accurately represent the situation. In summary, the method involves the following steps:

a. Estimate $G_1(s)$ by measuring LST aircraft cylinder response to a known input near the dominant aperture.

b. With $G_1(s)$ defined, estimate $T(s)$ from measured probe induced voltages.

c. Analytically define the $G_2(s)$ or surge impedance of A/C cylinder. This step may also require a know-ledge of skin current density response as suggested earlier.

d. Define the airborne transfer function $G_2(s)T(s)$ and predict true aircraft response, $y(t)$, to an arbi-trary input, $x(t)$, or:

$$y(t) = L^{-1}[X(s) \, G_2(s)T(s)] \qquad (131)$$

e. Perform magnitude scaling on the response calculated in sted d.

5.4 A Postulated LTA Model

5.4.1 General Discussion

A postulated LTA model is now presented that is able to explain some commonly observed LTA signal phenomena. The following explanation was proposed early in the present work period and has been found to be consistent with all observed LTA waveforms.

5.4.2 Detailed Discussion

It is proposed that the LST current component can and does magnetically, or capacitively, couple to the internal aircraft cabling and can and does appear in the induced voltage output but only if the aircraft cabling responds significantly at 3.00 MHz*. Superimposed on the 3.00 MHz aircraft cable response, if any, is the response of the internal aircraft circuitry to the step function, $\mu(t)$ of $\frac{di}{dt}$.

The above interpretation is well verified by the yaw-damper servo runs. Referring to Figure 50 in Section 4.1.2.3, the observation points for the yaw computer and yaw damper circuits are positioned 13m apart using conventional braided, shielded, single-point-ground aircraft cable. At the frequencies of interest, the inductive reactance of the servo valves is much greater than the characteristic impedance of the cable. Accordingly, the cable can be represented as an open-circuited transmission line (Figure 97) excited by a source described by:

$$i_s(t) = \mu(t) \, e^{-t/T.C.} \, \cos(f_R t) \, \alpha \, \frac{d}{dt}[I_1 + I_2] \qquad (132)$$

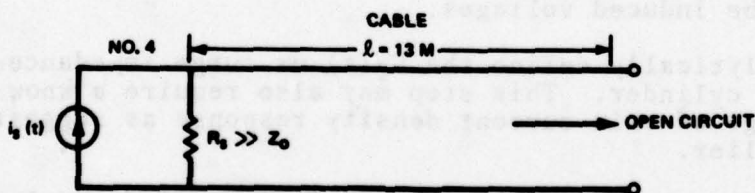Figure 97.. Yaw Circuit Cable Equivalent Circuit

---

* Lower LTA frequency due to longer LTA assembly used in the Eglin AFB test

FILE: F111 1832

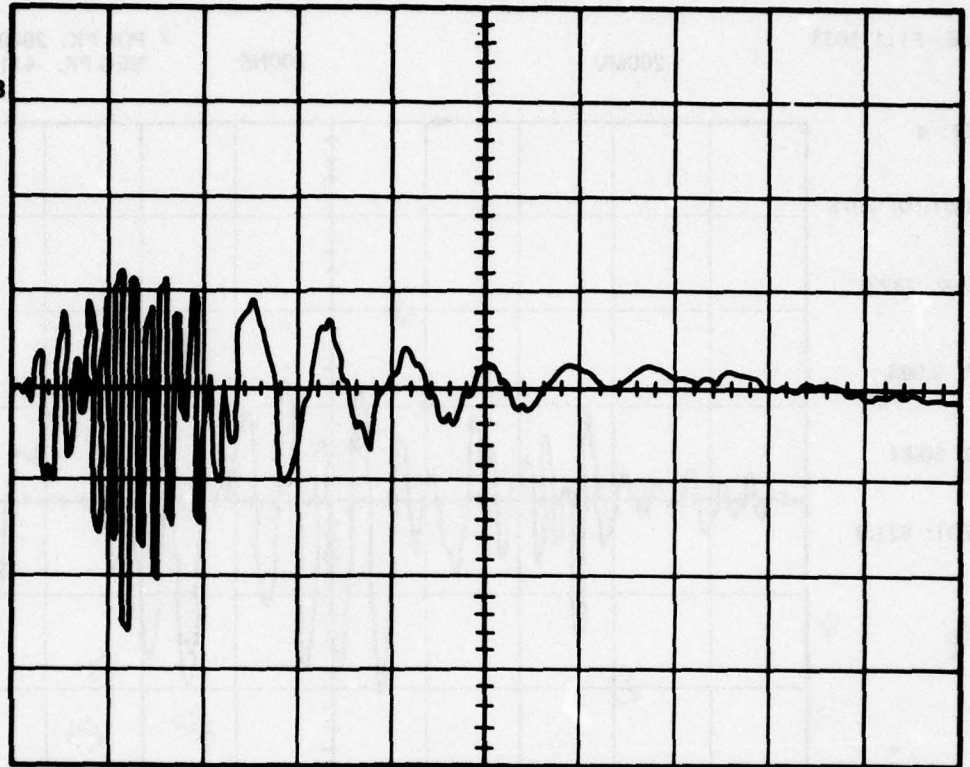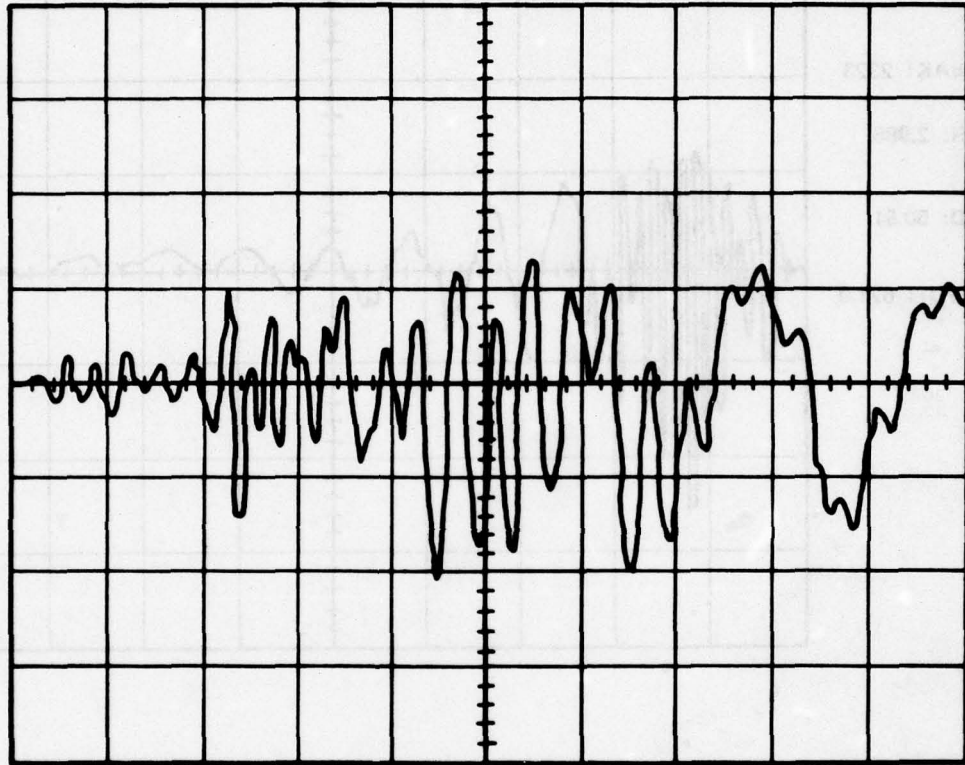200MV   500NS

POS PK: 2466
NEG PK: -5206

CKT: 4

INPUT ID: 3078

PEAK: 2323

TR: 2.988

TD: 50.81

DI/DT: 621.9

0 DIV

Figure 98. Measurement from the Yaw Computer Circuit

111

Figure 99. Measurement from the Yaw Computer Circuit

The open circuit line has a resonant frequency at $\lambda = 2\ell_{cable}$ or a $\lambda = 26$ m for a f_{cable} of ≈ 12MHz. The presence of the 12MHz transient is completely verified by all recorded yaw computer and yaw damper servo circuit waveforms. In all cases, it is the response of the open circuit line to the $\mu(t)$ of the $i_S(t)$ effective input since it is the $\mu(t)$ component which supplies an input spectral line at 12MHz. It is only at the front of the aircraft, the yaw computer circuit, where the 3.00 MHz component of $\frac{d\phi}{dt}$ can be coupled into a wide band circuit (e.g., probe). The 3.00 MHz response is observed as verified in Figures 98 and 99. The response of the yaw damper servo circuit (at the rear of the aircraft) will never contain a 3.00 MHz component but only a 12 MHz component inasmuch as its transfer function is narrow-band and peaks at 12 MHz as is shown in Figure 100.
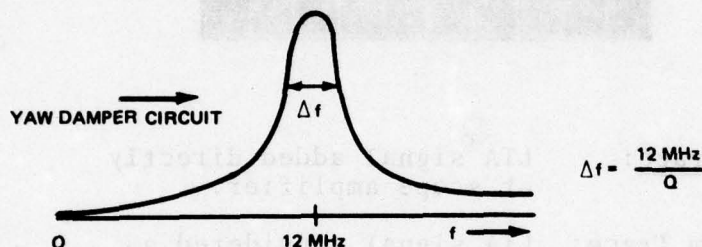
Figure 100. Predicted Spectral Response of
Yaw Damper Circuit

Figures 101 and 102 are of the yaw computer circuit response and illustrate the absence of 3.00 MHz and the presence of the classic 12 MHz, second-order resonant response.

Recent tests at AFFDL also confirm the model. Using a 1-foot loop, the responses of Figures 104 through 106 were recorded near the cockpit aperture. Since the one-foot loop was essentially wide-band, a clear 4.25 MHz*is to be expected as is confirmed.

In order to verify the postulated model, a RG-58 simulated LTA oscillation component was added to an induced transient in two separate ways. In the first experiment, the 2.5 MHz signal is added algebraically to the induced waveform without passing through the transfer characteristic of the cable. A signal situation is observed that is very similar to the yaw computer circuit responses recorded under actual testing. The second experiment actually passed the 2.5 MHz signal through the cable transfer function which effectively filtered out the LTA oscillation as shown.

*Higher LTA resonant frequency of 4.25 MHz due to shorter LTA assembly at WPAFB.

A similar explanation was advanced in Reference 6 by Burrows. While this reference did not discuss specific details, Burrow's observation should be acknowledged.
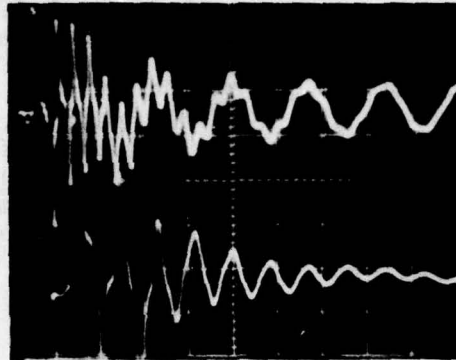
Top Trace: LTA signal added directly at scope amplifier.

Bottom Trace: LTA signal considered as part of signal. Not passed by cable transfer function.

Figure 101. Response of Yaw Damper Servo Circuit

5.5 Input/Output Linear System Analysis

5.5.1 General Discussion

This section deals with a linear system input/output description where the input is the measured LST current waveform and the output is the measured voltage waveform at some circuit point of interest. Regardless of the specific physics interrelating the input and output waveforms, they can be related in a general way given the condition of linearity.

5.5.2 Detailed Discussion

For any linear, time invariant system, the output can be written from superposition in the form of the convolution integral:

50MV

200NS

POS PK: 169
NEG PK: -1918

CKT: 7

INPUT ID: 3081

PEAK: 2172

TR: 2.937

TD: 0

DI/DT: 591.6
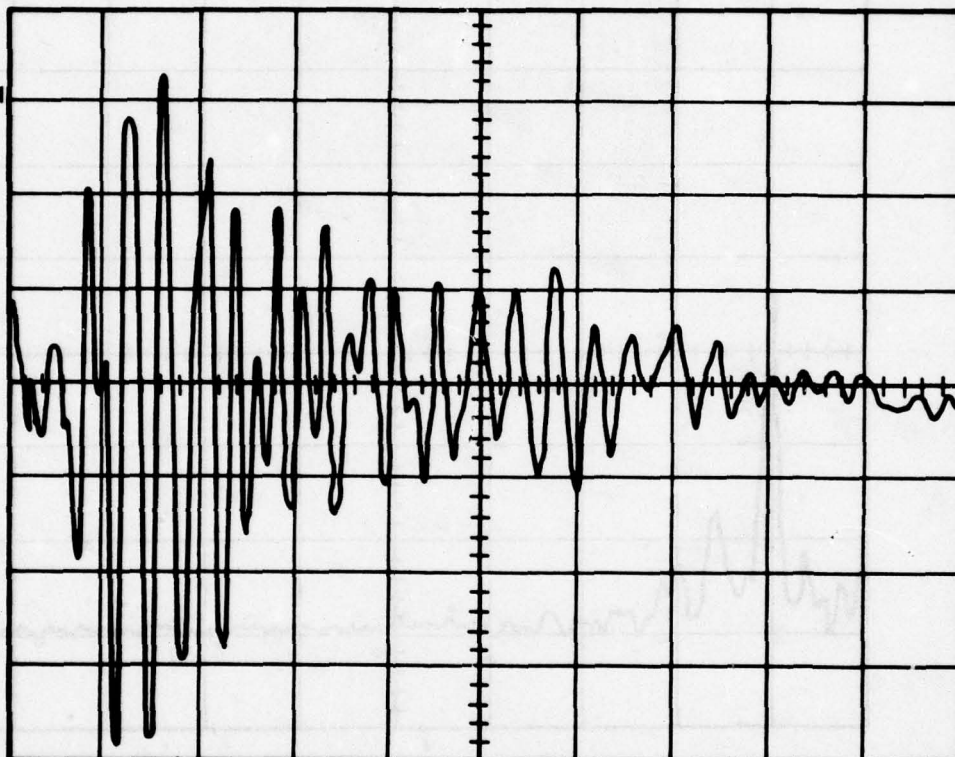
0 DIV

Figure 102. Measurements from Yaw Damper Servo Circuit

115
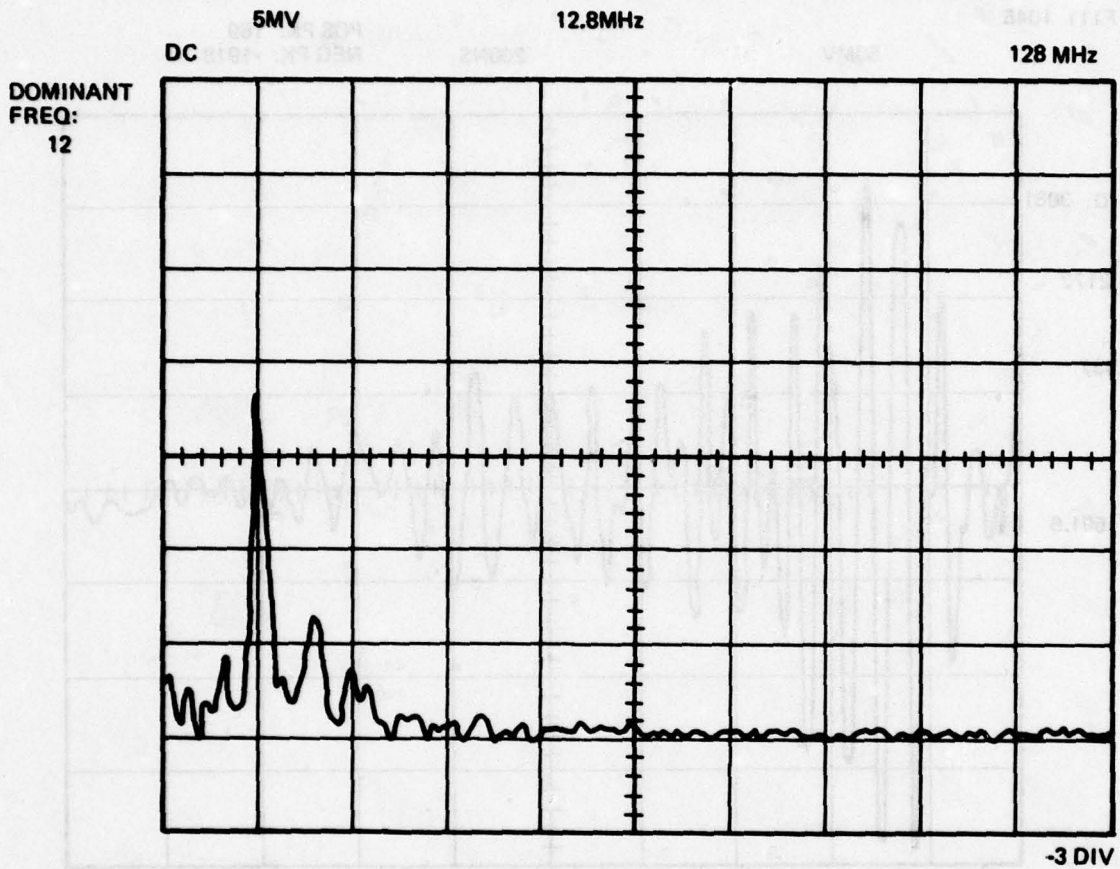
Figure 103. Spectral Measurement from Yaw Damper Servo

FILE: F111 1050

5V   200NS

POS PK: 8.167
NEG PK: -8.666

CKT: 0

INPUT ID: 3050

PEAK: 2334

TR: 1.351

TD: 0

DI/DT: 1382

-6

0 DIV

Figure 104.   Loop Measurement Near Cockpit Aperture

117

FILE: F111 1050

100MV   2.56MHz

DC   25.6 MHz

DOMINANT
FREQ. 4.1

-3 DIV
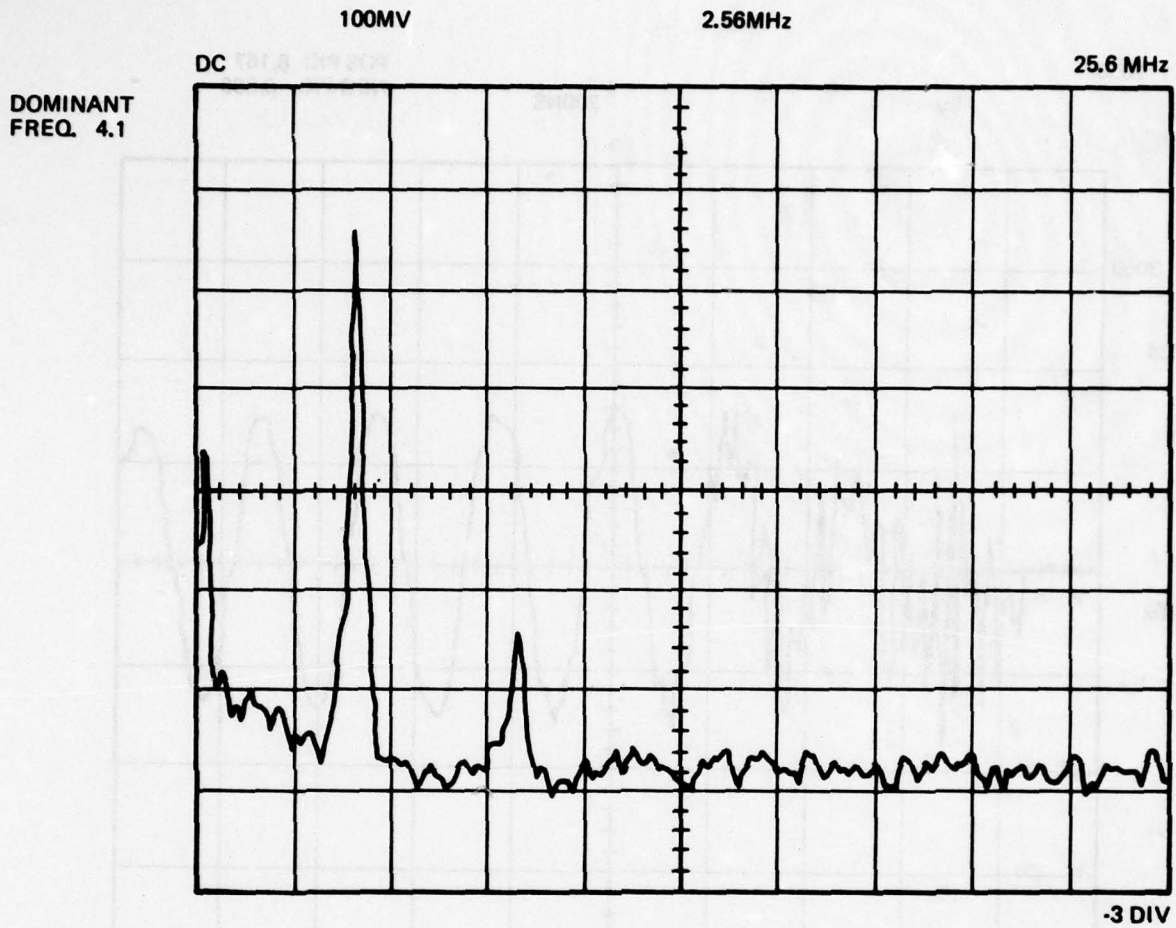
Figure 105.   Spectral Content of Loop Measurements
Made Near Cockpit Aperture

118

POS PK: 4.5
NEG PK: -4.25

2V   200NS

CKT: 0

INPUT ID: 3050

PEAK: 2334

TR: 1.351

TD: 0

DI/DT: 1382
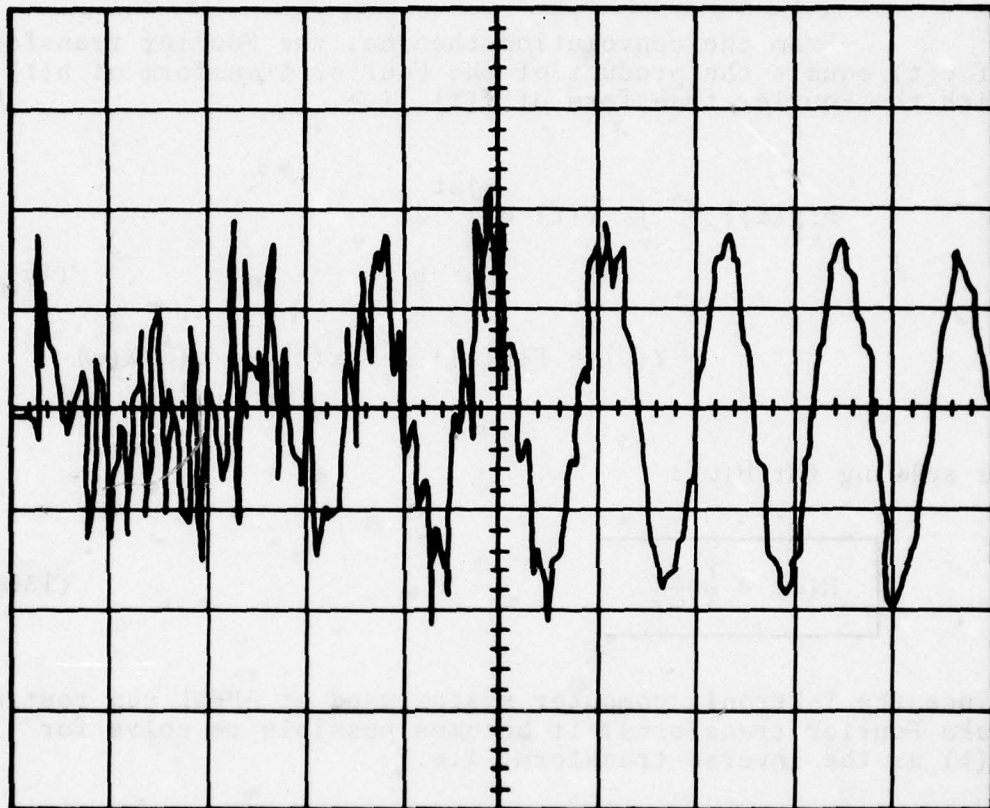
0 DIV

Figure 106. Loop Measurement Near Cockpit Aperture

$$y(t) = \int_0^t h(t - \tau)\, x(\tau)\, d\tau \tag{133}$$

From the recorded input $x(t)$ and output $y(t)$, it is desirable to calculate the impulse response, $h(t)$, in terms of $x(t)$, $y(t)$. Knowledge of $h(t)$ will allow us to predict the system output to any arbitrary input.

From the convolution theorem, the Fourier transform of $y(t)$ equals the product of the Fourier transform of $h(t)$ with the Fourier transform of $x(t)$, i.e.:

$$F\{y(t)\} = \int_{-\infty}^{\infty} y(t)\, e^{-j\omega t}\, dt \tag{134}$$

$$= Y(\omega) = F\{h(t)\} \ X \ F\{x(t)\} = H(\omega)X(\omega)$$

or solving for $H(\omega)$:

$$\boxed{H(\omega) = \frac{Y(\omega)}{X(\omega)}} \tag{135}$$

Since the Tektronix computer system used at AFFDL can routinely take Fourier transforms, it becomes possible to solve for $h(t)$ as the inverse transform, i.e.:

$$h(t) = F^{-1}(H(\omega)) = F^{-1}\left[\frac{Y(\omega)}{X(\omega)}\right] \tag{136}$$

There are two uses for $h(t)$:

a) By convolving $h(t)$ with a *DIFFERENT* $x(t)$, we can compare the calculated output to the measured output provided the input/output points are kept fixed. This provides a powerful test of linearity or superposition.

120

b) Because h(t) represents the physical system response to a narrow spike of energy, the detailed structure spike of h(t) can contain a great deal of information concerning the dynamics of the system. For example, predominantly inductive coupling will be represented by a reflected train of doublet pulses:

$$\left(\frac{d}{d} \delta(t) = \delta^{-1}(t) \right)$$

while capacitive coupling will be represented by a train of triplet functions:

$$\left(\frac{d^2}{dt^2} \delta(t) = \delta^{-2}(t) \right)$$

To illustrate the method by which h(t) is determined, an actual x(t), y(t), was processed by the procedure delineated in equations 136 through 138. The indicated input/output waveform pair is given in Figures 107 and 108. Figures 109 through 112 give the magnitude and phase responses of $X(\omega)$, $Y(\omega)$, respectively. Accordingly, the magnitude and phase of $H(\omega)$ is indicated in Figures 113 and 114. With the inverse transform subroutine, h(t) is easily determined as shown in Figure 115.

As a check of the accuracy of the procedure, the calculated h(t) is convolved with x(t) to give Figure 116 which is virtually identical to Figure 108 as it must be from the convolution theorem. Because the argument is circular, however, the result does not prove linearity but it does verify that S/N and round-off error are not serious problems in the calculated h(t).

5.6 Estimating the Relative Magnitudes of Capacitive and Inductive Coupling Using the Measured Phase Response of the LTA Transfer Function

5.6.1 General Discussion

The frequency technique described in this section uses the phase response of the voltage transfer function to determine the physical nature of the aperture coupling. It represents an interesting use of the principles discussed in Section 1.2 of this report.

121
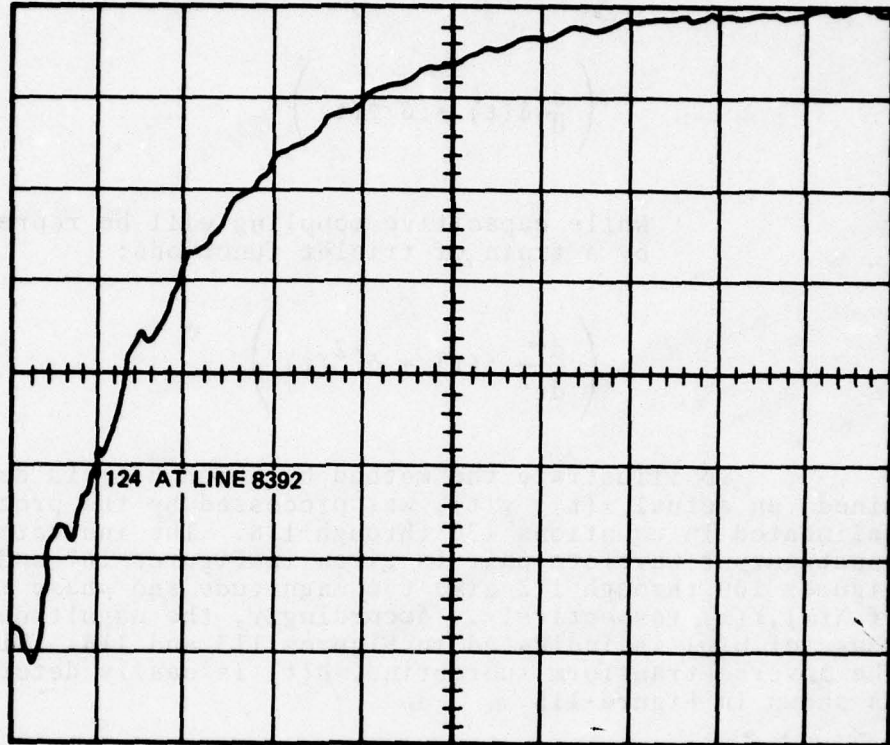
Figure 107. Input Waveform, x(t)

FILE: F111 1118

50MV

500MHz

POS PK: .137
NEG PK: -.1987

CKT: 4

INPUT ID: 3118

PEAK: 733.7

TR: 2.73

TD: 50

DI/DT: 211.5
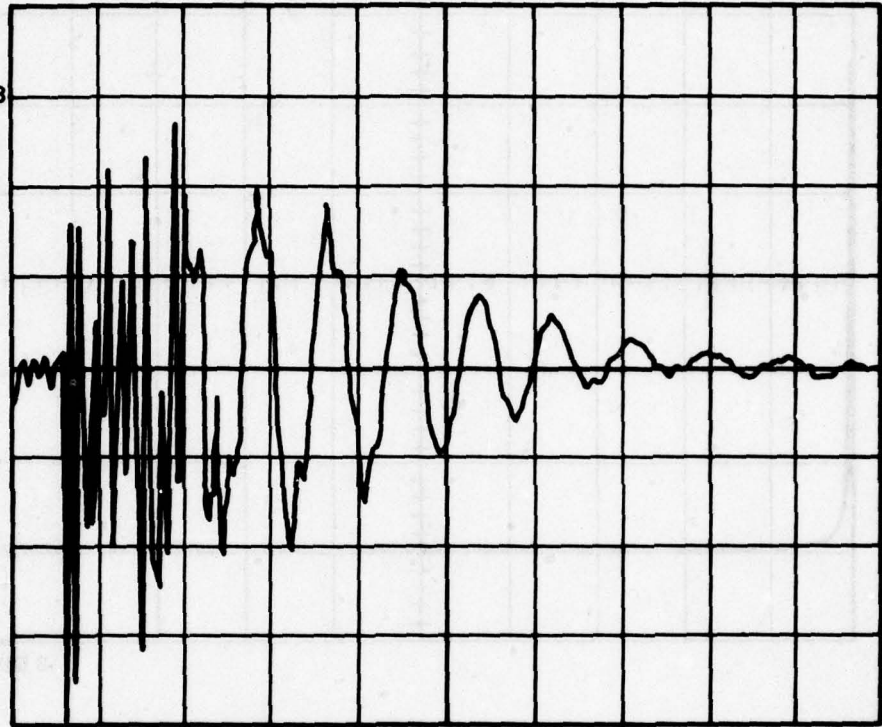
0 DIV

Figure 108.   Output Waveform, y(t)

123

Figure 109. Observed $|X(\omega)|$

124
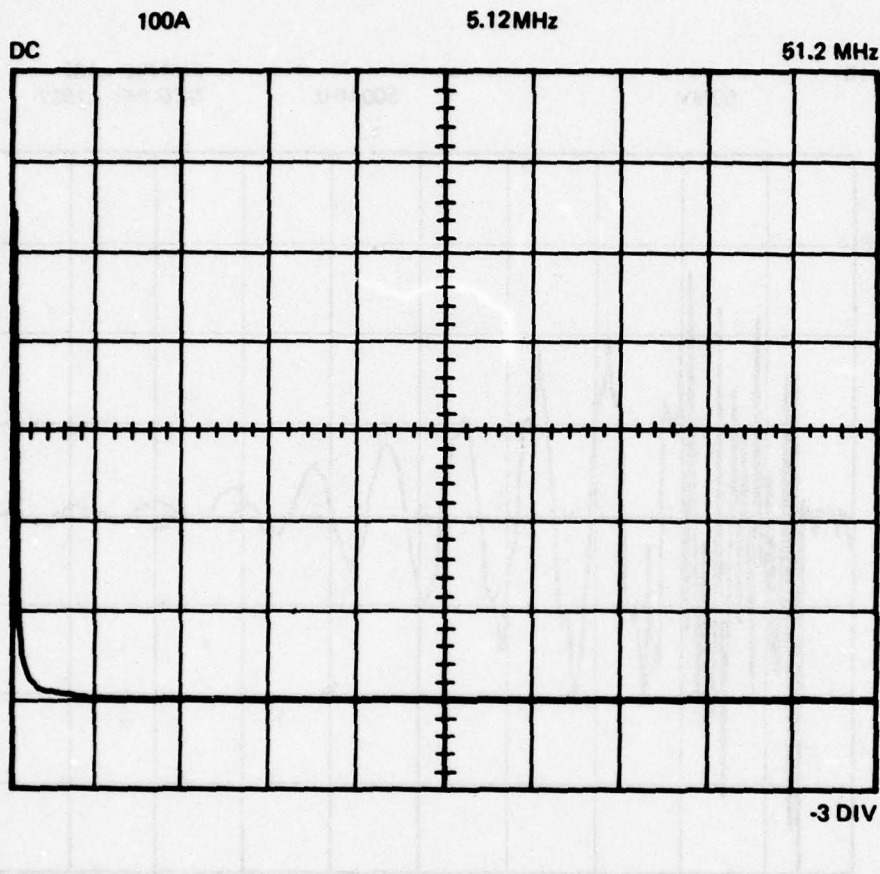
Figure 110. Phase of X(ω)

125

FILE: F111 1118

DOMINANT
FREQ: 2.4
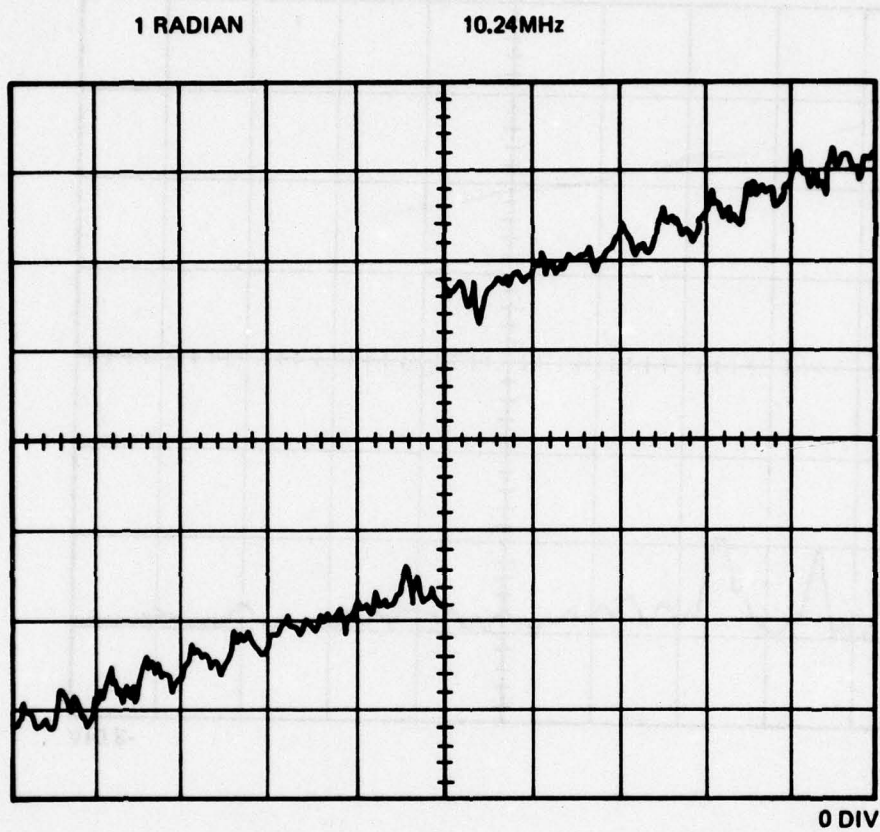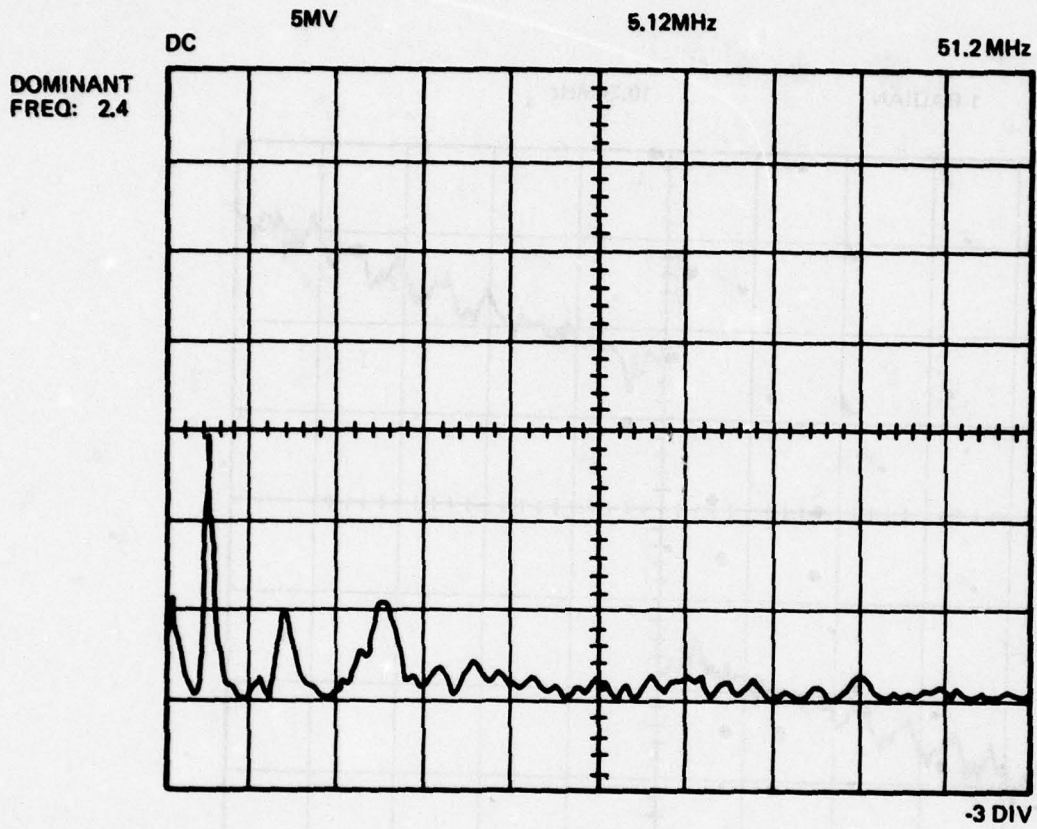
Figure 111. Observed $|Y(\omega)|$

126

50RADIANS   10.24MHz

0 DIV

Figure 112.   Phase of $Y(\omega)$

127
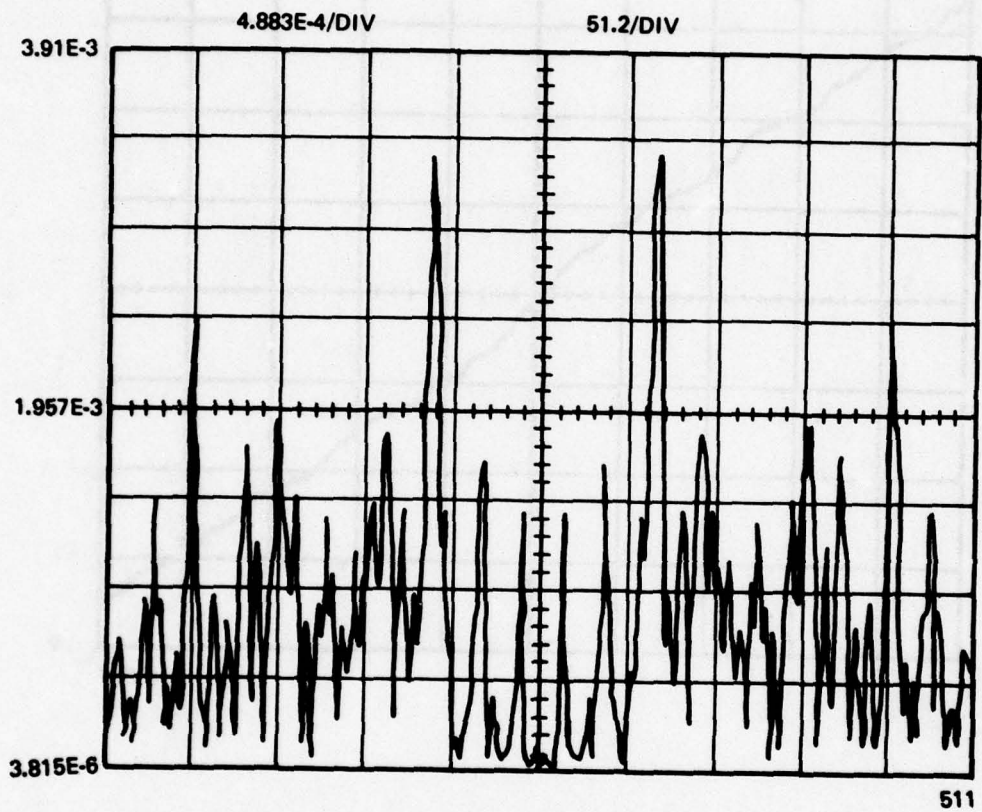
Figure 113. Observed $\left|\dfrac{Y(\omega)}{X(\omega)}\right|$

50RADIANS   1Hz
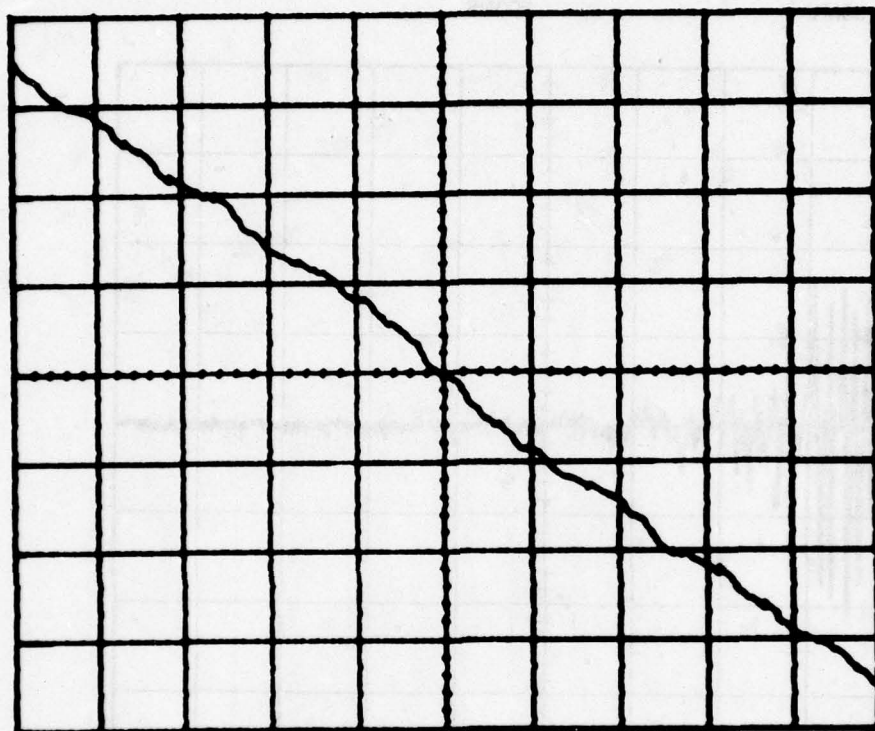
0 DIV

Figure 114. Phase of $Y(\omega)/X(\omega)$

129
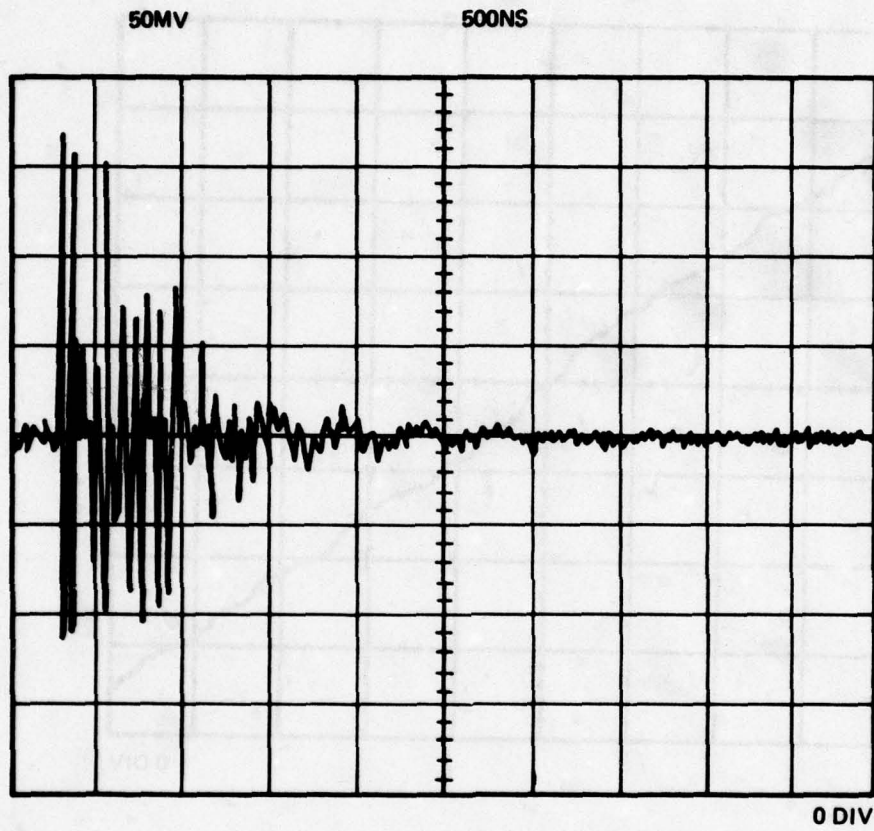
Figure 115. Impulse Response, h(t)

130

500MA   500NS

0 DIV
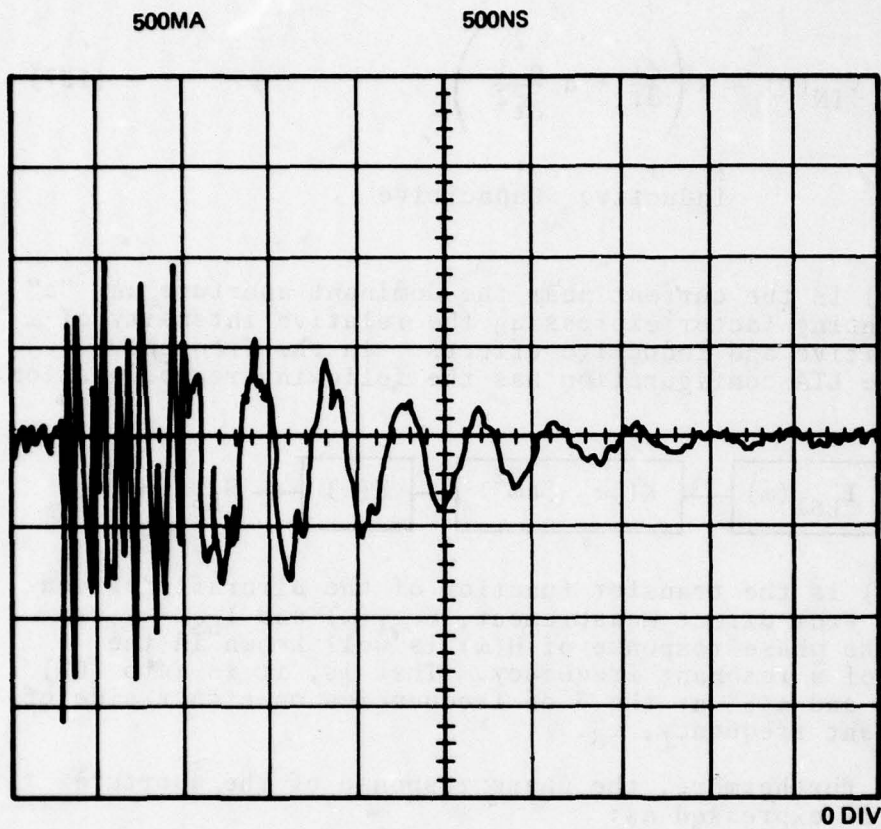
Figure 116.   Generated Output Front X(t)*h(t)

131

5.6.2   Detailed Discussion

In general, the aperture-induced waveform can be expressed as:

$$v_{IN}(t) = K\left(\frac{di}{dt} + a\,\frac{d^2 i}{dt^2}\right) \qquad (137)$$

$$\underset{\text{Inductive}}{\uparrow} \quad \underset{\text{Capacitive}}{\uparrow}$$

where $i(t)$ is the current near the dominant aperture and "a" is a weighting factor expressing the relative intensity of the capacitive and inductive effects. In the frequency domain the LTA configuration has the following representation:

$$\boxed{I_{LST}(\omega)} - \boxed{K(j\omega - a\omega^2)} - \boxed{H(\omega)} - S_{LST}(\omega)$$
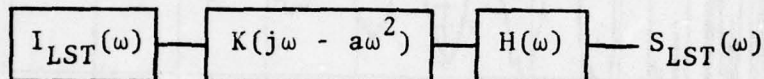
where $H(\omega)$ is the transfer function of the aircraft derived earlier. From direct measurement, $S_{LST}(\omega)$ and $I_{LST}(\omega)$ are known. The phase response of $H(\omega)$ is well known in the vicinity of a resonant frequency. That is, it is zero (0°) at $\omega = \omega_R$ and ±45° at the 3 db frequencies on either side of the resonant frequency, ω_R.

Furthermore, the phase response of the aperture term can be expressed as:

$$\theta_A(\omega) = \tan^{-1}\left[\frac{-1}{a\omega}\right] \qquad (138)$$

so that a knowledge of $\theta_A(\omega)$ should define the weighting factor "a" which is the parameter of interest.

For the following case:

$\theta_{LST}^{I}(\omega)$ - phase of LST current

$\theta_H(\omega)$ - phase of cable transfer function

$\theta_{LST}^{S}(\omega)$ - phase of LST output pulse,

132

we can write:

$$\theta_{LST}^{I}(\omega) + \theta_{A}(\omega) + \theta_{H}(\omega) = \theta_{LST}^{S}(\omega) \tag{139}$$

or:

$$\theta_{A}(\omega) \approx \tan^{-1}\left[\frac{-1}{a\omega}\right] \approx \theta_{LST}^{S}(\omega) - \theta_{H}(\omega) - \theta_{LST}^{I}(\omega) \tag{140}$$

which allows an estimate of the parameter "a".

Although the above procedure has been tried with encouraging results, more work needs to be done with the technique to fully develop it.

133

6. DISCUSSION OF TEST RESULTS AND CONCLUSIONS

6.1 Linearity and Its Implications

The results of the analysis and the experimental veri-
fication have demonstrated the validity of the LSA technique
using LST methods as the single, most valuable tool a de-
signer has for evaluating the susceptibility/vulnerability
of aircraft to lightning events.

It was demonstrated that the inherent linearity assump-
tion is valid and justified. Although this validation is
important, a possibly more important result is the develop-
ment of a method to isolate test configuration effects from
the test results. Although linearity has been conceded by
some LST critics, the difficulties of isolating the test
system from the tested system were of legitimate concern.
The linear systems approach taken and the transfer functions
defined during this investigation permit compensations to be
made for test system configurational effects.

Using test data collected during a normal ground-based
LST the methods for describing the unique transfer function
for each circuit have been developed and demonstrated. The
transfer function defined can be made independent of test
configuration effects. For each circuit it is this transfer
function which is carried aloft by the aircraft when it
flies. This function is readily computed for every aircraft
circuit on which measurements have been made or can be made.
These transfer functions, unique to each circuit, character-
ize the way in which the circuit will respond to any stimulus.
The ability to measure these functions is of extreme impor-
tance because it now makes possible the exact calculation of
any circuit's response to natural lightning. This calcula-
tion would include not only the maximum magnitude of the
transient but the precise time history of the induced tran-
sient. The calculation, of course, depends upon more detailed
knowledge of the airborne natural lightning environment than
is currently available. The AFFDL EM Hazards Group at
Wright-Patterson AFB has been and continues to be involved
in research projects aimed at measuring the airborne light-
ning parameters. With the present LST methods, the response
functions can be measured and with natural environmental
data, all past and present aircraft systems can be evaluated.
Newly designed systems could be mocked-up, for example, in
the iron-bird state, and flight-critical circuits could be
evaluated before design freeze or at least soon enough to
impact design trade-offs.

Some other interesting points were covered during this
investigation of F-111 aircraft and its yaw computer circuit

which was studied in detail. After the impulse response
function, Figure 117, was obtained, it was decided to examine
the properties of the output waveform which would be pro-
duced by a variety of input waveforms. Much criticism has
been made about the fact that laboratory test waveforms rise
in a convex fashion, whereas natural lightning probably
rises in a concave fashion (Figures 118 and 119). Accord-
ingly, a waveform which rises in a concave manner was con-
structed mathematically (Figure 119). It should be noted
that this waveform is abstract and not related in any way to
any physically real system or to the natural environment.
It is simply one of many possible waveforms which, if they
were physically realizable, could be passed through an air-
frame and would produce some output. This waveform was se-
lected based upon two arbitrary criteria: it rises in a
concave manner and it is rather significantly different in
its time domain appearance from the actual LST input wave-
form used to obtain the Input Response Function (IRF) shown.
Figure 118 shows a measured LST input and Figure 120 shows
the measured output created by the input. Figure 119 shows
the artificial input and Figure 121 shows the output which
would occur. Note that significant variations in time do-
main input waveforms do not result in drastic variations
in the output waveforms caused by those inputs. As is evi-
dent, any electrical circuit will respond only at discrete
frequencies or over discrete frequency bands. If the input
waveform (to the aircraft) contains those frequencies and
if an aperture allows them to enter the aircraft (independent
of whether entry is through electric or magnetic coupling)
then the circuit will respond accordingly. Conversely, if
the frequencies are not present in the input then the cir-
cuit will not respond (there will be no output). This
seemingly trivial exercise is presented to highlight a more
subtle fact: Over a wide range of test conditions, the same
output will be obtained. Thus a 2 x 50 µsec input current
pulse will yield results which probably will not significant-
ly differ from 1.5 x 50 or 3 x 50 µsec input current pulser
or whatever is used. Facilities effects may or may not be
important in what output is measured but techniques developed
and reported here permit the removal of these effects from
the test results.

    Having demonstrated the means by which the ground
facility configuration effects of LST can be eliminated in
LTA, that the aircraft and its subsystems' transfer functions
can be accurately defined by LST, and that LTA is inherently
linear if performed as described in this document, it remains
only to define, in both the time and frequency domains, the
actual lightning threat of the real environment. This is
easier said than done since, in all probability, lightning
strokes are like snowflakes, in that no two are ever exactly
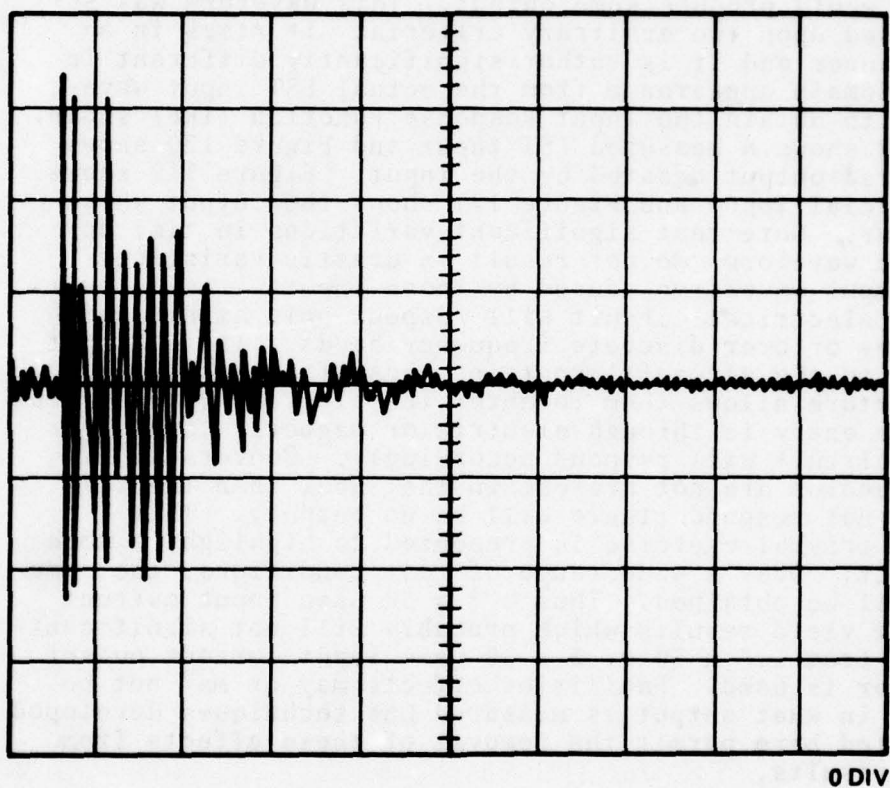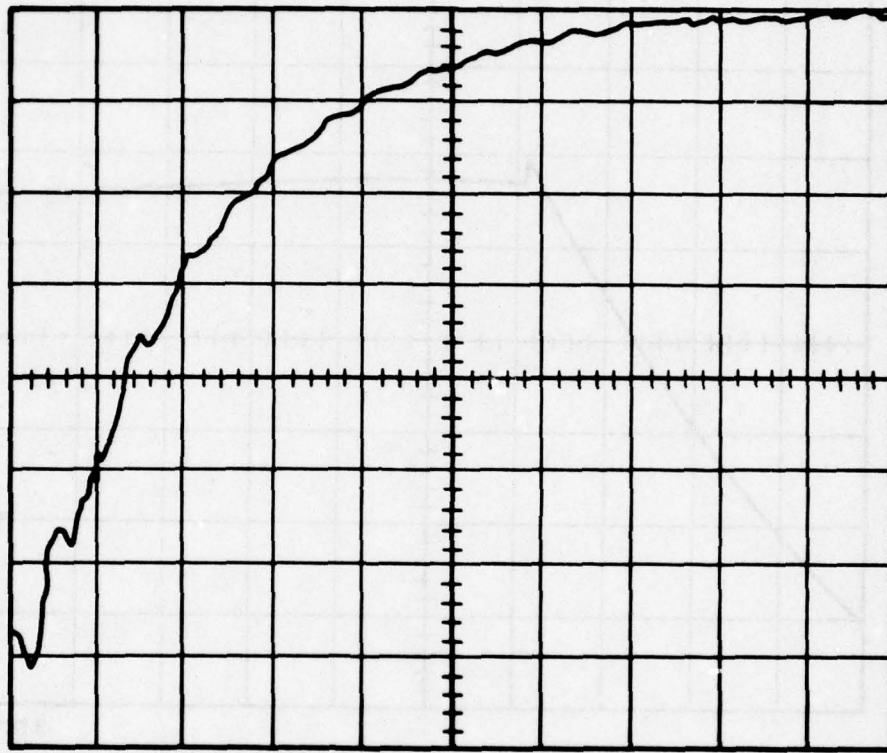alike. Therefore, the preparation of test standards (e.g.,

0 DIV

Figure 117.   Impulse Response Function for F-111
Aircraft Yaw Computer

FILE: FIl I 3109

-3 DIV

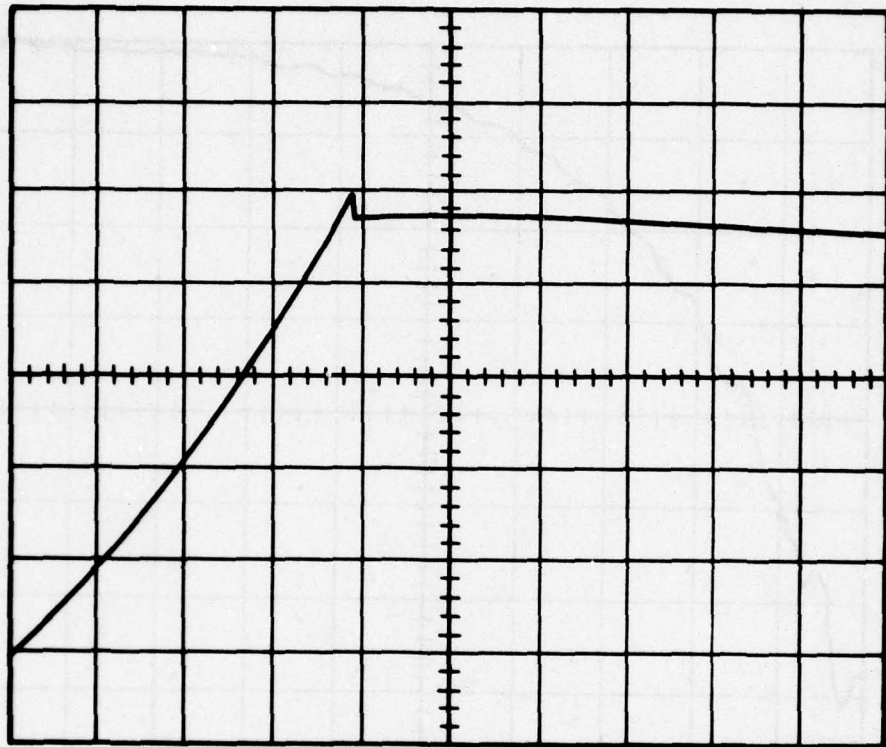Figure 118. Actual Measured Waveform with Convex Front

137

Figure 119.   Waveform with Concave Front
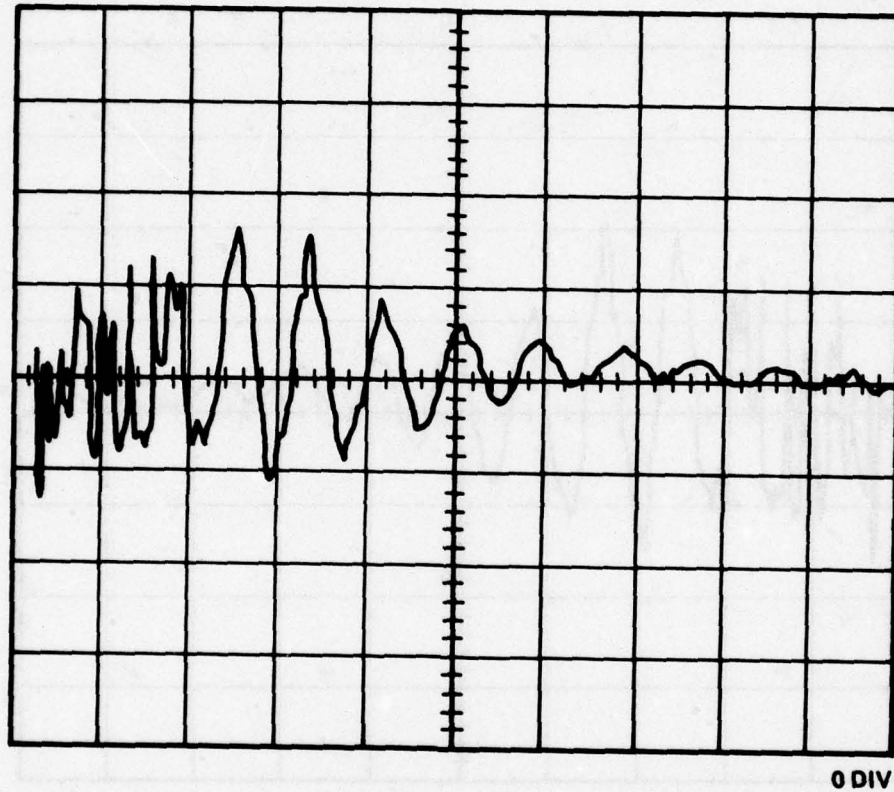
0 DIV

Figure 120.   Measured Output on F-111 Aircraft Yaw
Computer Circuit

139
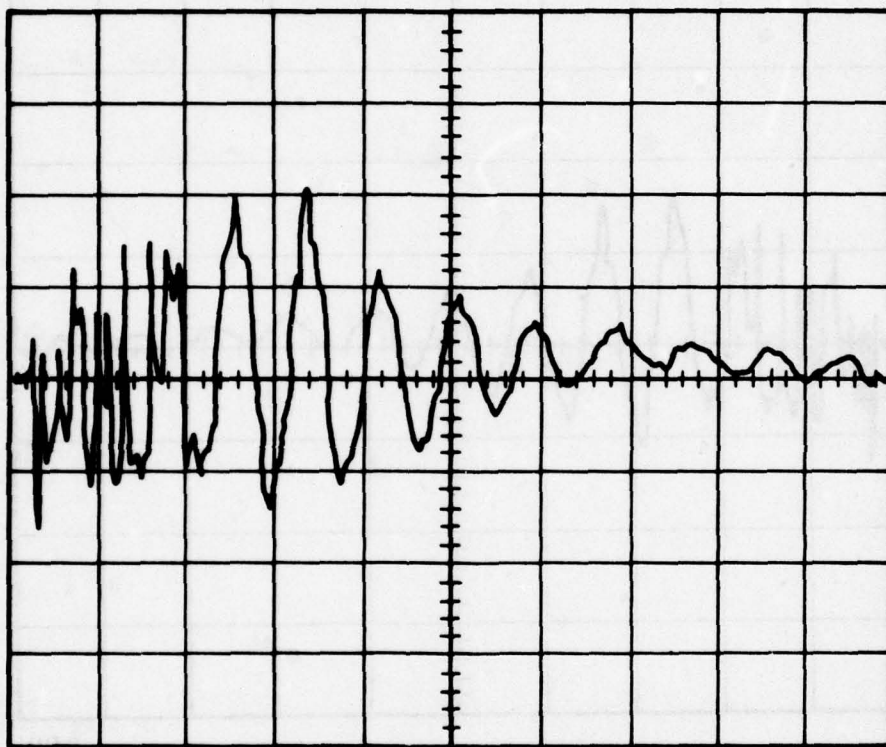
0 DIV

Figure 121. Predicted Output with Concave Input

140

pulse amplitudes and rise and decay times) for LST must not
concentrate on a single waveform. Certainly, at least until
sufficient actual lightning data is collected and analyzed,
a wide variety of LST stimulus waveforms should be used in
performing LST on actual aircraft/systems. Testing which in-
cludes (slowly) swept oscillator tests in which both ampli-
tude and phase characteristics of the input/output waveform
pair are recorded is an acceptable alternative. Also note
that although LST methods were originally intended to provide
a simulation of di/dt effects (magnetic fields), a dv/dt ef-
fect (electric fields) has been fortuitously included. In
this report we have demonstrated the potential for the mea-
surement of the dominant coupling mode (electric or magnetic
field). In addition, the capability exists for calculating
the location of the aperture through which the energy coupled.

6.2 TEM Shorted Transmission Line Representation

The verification that the LST system, the aircraft and
the return lines can be represented as a shorted transmission
line propagating energy in the TEM mode is important. Internal
shielding of cables, or black-boxes, and the fields inside
cavities can easily be mapped using simple resistance paper
(Teledeltos) techniques. This data can provide important
information to improve cable routing or shielding strategies.

6.3 Coupling Phenomena

The relationship and relative importance of the known
coupling mechanism's electric and magnetic fields can be cal-
culated. Only a few such calculations have actually been
performed so far and will be reported when time permits a
more comprehensive study of F-111 test data. This data will
stimulate further development in LST methods and is another
reason why limiting the development of LST standardized
current waveforms is thought to be premature. Another impor-
tant fact determined from this investigation relative to
coupling is the estimate of the length of cable which was
required to achieve the magnitudes of measured transients.
Although this study (in Section 3.4) did not include a de-
tailed evaluation on the induced voltage levels on aircraft
cabling resulting from aperture coupling, the analysis did
show that aperture coupling does not require unrealistic
lengths (9 cm in the example) of exposed cable to result in
significant induced voltages.

6.4 Systems Considerations

From a systems point of view previous methods of LST
indirect effects evaluation were incomplete. The necessity
for both time and frequency domain treatments results in a
need to include a data acquisition system with some "number

141

crunching" capability to provide accurate and thorough analyses to be accomplished. Low noise measurements with inherently high signal-to-noise ratios will also enhance the usefulness of the data and will ease data reduction problems. A representative LST system should include most of the capabilities outlined in the Appendix of this report. And, although it is premature to actually develop definitive specifications, pending resolution of in-flight environmental parameters, the basic framework of LTA methodology can be sketched. The AFFDL EM Hazards Group plans to do this in the near future.

6.5 Design Trade-offs

The methods developed permit a sensitivity analysis to be performed on aircraft by changing a) the aircraft itself, b) the circuit, c) the shielding of the cables, d) the dielectric insulation of the cables, or e) the surge suppression device. The sensitivity analysis will provide the required feedback necessary to ensure that design trade-offs can be made based on realistic data, not on judgement alone. In addition, these trade-off studies can be made early in the design.

6.6 Conclusions

The results of this investigation demonstrated that the LTA method with time and frequency domain inputs resulting from LST can accurately predict the susceptibility/vulnerability of aircraft to lightning.

The results also demonstrated that LST outputs are linearly proportional to the inputs, and, as a consequence, can be scaled to real lightning levels.

The method described enables the elimination of facility effects regardless of their magnitude.

The LST system and aircraft can be represented as a shorted transmission line operating in the TEM mode. From this TEM representation both external and internal magnetic and electric fields can be found by solving Laplace's equation through the resistance paper method.

The natural environment must be characterized in more detail so that an exact prediction of aircraft circuit responses can be calculated for any aircraft and circuit on which an LST is performed. At present this detailed characterization is not available. The data needed, although not required to validate LTA methods, should be accumulated to permit the application of these validated techniques to real aircraft flying into real lightning environments.

The location of the dominant aperture can be calculated if only one such aperture is the source. For multiple apertures it is probable that the existing methods can be extended to locate each.

The coupling mode, electric field or magnetic field can be calculated from the phase relationships between the input/output waveform and the impulse response function. Both coupling fields must be considered in any system study or evaluation.

The framework of LST standards can be established although complete LST standardization must await further development of present LST methods and definition of the natural environment.

143

7. RECOMMENDATIONS

The following list of recommendations, although not exhaustive, includes some such representative areas where further investigation is in order. In general, the recommendations consist of performing additional investigations in: LTA configuration effects, small apertures, pulse response of aircraft cabling, aircraft system considerations, standards for LST methods, acquisition of in-flight data, and reprocessing existing data from previous tests.

7.1 LTA Configuration Effects

a. Investigate the variation of skin current density as a function of lightning entry and exit points. The relationship between the LTA skin current density and the airborne lightning strike is one of the major open questions in the LTA problem. (It is expected that 2-dimensional potential solutions will be the preferred approaches.)

b. Analyze the effect of the LST grounding configurations on the skin current distribution. Measure the higher-mode skin current behavior near important apertures.

7.2 Small Aperture Studies

a. With the "yoke" coil experiment, quantify $\vec{E}$ and $\vec{H}$ values inside typical fuselage cavities as a means of verifying Van Bladel's expressions.

b. Evaluate the near field $\vec{E}$ and $\vec{H}$ scalar potentials as suggested in 3.2.2.1.

c. Consider a three-dimensional numerical study of the effects of aircraft cavity shielding on the expected $\vec{E}$ and $\vec{H}$ field levels.

d. Undertake a detailed measurement program to determine the shielding effects of conductive supports, panels, wire bundles, etc. These test results should then be correlated with the resistance paper method, the conjugate harmonic method, and the graphical method.

e. Develop a cable routing strategy using potential theory techniques.

144

7.3 **Pulse Response of Aircraft Cabling**

a. Perform a detailed series of experimental tests to compare the results predicted from linear system theory to actual LTA test results. The tests should include a wide range of aircraft circuits.

b. Develop the use of the phase response of the transfer function to predict the nature of the aperture coupling. The results should be compared to the estimates derived from "small aperture" theory.

c. Develop input waveform independent methods for determining the application point (ℓ_1, ℓ_2) of the dominant aperture flux. The frequency domain techniques will involve the interrelationship between transfer function magnitude and phase near the (ℓ_1, ℓ_2) dependent resonant frequencies.

d. Develop time and frequency domain techniques to identify the multiple input (aperture) case.

e. Analyze the possible effects of a distributed rather than a local excitation point.

f. Extend pulse response techniques to other kinds of terminating impedances, nonlinearities, and cable lengths.

g. Extend present work on unshielded cable to shielded coaxial cable.

7.4 **System Considerations**

a. The overall LTA impulse response, $h(t)$, (3.3.2.1) technique holds great promise, both as a means for predicting system outputs to new inputs and also as a means of identifying the dominant physical processes present in the LTA system. New input/output pairs should be analyzed. Also, the entrance-exit points of the LTA current pulse should be varied. The resulting change in $h(t)$ should reveal significant information about the LTA system.

b. The new amplitude scaling technique, involving the intermediate convolution state, should be programmed. The programming should be quite routine on the versatile AFFDL EM Hazards Group Tektronix computer. Given an input (damped exponential) output pair, the scaling can be done for all the frequencies of actual lightning waveforms.

145

c. The phase response method for identifying the nature of the "small aperture" coupling should be extended. Other frequency and time domain methods should be developed to quantify the aperture transfer function, $G_{AP}(\omega)$, which was presented in Figure 3.

7.5 Standards

The framework for standard LST methods should be established (possibly as a position paper). Such a framework would outline the general requirements for the measurement equipment, the data collection techniques and the methods of data reduction. In addition, methods for "spec-ing" equipment should be possible. For example, definitions of acceptable transfer functions might be one way to approach these specifications.

7.6 Supporting Data

Independent of the method(s) selected for the "on the ground" analysis of an aircraft (by test, computer model, or both), it is imperative that in-flight data be obtained. Without the detailed knowledge of the actual lightning environment to which aircraft and their systems are subjected, it is ludicrous to affirm that the results of LTA can become the basis of design standards. The methods are sound but definition of the input is incomplete. It can be stated that the aircraft (or system) will respond in a specific manner to a given input. However, this is not the same as saying that the aircraft/system will respond in a specific manner to an actual lightning stroke. It is evident now that for lightning our test methods have, in some cases, been developed and used before it was clear what effect was being tested for or why. Fortunately, the methods developed are fundamentally sound and coupled with the techniques presented here will yield the desired data.

7.7 Old Test Data

Once all of the other refinements to LST methodology have been made, all of the old LST test data (particularly F-16, and the F-8, F-4 (fly-by-wire tests)) should be reprocessed by the techniques presented here. The need for this review of "old" data is to determine if the transfer functions for generic types of equipment are similar. If the similarities are sufficiently close, then data collected for one system would apply to another. Protection successfully used on one system could be used on another system. This presents the potential for more standard installation procedures. Reduction of the number of different parts in the inventory would follow as a consequence.

146

REFERENCES

1. Air Force Lightning Incident Reports Compiled by Norton Air Force Base.

2. Lear Jet Flight Test Program for In-Flight Measurement of the Natural Electrical Environment (TRIP-77), Joint NASA/AFFDL program.

3. "Aerospace Recommended Practice; Lightning Effects Tests on Aerospace Vehicles and Hardware" by SAE Committee AE4, Special Task F.

4. MIL-B-5087B, "Bonding, Electrical, and Lightning Protection for Aerospace Systems."

5. Lloyd, K.J., Walko, L.C., and Plumer, J.A., "Measurement and Analysis of Lightning-Induced Voltages in Aircraft Electrical Circuits," NASA CR-1744, February 1971.

6. Burrows, B.J.C., "Induced Voltage in Full-Size Aircraft at 10^{11} Amp/Sec," IEEE EMC Conference, Seattle, Washington, August 1977.

7. Apollo-Soyuz Test Plan, NASA, 1976.

8. Maxwell, K.J., Unpublished Work for General Electric Company, 1976.

9. Butters, W.G., "Lightning-Induced Electrical Transients on Aircraft Wiring," McDonnell Douglas Corp. Report No. MDC A4555, January 1977.

10. Walko, L.C., and Mangold, V.L., "Lightning Transient Research on an F-111E Aircraft," AFFDL-TM-77-XXX, September 1977.

11. Van Bladel, J., and DeMeulenaere, F., "Polarizability of Some Small Apertures," IEEE Transactions on Antennas and Propagation, Volume AP 25 No. 2, pg. 198, March 1977.

12. Vitrovitch, D. (Ed.), "Field Analysis: Experimental and Computational Methods," Von Nostrand, 1966.

13. Walko, L.C., "A Test Technique for Measuring Lightning-Induced Voltages on Aircraft Electrical Circuits," NASA CR-2348, February 1974.

14. Jordan and Balmon, "Electromagnetic Waves and Radiating Systems," Prentice Hall, 1968.

REFERENCES (Concluded)

15. Natick, "Transmission Lines for Digital and Communi-
     cation Networks," McGraw Hill, 1969.

16. Schelkunoff, S.A., "Some Equivalence Theorems of
     Electromagnetics and Their Application to Radiation
     Problems," Bell System Technical Journal, Volume 15,
     pp. 92-112, January 1936.

BIBLIOGRAPHY

1.   McCormick, W.S., Ph.D., "Aperture Coupling and Related
     Problems", Internal Memo, 29 June 1977.

2.   McCormick, W.S., Ph.D., "Some Remarks on the LTA Waveforms",
     Internal Memo, 15 April 1977.

3.   McCormick, W.S., Ph.D., "Procedure for Isolating LTA
     Configuration Effects", Internal Memo, 2 May 1977.

4.   McCormick, W.S., Ph.D., "A Possible Model for the LTA
     Configuration", Internal Memo, 9 June 1977.

5.   McCormick, W.S., Ph.D., "Time Domain Analysis of LTA
     Configuration Plus Initial Results on Transmission
     Line Pulse Response", Internal Memo, 25 July 1977.

6.   McCormick, W.S., Ph.D., "Experimental Confirmation of
     the LTA TEM Assumption and Additional Results on
     Aperture Coupling", Internal Memo, 17 August 1977.

7.   McCormick, W.S., Ph.D., "Experimental Design for Aperture
     Coupling Experiments", Internal Memo, 7 July 1977.

8.   McCormick, W.S., Ph.D., "Distributed Presentation Notes
     Including Various Analytical Results as well as a Pre-
     sentation of Actual F-111 Time Domain and Frequency Domain
     Test Results", Internal Memo, 9 September 1977.

9.   McCormick, W.S., Ph.D., "Some More Results from Linear
     System Theory", Internal Memo, 23 September 1977.

10. McCormick, W.S., Ph.D., "Lightning-Induced Electrical
     Transients on Aircraft Wiring Systems", Internal Memo,
     18 March 1977.

148

APPENDIX I

F-111 Test Program

The F-111 tests were conducted on an Air Force F-111-E aircraft, serial number 67-116A, at Eglin Air Force Base by the Electromagnetic Hazards Group, AFFDL/FESL, during the late summer of 1976. The original objectives of the F-111 LTA program were mainly to improve the technique for obtaining information on the effect of lightning strikes to aircraft and to collect transient data on internal circuitry. Some of the important improvements incorporated in the F-111 tests over previous LTA tests performed in the industry were made to the pulse generating circuits and the measurement system. These improvements, in fact, were prerequisites to permit significant progress in LTA verification.

Pulse Generating Circuit Improvements

1) A pneumatic trigger system was used to initiate current flow from the lightning simulator capacitor bank. This system replaced conventional electronic systems. This trigger eliminates the extraneous trigger noise caused by electronic triggers. In addition, the isolation of the pneumatic trigger eliminates possible ground loops within the test set-up thus improving signal-to-noise ratios.

2) Return leads were set up in a symmetrical fashion about the aircraft to simulate natural current distribution of current in the airframe. Several return leads were used to lower total circuit inductance permitting rapid rates of current rise.

Measurement System Improvements

1) A fiber optics data link was used to transfer the measured transients from the measurement point on the aircraft to a remote data acquisition point (a shielded trailer).

2) Break-out boxes and cable interfaces between the aircraft circuitry and the fiber optics were specifically designed for lightning transient research which minimize alterations of the circuit's response. Again, increased signal-to-noise ratio was a result of this careful design.

3) A Tektronix transient digitizer (Model R7912) was used to acquire the signal transmitted over the fiber optic data-link. This digitizer was connected to a PDP 11/05 computer system to allow the data to be stored on magnetic tape (cassettes) and to permit analyses to be performed in both the time and frequency domains.

149

The use of these methods advanced the state-of-the-art of the LTA technique and improved the usefulness of the data significantly over the first generation LTA techniques. This improvement is directly traceable to the higher signal-to-noise ratios attained and the ease with which frequency domain analyses can be performed.

As a result of the F-111 test, lightning-induced voltages were measured on flight critical circuits of the Altitude-Vertical Speed amplifiers, including the yaw and roll computers, the Roll Rate Gyro Circuit in the Feel and Trim assembly and the servo damper circuits. Power was on for these measurements since there was evidence from previous tests which suggests that higher transients occur with power on than with power off.

The electrical configuration used to simulate a current pulse similar in shape to the unidirectional fast rising current wave of a natural lightning strike has been described previously (Reference 3) and is shown in Figure A-1.

The Lightning Current Generator used for these tests uses two separate capacitor banks, each charged separately. The capacitance, resistance and inductance of the circuit may be varied along with charge voltage to achieve a variety of waveshapes, risetimes, or amplitudes. The banks were triggered by a pneumatic trigger instead of an electronic trigger because trigger noise is reduced and gap spacing is no longer critical thus preventing premature "firing" of the network ("prefire"). Figures A-2 and A-3 show the capacitor bank physical arrangement and Figure A-4 shows the overall LTA set-up with the F-111 in place. Note in Figure A-4 that the return lines are arranged to prevent distortions in current distributions within the airframe. This was verified by skin current measurements.

A typical current pulse generated by this arrangement is shown in Figure A-5. Note that the configurational data is recorded on the margin. This is done for each waveform and updated as the configurations change.

The measurement system and instruments for this test are shown in Figures A-6 through A-8. The data obtained from an LST are usually induced voltages measured on selected circuits within the aircraft. Valid induced voltage measurements on aircraft electrical circuitry require that special consideration be given to not disturbing the system on which the measurement is made. Additionally, signal-to-noise ratios must be maximized. The break-out boxes and fiber optics system resulted from these considerations.

The data acquisition system shown in Figure A-8 also offers a significant improvement over previous techniques. The Tektronix R7912 Transient Digitizer is a high-speed digital converter (500 MHz bandwidth) which can be operated similarly to

an oscilloscope when coupled with a 7A19 vertical amplifier plug-in and a 7B92A horizontal time base plug-in. The PDP 11/05 computer controls the entire system and can perform normal computation routines using either BASIC or FORTRAN programming languages. Data is permanently recorded using the Tektronix 4610 hard copy unit (producing an 8 x 10 report quality print similar to an oscillogram). The data may also be stored on magnetic cassettes.

151
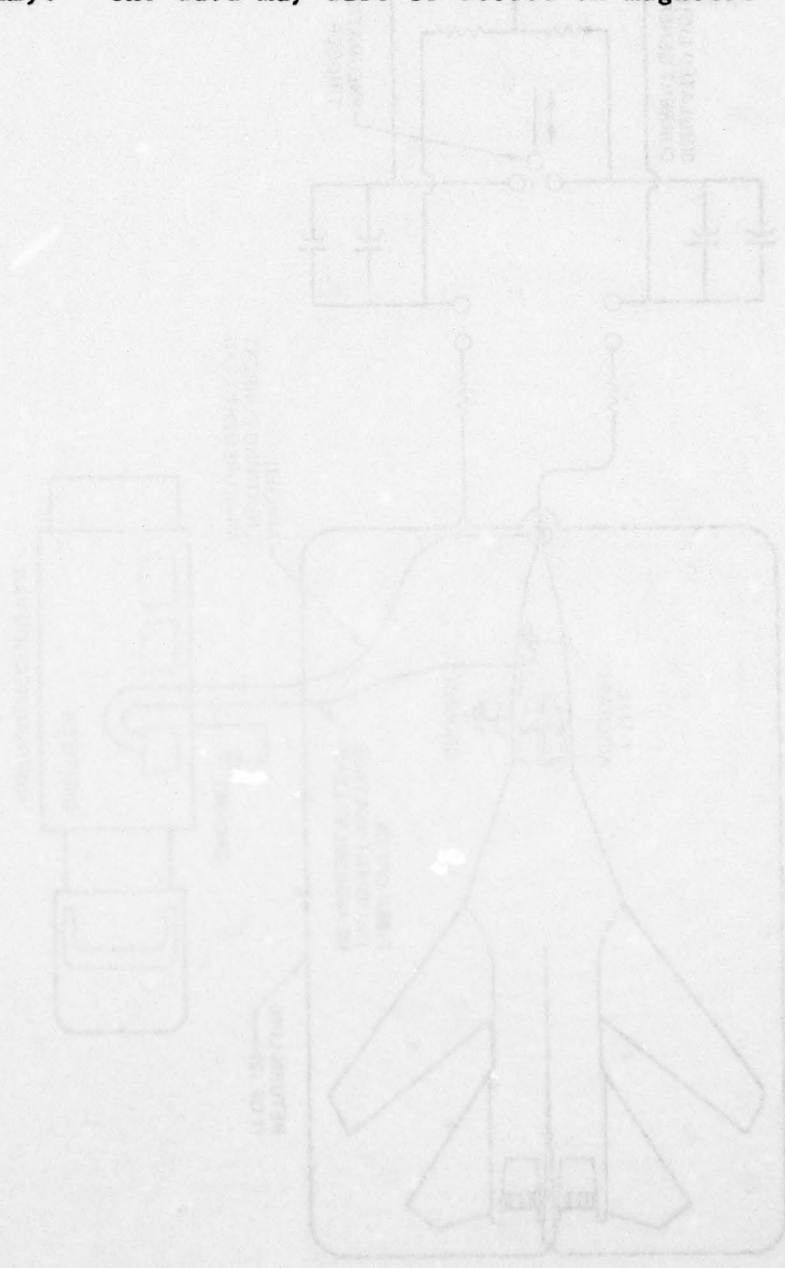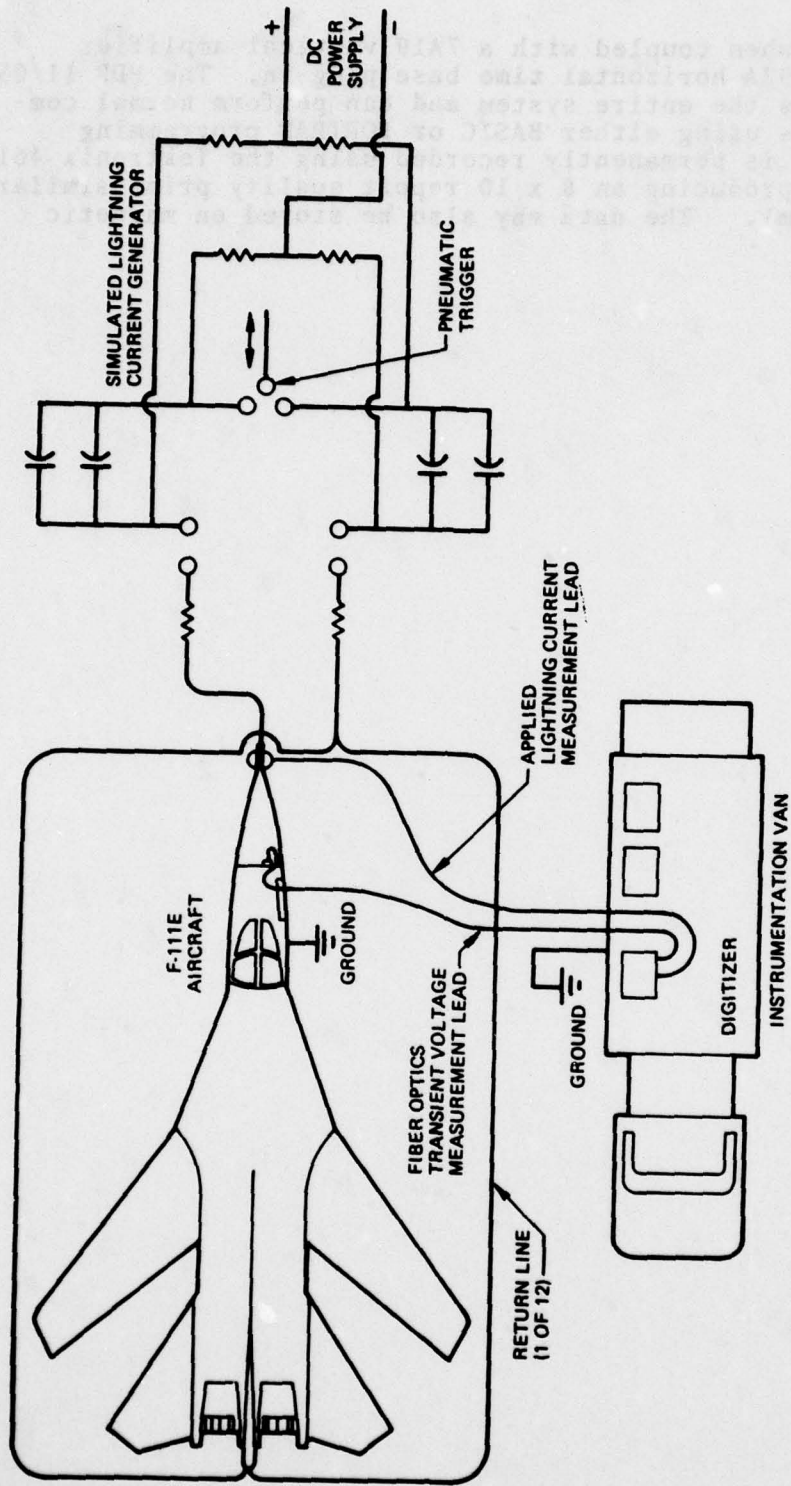
Figure A-1. Plan View of Test Set-Up

152

Figure A-2. Two-Stage Marx-Type Current Impulse Generator
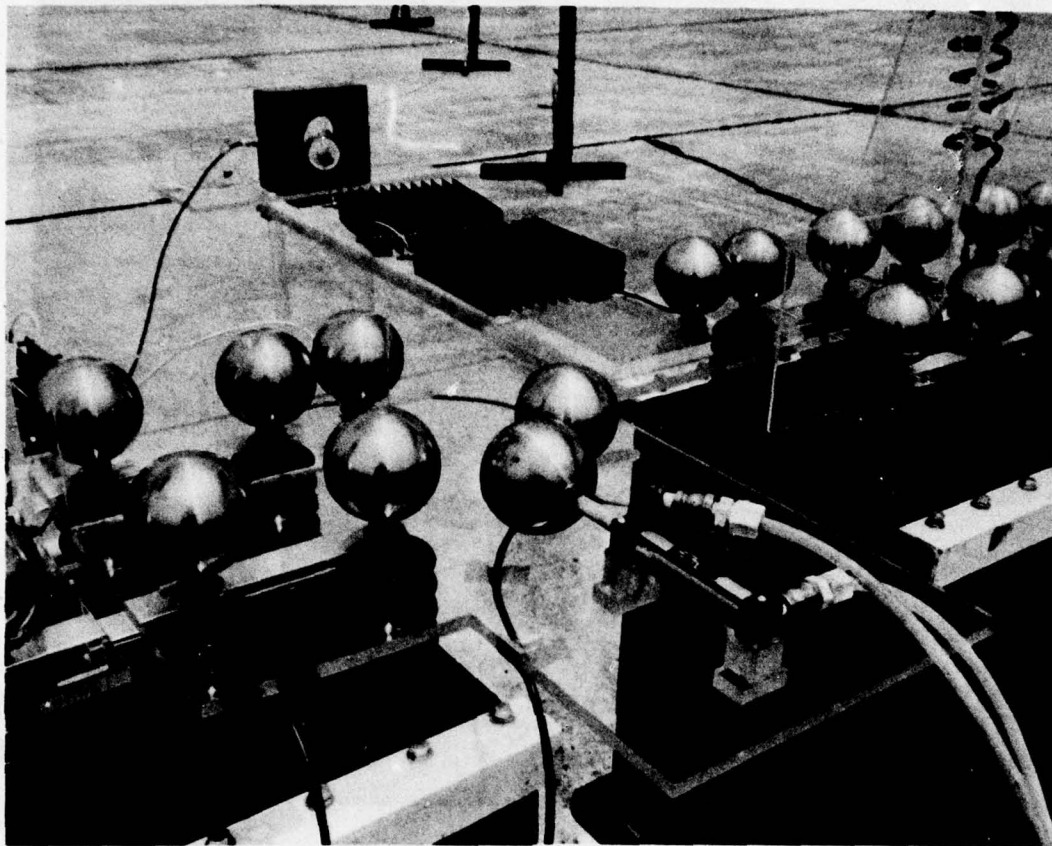
Figure A-3.   Detail of Marx-Type Current Impulse Generator
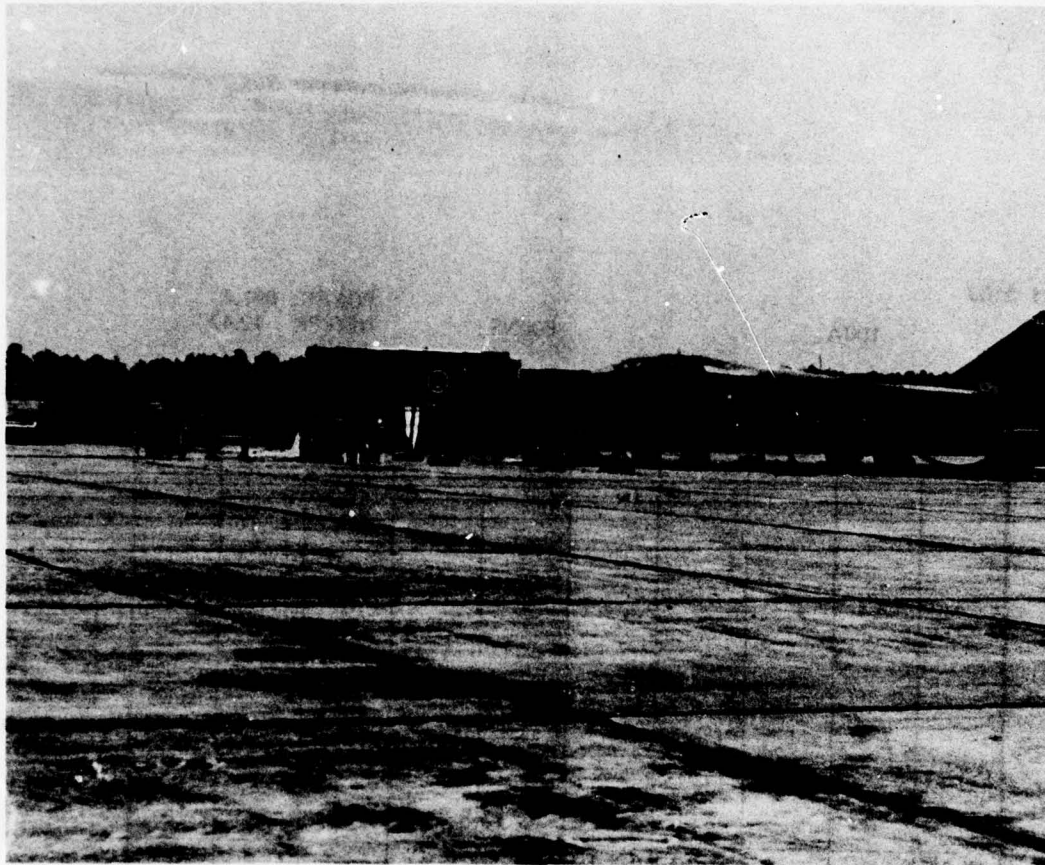
Figure A-4.   F-111E Aircraft and Lightning Transient
             Test Set-Up
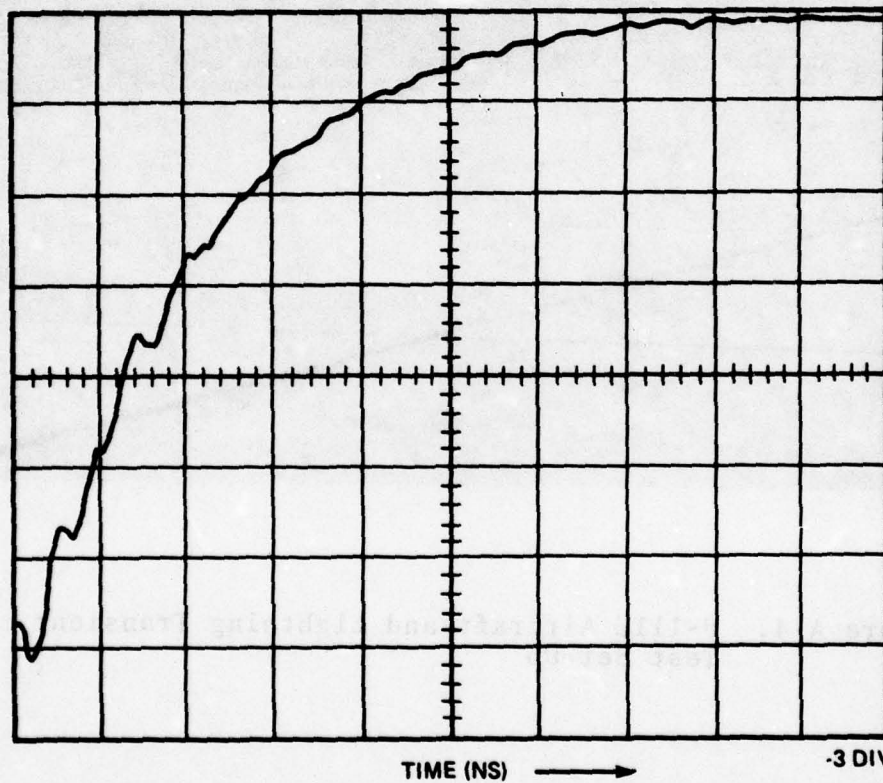
Figure A-5. Typical Current Pulse Generated by
Marx-Type Impulse Generator

156
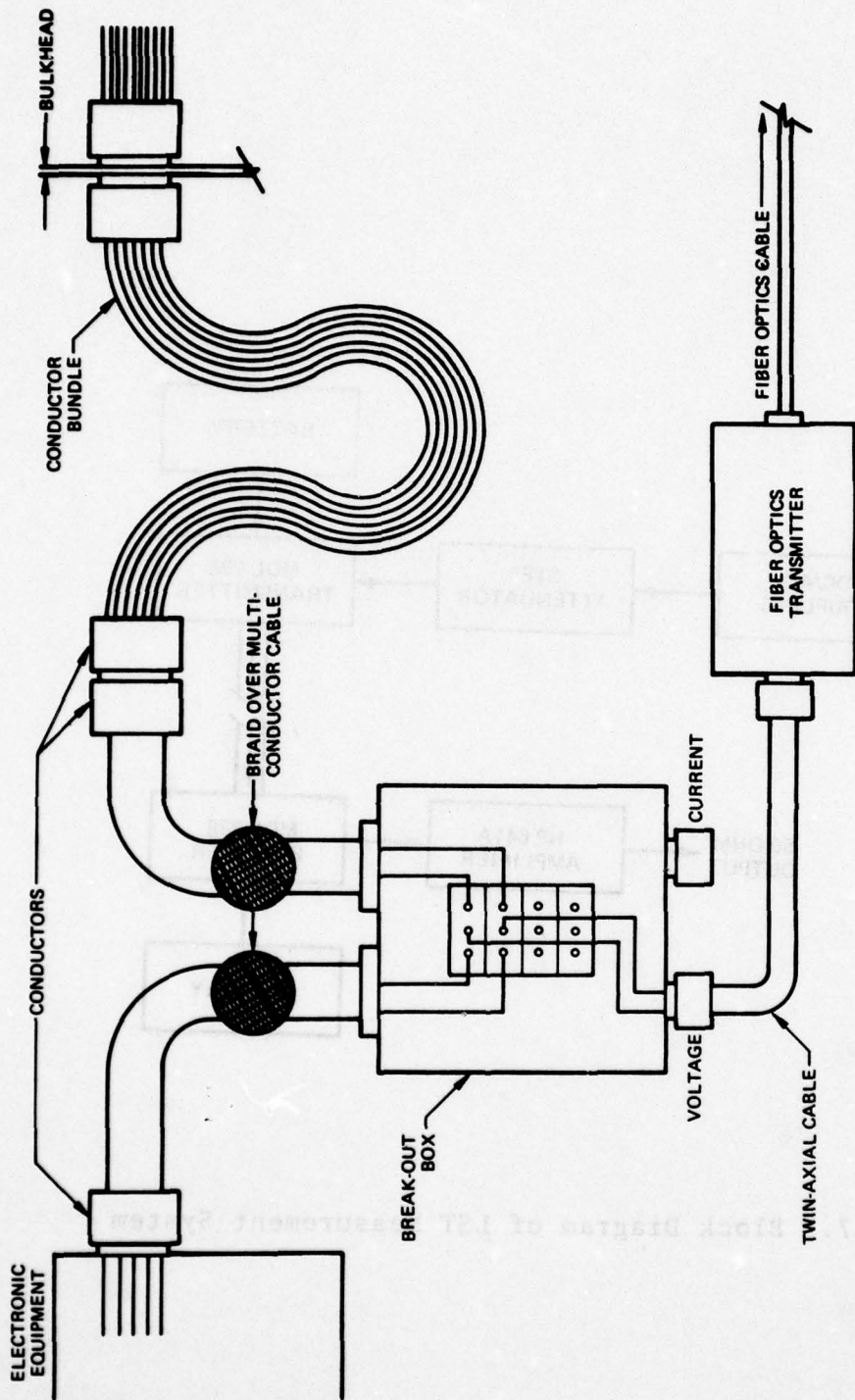
Figure A-6. Detail of Break-Out Box Used for
Induced Transient Measurements
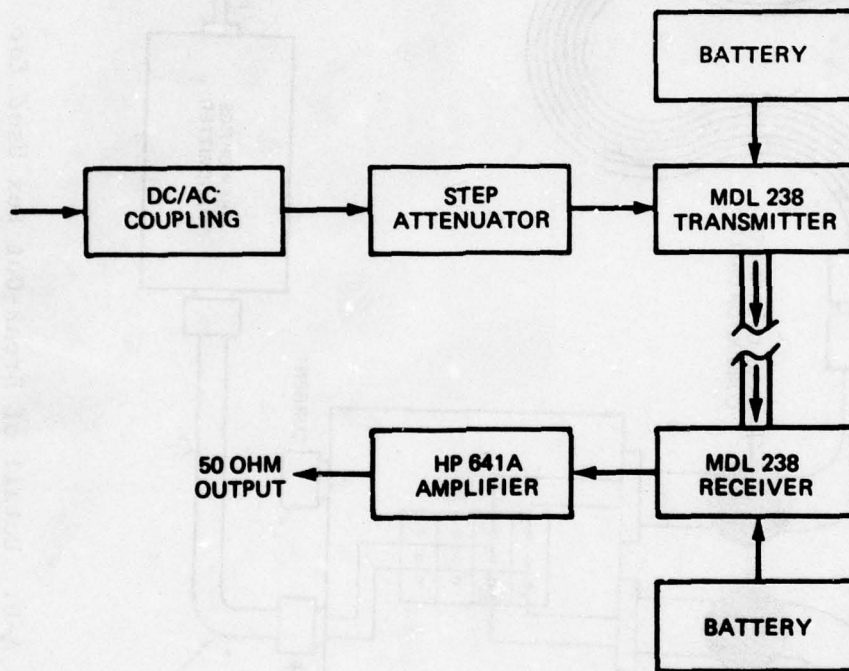
Figure A-7. Block Diagram of LST Measurement System
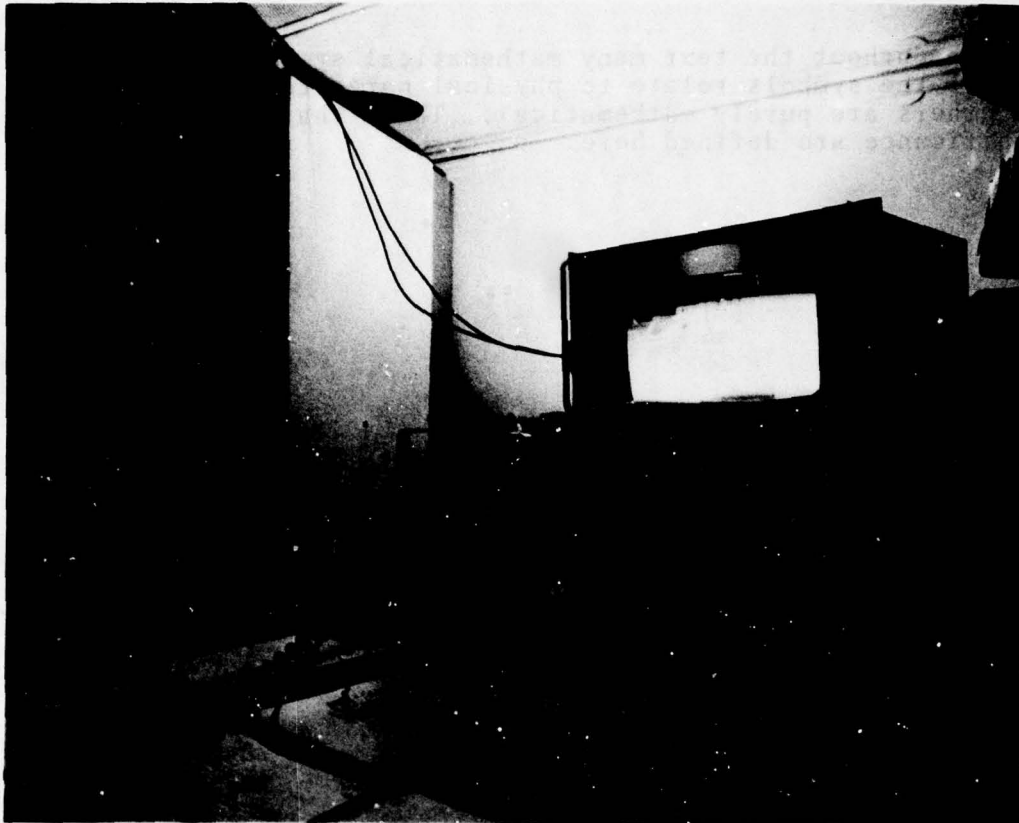
Figure A-8.   Monitoring and Recording Equipment
for LST Programs

LIST OF SYMBOLS

Throughout the text many mathematical symbols are used. Some of the symbols relate to physical parameters of interest and others are purely mathematical. Those that have a physical significance are defined here.

| Symbol	Description
α	Radius of circle
A	Area of continuous conductive collar
An	Attenuation due to the non-zero loss factor
$\alpha(f)$	Frequency varying skin resistance
a	Twin lead separation distance
C_s	Capacitance of source
c	Speed of light
C	Distributed capacitance (per meter) between aircraft skin and return lines
$\overline{C}$	Bulk capacitance ($C \times \ell_{A/C}$)
C_n	Capacitance of nth capacitive element in series resonant circuit
C_T	Capacitance of continuous conductive collar configuration
$\dfrac{di}{dt}$	Rate of change of current
dS	Increment of aperture area
d	Distance
ε_0	Permittivity constant coul²/nt-m² (of air)
e	Base of Naperian Logarithm
$\vec{E}$	Electric field vector
ε	Permittivity
E_n	Constant potential contour number n

161

Symbol	Description
E_o	Permittivity of free space
E_T	Tangential component of electric potential
$\vec{E}_e$	Electric field strength - e component
$\vec{E}_m$	Electric field strength - m component
E_R	Relative dielectric constant of plastic space
E	Electric field intensity
f_n	Resonant frequency of RLC series circuit
f_R	Resonant frequency
$G_{LST}(\omega)$	LST configuration transfer function
$G_{AP}(\omega)$	Aperture (small) transfer function
$G_{A/C}(\omega)$	Aircraft cable transfer function
$\vec{H}$	Magnetic field vector
H_{TAN}	Tangential component of magnetic field
H_N	Normal component of magnetic field
$\vec{H}_e$	Magnetic field strength - e component
$\vec{H}_m$	Magnetic field strength - m component
H_o	Aircraft surface current density
I_p	Peak current of return lightning stroke
$i_\ell(t)$	Skin current
$I_{LST}(\omega)$	Fourier transform of LST current pulse
$i(t)$	LTA current

Symbol	Description
$i(\ell,t)$	Time varying skin current at length from entry point
$i_s(x,t)$	Time varying current pulse
I_D	Displacement current
$\vec{J}$	Current density vector
$J_x(x)$	Skin current density function
J_x	Skin current density at point x from aperture
$\vec{J}_m$	Magnetic current density
$\vec{J}_e$	Electric current density
J_s	Aircraft surface charge density
K	Initial pulse magnitude
K^E	Far field ratio of E to aperture field E_o
k_1	Magnitude of peak skin current $i_1(t)$ in ground
k_2	Magnitude of peak skin current $i_2(t)$ in air
ℓ	Length
L	Inductance
L_1	Cable length between excitation point and shorted end
L_2	Cable length between excitation point and open end
L_o	Inductance of initial inductive element in series resonant circuit
$\ell_{A/C}$	Length of aircraft

163

Symbol	Description
L	Bulk inductance $(Lx\ell_{A/C})$
m	Number of round trip intervals in transmission line
η	Intrinsic impedance of free space $(\sim 377\Omega)$
N	Number of turns
σ	Conductivity of resistance paper
$\theta_A(\omega)$	Phase response of aperture
Q	Charge on continuous conductive collar
R_s	Value of damping resistance
$S_s(\omega)$	Fourier transform of skin current
$S_1(\omega)$	Fourier transform of induced voltage
$S_{LST}(\omega)$	Fourier transfer of output pulse
$S_I(\omega)$	Fourier transform of induced current
$S_s(\omega)$	Fourier transform of (aircraft) skin current
T_f	Rise time to peak current value of return lightning stroke
$T_f{}^1$	Time of maximum di/dt

164

Symbol	Description
T_1	Front time of current wave shape. Corresponds to the intercept of a line drawn through the 10% and 90% points of the rising phase and its intercept with the peak value of the pulse
T_2	Time for the current wave, hope to reach 50% of the peak value during the decay phase
T_o	Time constant for ℓ_{xc}
T	Effective exponential time constant
T.C.	Damped time constant
t_p	Round trip pulse propagation time in cable (RG-58)
μ_o	Permeability constant Weber/amp - m (of air)
U	Scalar magnetic potential
$v_I(t)$	Time varying induced aperture voltage
V_c	Capacitor charge voltage
$v(x,t)$	Time varying voltage pulse
$v_m(t)$	Time varying voltage input to transmission line
$v(\ell,t)$	Time varying skin voltage at length ℓ from entry point
$v(\ ,\ )$	Voltage which is a function of two variables
V	Voltage, volts
$V(X)$	Magnetic potential
$V_R(t)$	Reflected pulse amplitude

Symbol	Description
V_C	Excitation voltage at center of transmission line
V_T	Excitation voltage at open end of transmission line
V_F	Excitation voltage at shorted end of transmission line
V_p	Pulse velocity
V_A	LST aircraft voltage to ground at aperture
$\upsilon_2(t)$	Input continuous at $t = 0$
$\upsilon_1(t)$	Input discontinuous at $t = 0$
v_{in}	Voltage input to transmission line
ω	Frequency in radians per second
ω_1	$\pi C/\ell_{AK}$
ω_R	Resonant frequency in radians per second
Y	Input admittance of shorted transmission line
Y_o	Reciprocal of characteristic impedance
$Y_2(t)$	Convolution integral
Z_1	Impedance of cable length ℓ_1
Z_2	Impedance of cable length ℓ_2
Z_o	Characteristic impedance of cable
Z_{in}	Input impedance of shorted transmission line
$Z(s)$	Terminating impedance

Symbol	Description
α	Undamped resonant frequency
δ	Damping ratio
λ	Wave length
ρ_o	Reflection coefficient of sending end of transmission line
$\rho\ell_{A/C}$	Reflection coefficient of shorted end of transmission line
ρ_m	Magnetic charge density
ρ_e	Electric charge density